

Important Notice

This copy may be used only for the purposes of research and private study, and any use of the copy for a purpose other than research or private study may require the authorization of the copyright owner of the work in question. Responsibility regarding questions of copyright that may arise in the use of this copy is assumed by the recipient.

THE UNIVERSITY OF CALGARY

**FULL WAVEFORM PROCESSING AND INTERPRETATION
OF KILOHERTZ CROSSWELL SEISMIC DATA**

by

Ashraf A. Khalil

A THESIS
SUBMITTED TO THE FACULTY OF GRADUATE STUDIES
IN PARTIAL FULFILLMENT OF THE REQUIREMENTS FOR THE
DEGREE OF MASTER OF SCIENCE

DEPARTMENT OF GEOLOGY AND GEOPHYSICS

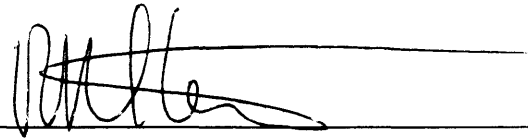
CALGARY, ALBERTA
FEBRUARY, 1991

© Ashraf A. Khalil 1991

THE UNIVERSITY OF CALGARY

FACULTY OF GRADUATE STUDIES

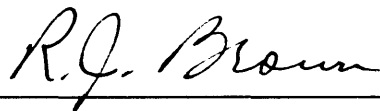
The undersigned certify that they have read, and recommend to the Faculty of Graduate Studies for acceptance, a thesis entitled "Full waveform processing and interpretation of kilohertz crosswell seismic data" submitted by Ashraf A. Khalil in partial fulfillment of the requirements for the degree of Master of Science.



Supervisor, Dr. R. R. Stewart,
Department of Geology and Geophysics



Dr. D. C. Lawton,
Department of Geology and Geophysics



Dr. R. J. Brown,
Department of Geology and Geophysics



Dr. D. R. Westbrook,
Department of Mathematics

February 27, 1991

Abstract

Previous studies of crosswell seismic data have mostly used tomographic inversion operating on direct traveltimes to obtain velocity information about the medium between the boreholes. A study is presented here for the analysis and processing of the full waveform of crosswell seismic data. This work uses direct arrivals to obtain velocity information and reflected arrivals to construct an image in depth.

Two data sets are considered through the development of the method; a synthetic data set and a field data set from the Midale field of southeastern Saskatchewan, Canada. The field data were acquired by Shell Development Company for Shell Canada Ltd. as part of their EOR monitoring studies. Raw field data showed a complex assortment of wave modes that included direct compressional and shear waves, head waves, converted transmitted waves, and reflected shear waves.

A traveltime inversion technique (layer-stripping via raytracing) is developed to obtain P- and S-wave interval velocities from their respective direct arrivals. Field data inversion results showed good agreement between the seismic and sonic velocities. Traveltimes generated from forward modeling using the estimated (1-D) velocity functions also showed favorable agreement when compared to the observed (picked) traveltimes. Error analysis gave a maximum relative error of 1.45 % in one particular interval in the P-wave function. The estimated P and S velocities were in general agreement with measurements of V_p/V_s reported in the literature.

Techniques of processing crosswell seismic data to construct a subsurface image using the reflected wavefields are developed here. Most of the processing steps are conventionally used in VSP data processing. This allows processing of crosswell data to be

carried out using existing software. The processing flow for crosswell data includes band-pass, median, and $f-k$ filtering steps. The subsurface coverage of the crosswell geometry is derived based on a constant-velocity model and found to cover zones past the midpoint between the boreholes. From a reconstruction technique, called here XHLCDP, reflected wavefields are used to construct a reflected image similar to that of the VSP transformation procedure. A final section is produced by summing all the individual reflection images. This section provides a detailed description both laterally, in the subsurface between the boreholes, and vertically, with depth resolution on the order of 1 m.

Synthetic seismograms are used to interpret the final sections. Their use has led to the identification of many subsurface horizons at and around the zone of interest. In this case study, the crosswell images have shown higher resolution of strata than those depicted by the synthetic seismograms. Finally, the coverage of the crosswell experiment promises to complement and extend the interpretation of well logs.

Acknowledgements

My sincere gratitude goes to the faculty and staff of the Department of Geology and Geophysics at The University of Calgary. In my application to the Faculty of Graduate Studies of the University of Calgary, I wrote in my letter of intent; " My study goal is to obtain a highly qualified Master of Science degree in Geophysics which would first, satisfy my intention of acquiring solid knowledge in the subject, and second, help me join the competitive oil industry". Now, after completing most of my degree requirements, I am very satisfied (and saturated!) with the geophysical understanding I have improved upon throughout my course and research work. I owe a great deal of thanks and appreciation to my thesis supervisor, Dr. Robert R. Stewart, who showed me the way to good science. His continuous support and valuable advice have always been of major encouragement.

I would like to thank Shell Canada Ltd. for releasing the log and crosswell data of the Midale field of southeastern Saskatchewan. Particular thanks go to Mr. David C. Henley of Shell Research in Calgary for providing valuable information about the Midale field and the crosswell survey through our periodical meetings. Most of the processing presented here in this thesis was conducted at Western Geophysical Company of Canada. Many thanks to Adam Chow and Lynn Burroughs of Western Geophysical for their generous assistance.

I have been fortunate to be a research member (as a graduate student) in the Consortium for Research in Elastic Wave Exploration Seismology (CREWES) of the Department of Geology and Geophysics at The University of Calgary. I wish to express my appreciation to all the sponsors of the CREWES project for their support. Particular thanks to Dr. R. James Brown and Dr. Donald C. Lawton for their valuable advice throughout my Master's program. I would also like to acknowledge my good friends Mark

Harrison, David Eaton, and David Schieck for the useful discussions while pursuing our graduate degrees.

Finally, I wish I could express how grateful I am to my parents and my wife Manal for their long-standing encouragement and support. To my kids Amira and Moustafa, your parents had a hard time making this possible, especially, when you were around !

Table of Contents

Abstract	iii
Acknowledgements	v
Table of Contents	vii
List of Figures	ix
Chapter 1 - Introduction	1
1.1 Overview.....	1
1.2 Thesis objectives.....	4
1.3 Data sets used in the thesis.....	5
1.4 Hardware and software used in the thesis	5
1.5 Structure of the thesis	6
Chapter 2 - Geologic setting, log, and crosswell data	7
2.1 Study area	7
2.2 Regional stratigraphy.....	8
2.3 Full-waveform sonic logs.....	9
2.4 Synthetic examples	9
2.5 Field data	16
Chapter 3 - Traveltime inversion	33
3.1 Introduction.....	33
3.2 Inversion geometry.....	34
3.3 Inversion formulation.....	37
3.4 Inversion results.....	42
3.4.1 Synthetic data examples	43
3.4.2 Field data inversion	47
3.5 Lithologic characterization.....	55
3.6 Conclusions.....	57
Chapter 4 - Reflection processing	61
4.1 Introduction.....	61
4.2 Single-channel processing.....	62
4.3 Median filtering	64
4.4 Deconvolution	70
4.5 <i>f-k</i> filtering	75

4.6	Gain.....	79
4.6.1	Time-variant gain.....	80
4.6.2	Time-invariant balance.....	80
4.7	Crosswell subsurface coverage.....	82
4.8	Crosswell transformation.....	92
4.9	Sum.....	101
4.10	Instantaneous amplitude.....	106
4.11	Conclusions	107
Chapter 5 - Data interpretation.....		111
5.1	Introduction.....	111
5.2	Synthetic data.....	111
5.3	Synthetic seismograms.....	112
5.4	Field data.....	114
5.5	Conclusions.....	117
Chapter 6 - Conclusions.....		118
Chapter 7 - Future work		122
References		123

List of Figures

Figure 1.1:	Geometry of the crosswell experiment. D represents the direct arrival, RU and RD represent reflected upgoing and downgoing respectively.....	2
Figure 1.2:	Crosswell geometry suggests the use of direct arrivals in estimating velocities, and reflected arrivals in obtaining a reflected image in depth. The right part of the Figure shows the compressional, 1, and shear, 2, slownesses of the zone of coverage.....	4
Figure 2.1:	Study area of the field crosswell data. The experiment was conducted between FS-1, source well, and I-2, receiver well. The distance between the boreholes is 13.5 m	7
Figure 2.2:	Regional stratigraphy of the Midale field (Shell lithology log)	8
Figure 2.3:	Full-waveform sonic log recorded in well FS-1.....	10
Figure 2.4:	Interval velocity functions of the sonic logs.....	11
Figure 2.5:	Depth model for generating synthetic data. Interface depths, P-wave layer velocities, and array geometry are displayed on the model	12
Figure 2.6:	Synthetic shot record. Shot 1 at depth 100 m with geophone locations 96 to 158 m with 2 m interval (same set of geophones for every shot). Direct arrivals are labeled D , while reflected upgoing events are identified by RUI where I denotes the interface at which reflection occurred. Reflected downgoing events follow the same scheme	14
Figure 2.7:	Synthetic shot record. Shot 2 at depth 124 m.....	14
Figure 2.8:	Synthetic shot record. Shot 3 at depth 180 m.....	15
Figure 2.9:	The relationship between direct-arrival incidence angles and vertical-component displacements.....	15
Figure 2.10:	Raw receiver gather (no. 2) of the Midale field data. Receiver is at depth 1392 m (star).....	17
Figure 2.11:	Trace-equalized receiver gather (no. 2) of the Midale field data. The arrow points at complex high-frequency noise.....	20
Figure 2.12:	Trace-equalized receiver gather (no. 5) of the Midale field data	21
Figure 2.13:	Trace-equalized receiver gather (no. 8) of the Midale field data	22
Figure 2.14:	Band-pass receiver gather (no. 2) of the Midale field data. Annotated are D-P and D-S for direct P- and S-wave	

	respectively, RUSS and RDSS for reflected upgoing and downgoing S waves	24
Figure 2.15:	Band-pass receiver gather (no. 5) of the Midale field data	25
Figure 2.16:	Band-pass receiver gather (no. 8) of the Midale field data	26
Figure 2.17:	Geometry showing raypaths of transmitted-converted arrivals	27
Figure 2.18:	Median-filtered record (no. 2); filter is designed on the P-wave direct arrivals.....	28
Figure 2.19:	Difference record (no. 2) between the band-pass filtered record (Figure 2.14) and the median-filtered record.....	29
Figure 2.20:	Comparison between computed and observed traveltimes of two T-SP events seen on Figure 2.19	30
Figure 2.21:	Source levels 1398.4 to 1406.4 m of receiver 5 to show head waves, H , and peg-leg multiple events, DM and RUM . Receiver is at depth 1399 m.....	32
Figure 3.1:	Blocked full-waveform velocity log of the Midale field data.....	35
Figure 3.2:	Layer-stripping via raytracing inversion geometry. x is the distance between boreholes. Receiver is in layer n while source is in layer i	36
Figure 3.3:	Geometrical representation of Newton's method for finding the real root of function $E(p)$	40
Figure 3.4:	Inversion of synthetic data with no errors introduced. The two curves, true and estimated velocity functions, match well.....	44
Figure 3.5:	Inversion of synthetic data with an isolated error in each interval. The two curves, true and estimated velocity functions, again match well.....	45
Figure 3.6:	Inversion of synthetic data with a uniform error in all the picks. There is a consistent error in the estimated velocity function (dots) with respect to the true solution (solid)	46
Figure 3.7:	Inversion of synthetic data with a random error in all the picks. The dotted curve is the estimated velocity function while the solid one is the true solution	47
Figure 3.8:	P-wave inversion of three independent receiver gathers.....	49
Figure 3.9:	S-wave inversion of three independent receiver gathers.....	50
Figure 3.10:	Comparison of P- and S-wave inversion results with the respective full-waveform velocity logs	52
Figure 3.11:	Comparison of the P-wave observed and computed direct	

	arrivals. The computed traveltimes are obtained by forward modeling using the estimated velocities from the inversion	53
Figure 3.12:	Comparison of the S-wave observed and computed direct arrivals. The computed traveltimes are obtained by forward modeling using the estimated velocities from the inversion	54
Figure 3.13:	The magnitude of the local error between the observed and computed P-wave traveltimes of Figure 3.11. Also plotted is the average residual error in every interval	55
Figure 3.14:	The magnitude of the local error between the observed and computed S-wave traveltimes of Figure 3.12. Also plotted is the average residual error in every interval	56
Figure 3.15:	The relation between inverted V_p and V_s for the assumed model intervals. A linear relationship can generally be observed.....	57
Figure 3.16:	The relation between inverted V_p/V_s and V_p for the assumed model intervals.....	59
Figure 3.17:	The relation between inverted V_p/V_s and V_s for the assumed model intervals.....	59
Figure 4.1:	Processing flow of crosswell seismic data used in the thesis	63
Figure 4.2:	Median-filtered upgoing wavefield of synthetic shot record 2	67
Figure 4.3:	Median-filtered downgoing wavefield of synthetic shot record 2 ..	67
Figure 4.4:	Median-filtered record of field-receiver gather 2. This figure represents the S-wave direct-arrival component of the record	68
Figure 4.5:	Difference record between the bandpass-filtered record (Figure 2.14) and the median-filtered record. This figure represents the reflection arrival component of the record.....	69
Figure 4.6:	The result of applying deterministic deconvolution. The direct arrivals of the filtered record (Figure 4.4) are assumed to be the seismic wavelet	73
Figure 4.7:	The result of applying statistical deconvolution. The total record (Figure 2.14) is deconvolved to remove the seismic wavelet	74
Figure 4.8:	Processing steps of the $f-k$ dip filter	76
Figure 4.9:	Upgoing reflected wavefield after $f-k$ dip filtering of the difference record (Figure 4.5)	77
Figure 4.10:	Downgoing reflected wavefield after $f-k$ dip filtering of the difference record (Figure 4.5)	78
Figure 4.11:	Gained upgoing reflected wavefield. No deconvolution is used....	83

Figure 4.12:	Gained downgoing reflected wavefield. No deconvolution is used.....	84
Figure 4.13:	Gained upgoing reflected wavefield. Deterministic deconvolution is used.....	85
Figure 4.14:	Gained downgoing reflected wavefield. Deterministic deconvolution is used.....	86
Figure 4.15:	Gained upgoing reflected wavefield. Statistical deconvolution is used.....	87
Figure 4.16:	Gained downgoing reflected wavefield. Statistical deconvolution is used.....	88
Figure 4.17:	A constant-velocity case to derive the 2-way normal-incidence time and subsurface reflection point.....	89
Figure 4.18:	Subsurface coverage of shot record 2 of the synthetic data.....	92
Figure 4.19:	Subsurface coverage of receiver gather 2 of the field data.....	93
Figure 4.20:	Upgoing map of XHLCDP transformation for shot 2 of the synthetic data.....	95
Figure 4.21:	Downgoing map of XHLCDP transformation for shot 2 of the synthetic data.....	96
Figure 4.22:	Upgoing map of XHLCDP transformation for receiver 2 of the field data.....	97
Figure 4.23:	Downgoing map of XHLCDP transformation for receiver 2 of the field data.....	97
Figure 4.24:	Total map of XHLCDP transformation for receiver 2 of the field data.....	98
Figure 4.25:	Subsurface coverage of receiver gather 2. Note the effect of limited recording time on the coverage.....	100
Figure 4.26:	Total map of XHLCDP transformation for receiver 2 of the field data after further poststack processing.....	102
Figure 4.27:	The sum of all maps of the synthetic data set.....	104
Figure 4.28:	The sum of all maps of the field data set.....	105
Figure 4.29:	Instantaneous amplitude of the single-receiver map (Figure 4.26).....	108
Figure 4.30:	Instantaneous amplitude of the sum of all maps (Figure 4.28)....	109

Figure 5.1:	Synthetic seismograms generated from the shear sonic log from the source well (FS-1). The band limits used to generate the wavelet are annotated on the top of each group of synthetic seismograms.....	113
Figure 5.2:	Correlation between the sum of all receiver-gather maps (right) and the synthetic seismogram in depth (middle) generated from the sonic log (left).....	115
Figure 5.3:	Correlation between the instantaneous amplitude of the sum (right) and the synthetic seismogram in depth (middle) generated from the sonic log (left)	116

Chapter 1 - Introduction

1.1 Overview

Crosswell experiments require at least two boreholes; receivers are placed in one borehole and source(s) in another. Upgoing and downgoing events are present in crosswell data as in a Vertical Seismic Profiling (VSP) survey, except that in the crosswell experiment the receiver can be above the source. When the receiver is at a similar depth as the source, waves traveling horizontally also exist (Figure 1.1). The unique advantage of the crosswell survey is that all of the source/receiver locations can be beneath the weathered layer and closer to the zone of interest. This setting avoids some loss of high frequencies. The energy range in crosswell seismic can be in the kilohertz range which can theoretically resolve layers as thin as 0.6 m (Iverson, 1988). This is very important for hydrocarbon-reservoir description and development where high resolution is required. The crosswell experiment shows considerable promise in monitoring enhanced oil recovery (EOR) activity in the area between the boreholes (Macrides, 1987; Bregman et al., 1989b; Justice et al., 1989).

Numerical modeling of crosswell data shows that reflected, transmitted, guided, and converted waves are all prominent (Hu et al., 1988b). However, most crosswell studies have used only the direct arrivals to obtain velocity information about the medium between the boreholes. Tomographic inversion techniques are a favorite analysis method. Bois et al. (1972) acquired and inverted, via raytracing, the first arrivals of crosswell data in order to detect major structural events. Imaging methods like the algebraic reconstruction techniques (ART) and the simultaneous iterative reconstruction techniques (SIRT) were used by Peterson et al. (1985) and Ivansson (1985) respectively to estimate seismic velocities for two-dimensional (2-D) models in the presence of low-velocity zones. Least-

squares inversion techniques, that produced 2-D models of compressional seismic velocities between two boreholes, have also been implemented to detect low-velocity

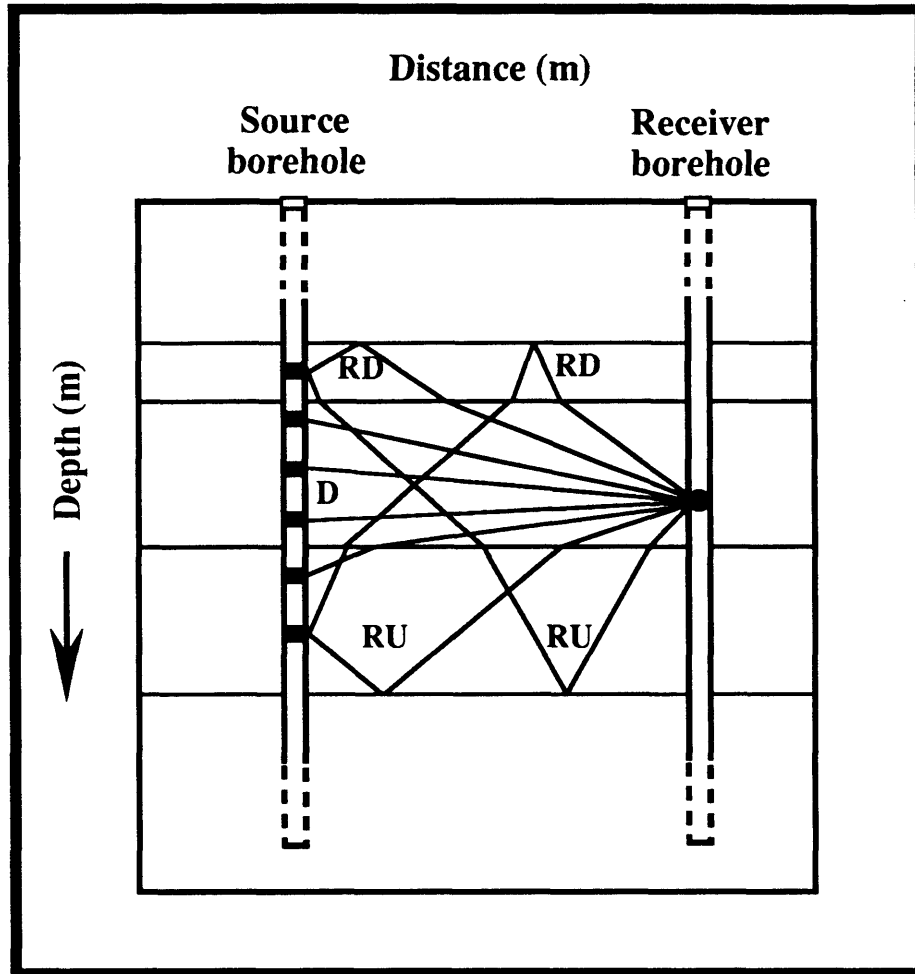


Figure 1.1: Geometry of the crosswell experiment. **D** represents the direct arrival, **RU** and **RD** represent reflected upgoing and downgoing respectively.

regions associated with steam injection, heavy fracturing, and fire-flood zones (Macrides et al., 1988; Bregman et al., 1989a; Justice et al., 1989). The same method helped Lines and LeFehr (1989) to understand better the homogeneity of the subweathering layer, but due to the lack of raypath coverage the inversion results could not help them to understand the weathered zone. Other applications of first arrivals in crosswell data include diffraction tomography (Pratt and Worthington, 1988) where a qualitative image of a wedge anomaly

was found, seismic velocity imaging before and after steam injection (Macrides et al., 1988), and a study of velocity anisotropy in shale (Winterstein and Paulsson, 1990). Chen et al. (1990) offered a comparison study for the resolution of surface seismic, reverse vertical seismic profile, and crosswell seismic data. They concluded that crosswell data provide higher resolution cross-sections and can potentially resolve smaller structures. Other recent studies that investigated EOR activities (Inderwiesen and Lo, 1990; Justice et al., 1990) and structural detection (Paulsson et al., 1990; Lo et al., 1990; Harris et al., 1990) have all shown the wide interest that the crosswell experiment has gained over the last few years.

A few studies have considered the different types of scattered waves which constitute the later arrivals in a crosswell seismic record. Of these studies, acoustic modeling and imaging of crosswell data with finite differences were presented by Hu et al. (1988a), for common-source gathers (prestack), and by Zhu and McMechan (1988), for stacked data. In those studies, the reverse-time wave-equation method was used to obtain a depth section from the total wavefield. Wave-equation imaging of scattered waves has produced high-resolution images of structures between boreholes (Pratt and Goult, 1989). Another 2-D migration/inversion technique by Beydoun et al. (1989) produced high resolution S-wave velocity and density depth images of the subsurface at some distance from the wells.

Only a few authors (e.g. Baker and Harris, 1984; Iverson, 1988) have considered reflection processing of crosswell data for a constant-velocity model by a method more similar to conventional CDP and VSP processing. The final results of these two studies were depth sections similar to the conventional CDP sections used for exploration purposes. Abdalla et al. (1990) further extended this method by considering the multi-layered case and deriving the subsurface reflection coverage of the crosswell geometry.

1.2 Thesis objectives

The overall objective of this thesis is to exploit the full waveform of crosswell data and deduce information about the geology in terms of velocity and reflectivity of the subsurface between boreholes. This starts with further understanding of wave propagation in the crosswell geometry. Secondly, a one-dimensional (1-D) solution of the velocity function is sought from the direct arrivals of the crosswell data (labeled **D** in Figure 1.2). The following objective is perhaps challenging in that it is unfamiliar to most of the

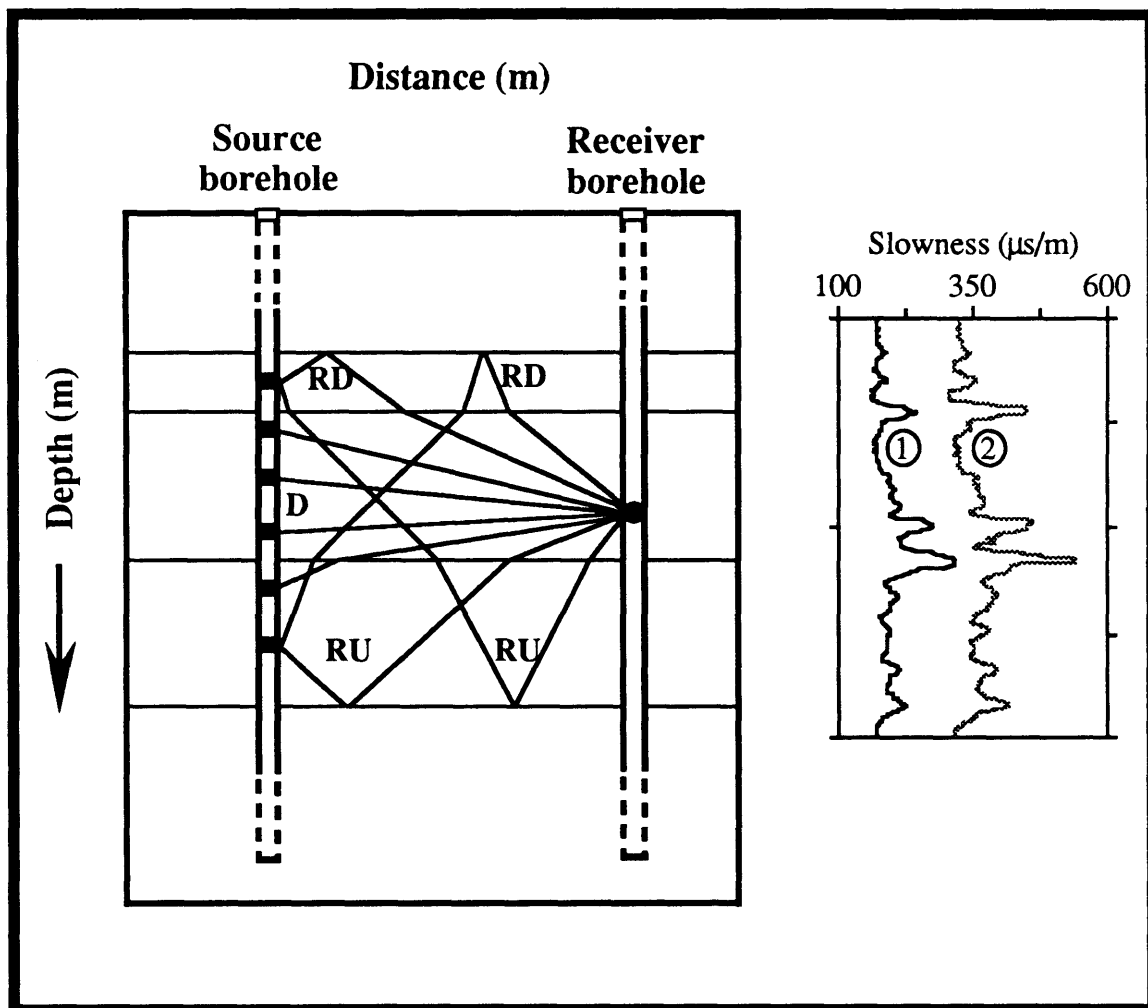


Figure 1.2: Crosswell geometry suggests the use of direct arrivals in estimating velocities, and reflected arrivals in obtaining a reflected image in depth. The right part of the Figure shows the compressional, 1, and shear, 2, slownesses of the zone of coverage.

research efforts paid to crosswell data. That is, focusing on developing a processing flow for the later arrivals, reflected events **RD** and **RU**, rather than the direct ones to obtain a reflected image in depth of the surveyed zone between the boreholes (Figure 1.2). Finally, as the ultimate goal of processing studies, the ability to interpret such reflected images is to be discussed.

1.3 Data sets used in the thesis

Two data sets are considered in this thesis. A synthetic data set and a field crosswell data set. Synthetic crosswell data are processed first. This is primarily because of their simplicity, and our interest in developing and validating the processing approaches and derivations. The synthetic records were generated using a ray-tracing software package (Uniseis®) on the Landmark workstation made available to the CREWES Project at The University of Calgary. The geologic model used here is based on the geology of the Midale field of southeastern Saskatchewan. A detailed description of the parameters used to generate the synthetic records is presented in the next chapter.

The real crosswell data set considered here is also from the Midale field of southeastern Saskatchewan. Shell Development Company acquired these data for Shell Canada Ltd. in 1985 as part of their EOR monitoring studies. Examples of the recorded field data set are shown and discussed in the next chapter.

1.4 Hardware and software used in the thesis

As mentioned in the previous section, the numerical modeling of synthetic crosswell data was performed using the Uniseis® software package on the Landmark workstation. Other numerical modeling was also conducted on the Sierra® software packages. The computer code described in Chapter 3, a traveltime inversion, was written in

FORTRAN and run on a Zenith AT-personal computer. Processing and other FORTRAN programming were done on the Western Geophysical of Canada systems. These include IBM-3081 mainframes, the CRYSTAL workstation, and VERSATEC plotting facilities connected to the mainframes. Other figures in the thesis were generated using Cricket Graph and MacDraw software packages on a Macintosh Plus computer. Finally, word processing was also completed on the Macintosh with Microsoft Word and, for mathematical equations, the Expressionist package was used.

1.5 Structure of the thesis

Chapter 2 provides the geologic background for the survey and shows data examples in the form of sonic logs and synthetic and field crosswell data. A traveltime inversion technique is presented in Chapter 3 to obtain P- and S-wave interval velocities from the respective direct arrivals in synthetic and field data. Processing flows for the later arrivals, reflected events, of both data sets are presented and discussed in Chapter 4. The final results of Chapter 4 are then inserted into an interpretation method in Chapter 5 to help identify the horizons and subsurface coverage. Chapter 6 concludes with the thesis findings and discusses the potential of reflection processing of crosswell data. Some future work suggestions are presented in Chapter 7.

Chapter 2 - Geologic setting, log, and crosswell data

2.1 Study area

The study area is located in the Midale field of southeastern Saskatchewan owned by Shell Canada Ltd. about 150 km southeast of Regina (Figure 2.1). The Midale field is a 37 year old oil field which has yielded about 100 million barrels of oil (The Calgary Herald, Nov. 30, 1990). The crosswell experiment considered in this thesis was conducted between a fluid sampling well (FS-1) and an injector well (I-2) as part of Shell's EOR monitoring activity. The source was placed in the FS-1 well while the receiver was in the I-2 well. The distance between the boreholes is 13.5 m (Figure 2.1) while the zone of interest extends from depths of 1380 m to 1420 m.

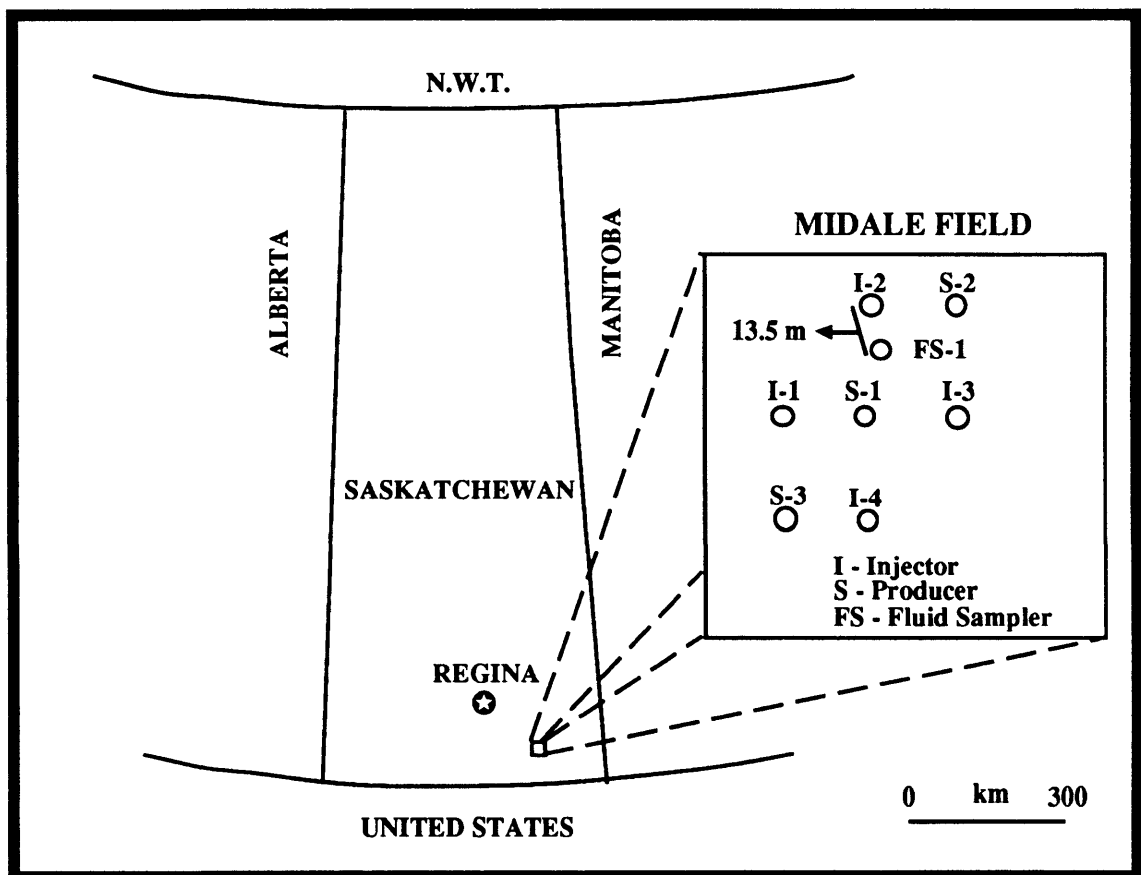


Figure 2.1: Study area of the field crosswell data. The experiment was conducted between FS-1, source well, and I-2, receiver well. The distance between the boreholes is 13.5 m.

2.2 Regional stratigraphy

The stratigraphic column of the area (Figure 2.2) is shown for the interval from 1365 m to 1430 m (Shell lithology log). There are two productive zones, a marly porous dolomite (upper) and a vuggy porous limestone (lower), in the Midale Formation. The Ratcliffe beds (shale- and dolomite-interbedded anhydrite) overlie the Midale strata. Below the productive layers, there is an anhydrite zone which overlies the Frobisher Alida Formation, another porous (but water-bearing) dolomite zone.

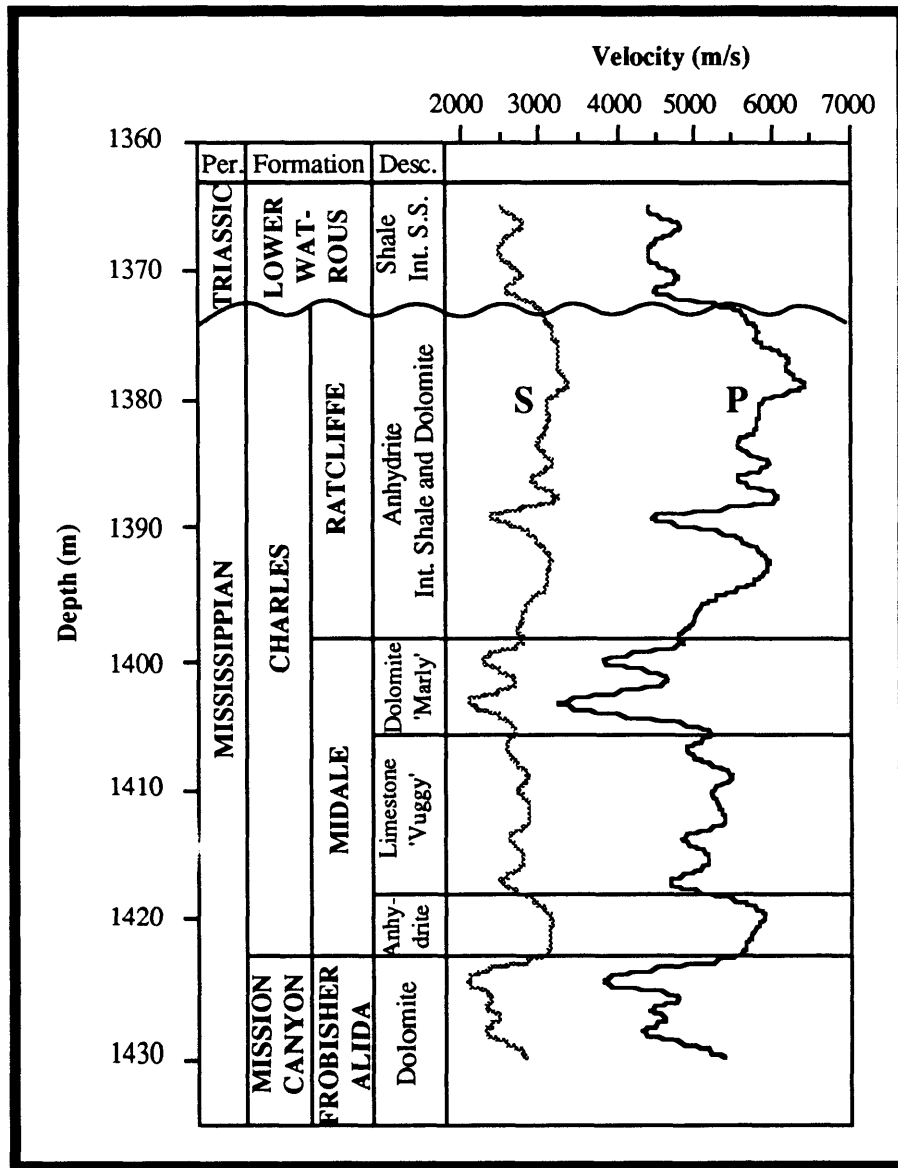


Figure 2.2: Regional stratigraphy of the Midale field (Shell lithology log).

2.3 Full-waveform sonic logs

There is a full-waveform sonic log recorded in well FS-1 in 1987 and used here in this thesis. Figure 2.3 shows a 13-point running average of the logs for the interval from 1300 m to 1500 m. The smoothing was performed on the logs only for display purposes. The two sonic logs show similar transit time details. The upper Midale formation (marly dolomite) lies between 1399 m and 1404 m while the lower Midale formation (vuggy limestone) is found between 1404 m and 1418 m. Figure 2.4 shows the velocity functions (the inverse of the slowness) of the sonic logs. In Chapter 5, sonic logs are used to create synthetic seismograms that are used in the interpretation procedure.

2.4 Synthetic examples

The depth model used to generate the synthetic source records is shown in Figure 2.5. The model was derived generically from a digitized sonic log from the Midale field. Identified on the model are the interfaces as I1, I2, I3, . . . , I9 and their corresponding depths. The P-wave velocity for each layer is also displayed on the same figure. Note that the distance along the top of the model and the depths of interfaces are relative. P-wave arrivals were measured as vertical displacements using the following parameters:

Distance between boreholes :	45 m
Number of sources:	3 (numbered 1 to 3)
Source depths:	100, 124, and 180 m
Number of receivers:	32
Receiver depths:	96 - 158 m
Receiver spacing:	2 m
Sampling interval:	100 μ s

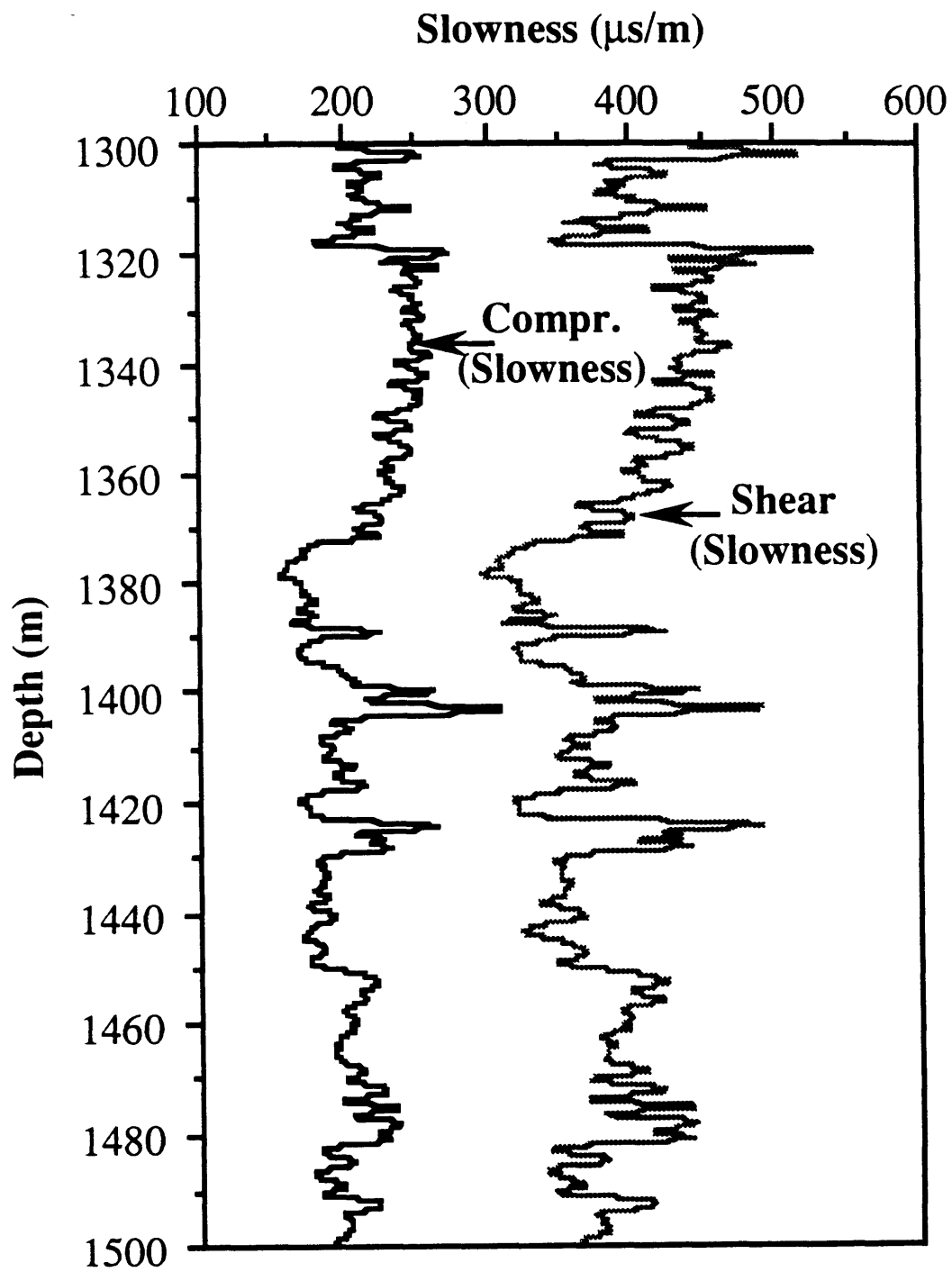


Figure 2.3: Full-waveform sonic log recorded in well FS-1.

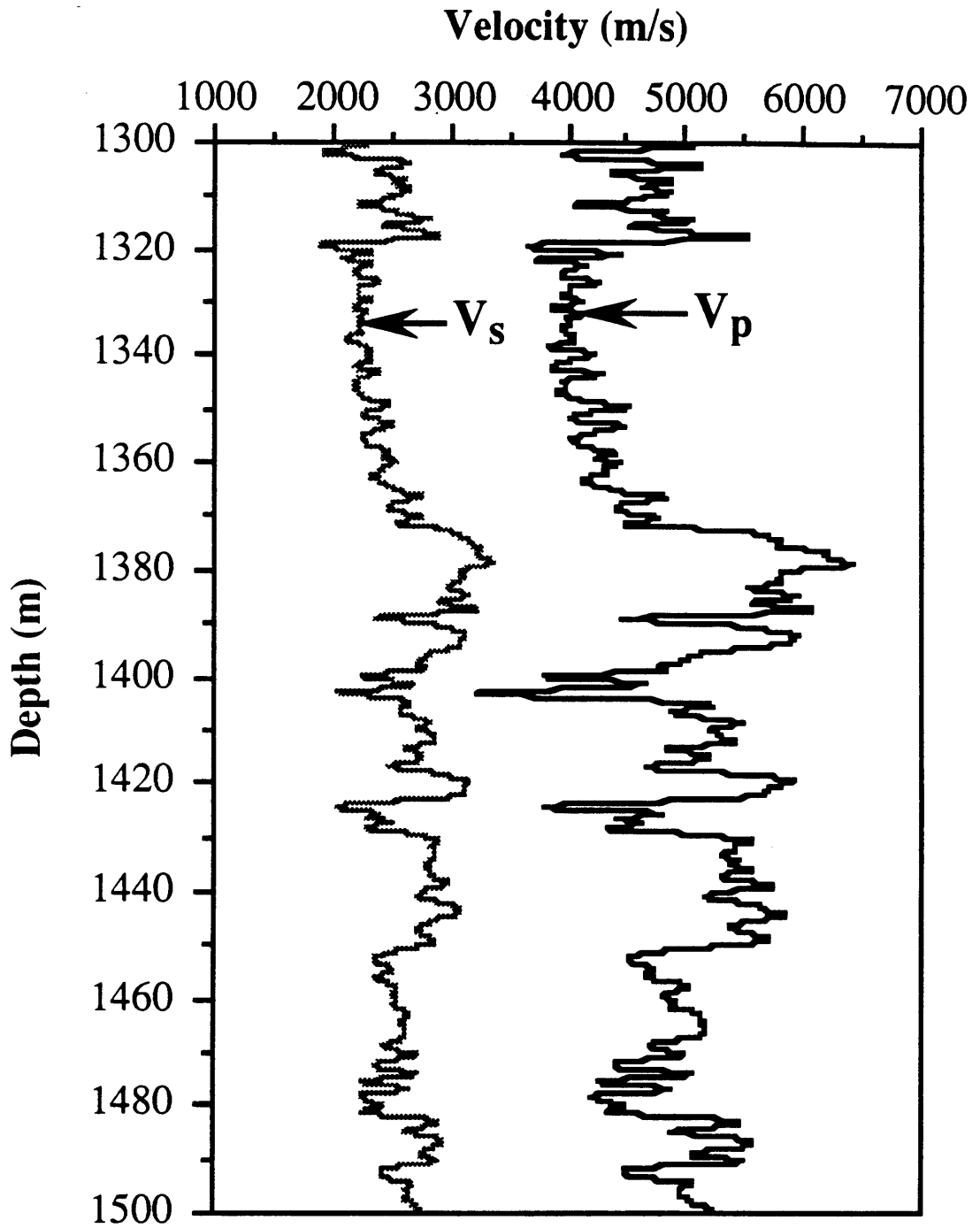


Figure 2.4: Interval velocity functions of the sonic logs.

Wavelet: Zero-phase Ricker
 1000 Hz centre frequency
 2 ms wavelet breadth

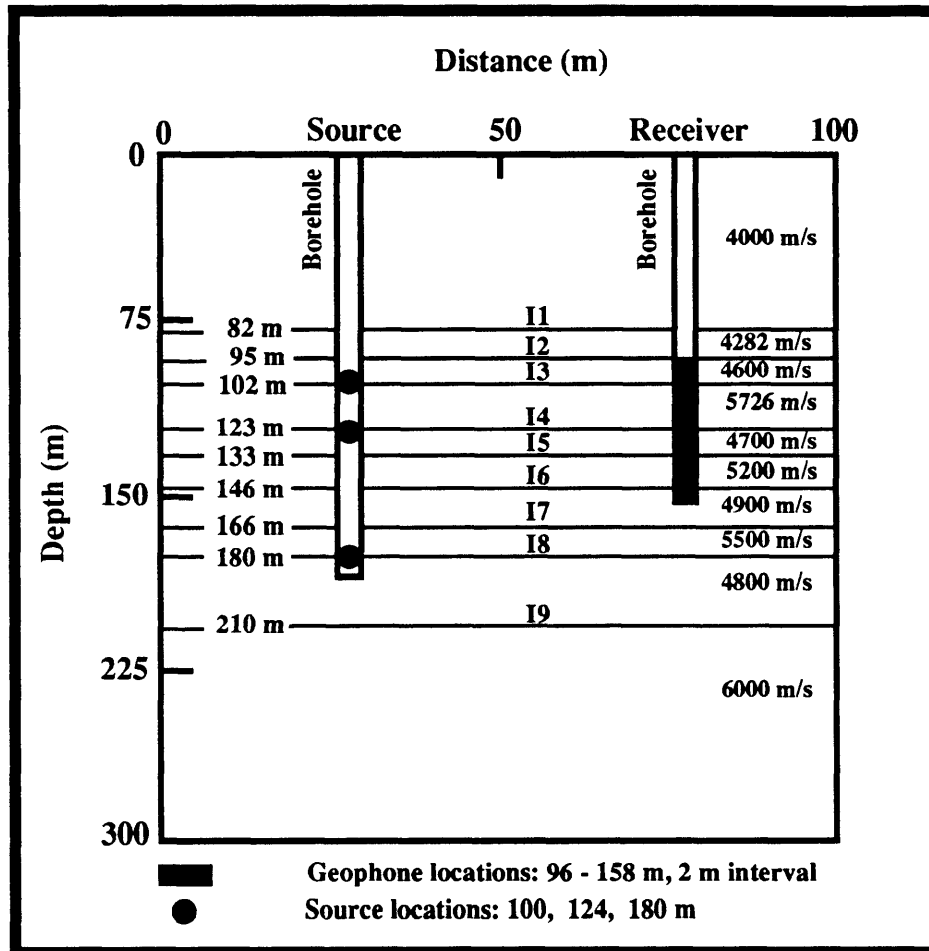


Figure 2.5: Depth model for generating synthetic data. Interface depths, P-wave layer velocities, and array geometry are displayed on the model.

Only direct (**D**) and primary reflected upgoing (**RU**) and downgoing (**RD**) events were generated in the ray-tracing (Figure 1.2).

The three simulated source gathers are displayed in Figure 2.6 through 2.8 which result from ray-trace numerical modeling (through the structure in Figure 2.5). Direct arrivals are labeled **D**, while upgoing reflections are labeled according to the interface from

which they reflected. For example, upgoing reflections from interface 1 (I1) are denoted RU1 and so on for all interface reflections. The same scheme was followed for the downgoing reflections. Investigating the slope (the change of recorded time with respect to the change of receiver depth) of the different arrivals on the synthetic records, particularly Figures 2.6 and 2.8, shows that the direct and reflected arrivals may have similar slopes in crosswell seismic data. For example, in Figure 2.6, the direct arrival (D) which is going downward has a slope similar to that of the downgoing reflected events (RD1 and RD2). Also in Figure 2.8, the direct arrival (D) which is going upward has a slope similar to that of the upgoing reflected event (RU9). What can be concluded from this observation is that these events of similar slopes may not be separable if we use slope-dependent algorithms such as median and *f-k* filtering.

The amplitudes recorded in these data are a function of angular incidence using Knott-Zoeppritz coefficients in both reflections and transmissions (Uniseis[®] User Manual). Because we are measuring the vertical displacement at the recording locations, the recorded amplitude of the direct arrival is proportional to the cosine of the incidence angle θ . Figure 2.9 shows a schematic configuration of this phenomenon for straight raypaths in the case of shot 1 (Figure 2.6). We see (Figure 2.9) that for a geophone at the same depth as the source, a very small direct-arrival amplitude is recorded since the angle of incidence, θ_2 in this case, is theoretically 90° . We see also that the absolute direct-arrival amplitude for the bottom location is much larger than that for the top one, since $\theta_3 < \theta_1$. Now, from θ_2 to θ_1 and from θ_2 to θ_3 , the absolute vertical displacement increases with decreasing incidence angle. For bending ray paths, the same behavior still holds with slightly different incidence angles. The same idea is applicable in shots 2 and 3, with the remark that shot 2 does not show the small direct displacement on the record at and around the shot depth because of the interference of the downgoing reflected event from interface I4 with these direct arrivals. Geometrical spreading is accounted for in these data. No gain

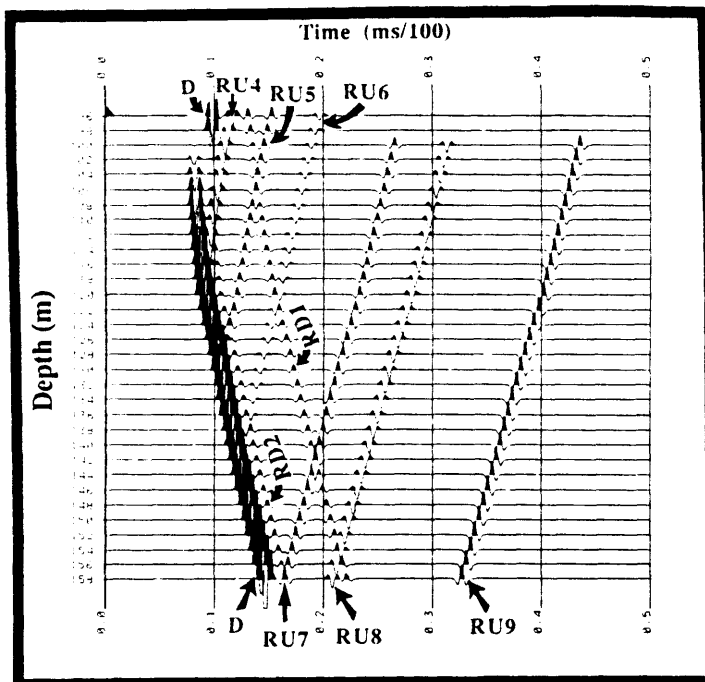


Figure 2.6: Synthetic shot record. Shot 1 at depth 100 m with geophone locations 96 to 158 m with 2 m interval (same set of geophones for every shot). Direct arrivals are labeled D, while reflected upgoing events are identified by RUI where I denotes the interface at which reflection occurred. Reflected downgoing events follow the same scheme.

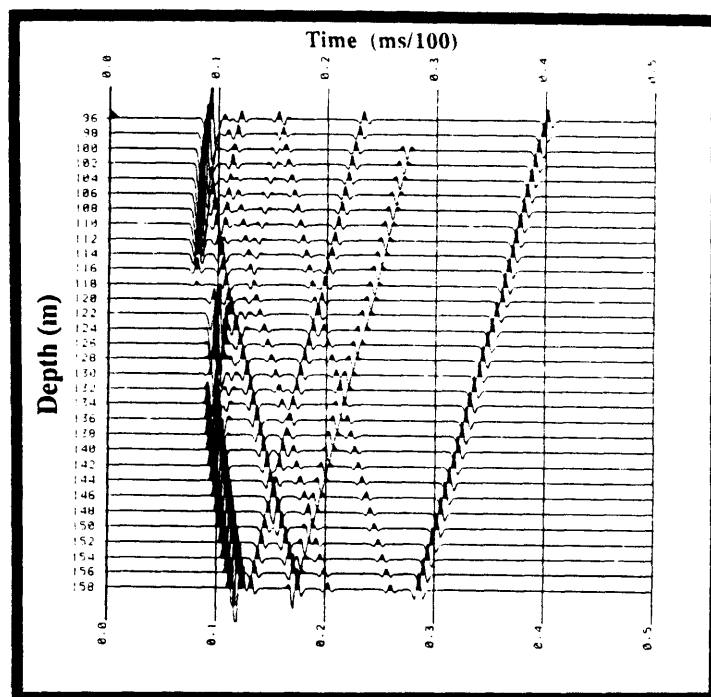


Figure 2.7: Synthetic shot record. Shot 2 at depth 124 m.

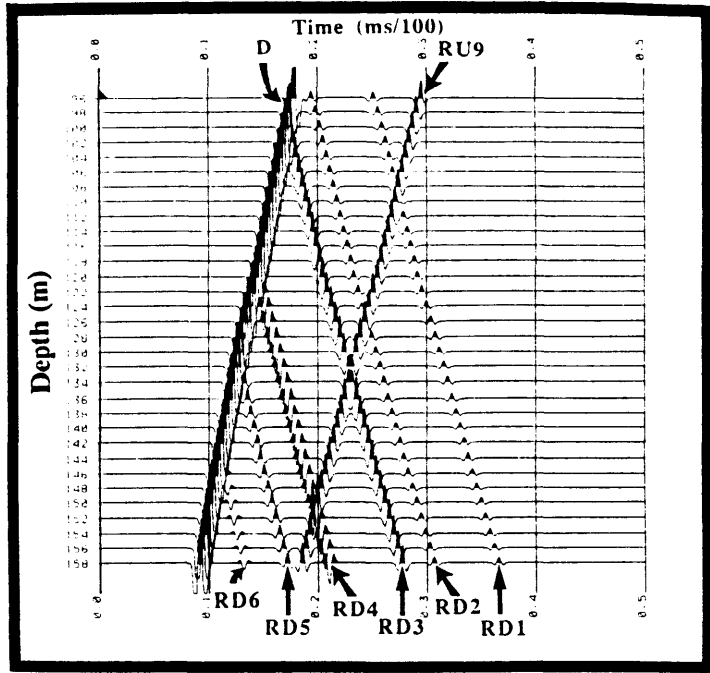


Figure 2.8: Synthetic shot record. Shot 3 at depth 180 m.

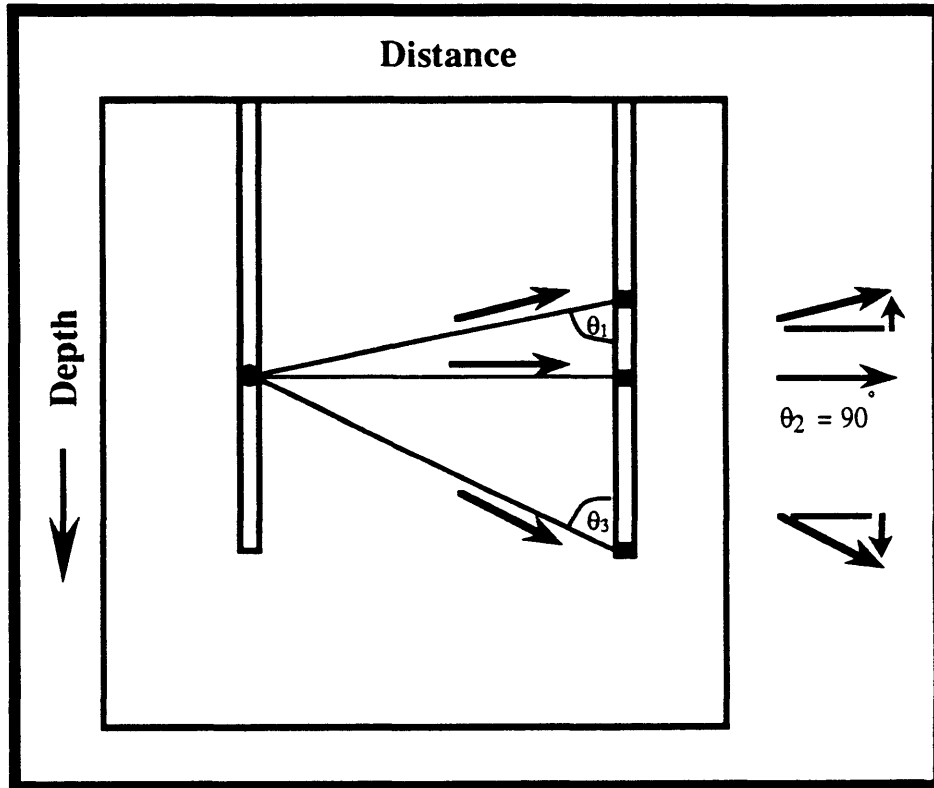


Figure 2.9: The relationship between direct-arrival incidence angles and vertical-component displacements.

of any type is applied to these data at any processing step. The values are simply multiplied by a scalar to obtain a reasonable plot.

2.5 Field data

The real data acquired in the Midale field is of the receiver-gather type with the following parameters:

Distance between boreholes:	13.5 m
Number of sources/receiver:	variable (average of 400)
Source depths:	1371.1 m (min.) to 1440.2 m (max.)
Source spacing:	0.1 m
Number of receivers:	9 (numbered 1 to 9)
Receiver depths:	1390.8, 1392.0, 1393.5, 1398.0, 1399.0, 1401.0, 1418.5, 1419.0, 1420.0
Sampling interval:	8 μ s

As seen above, there are 9 receiver gathers representing the field component of the data base provided in this thesis. The source used in the experiment was of a magnetostrictive type that had a centre frequency of 20 kHz while the receiver was a hydrophone. Both source and receiver were suspended in fluid-filled, cased boreholes. Unfortunately, there was one serious flaw in the data: the source/receiver depths could not be confirmed in the field and are only approximate (within an error of 2 m for the receiver depth).

An example of the raw recorded gathers (receiver no. 2) is shown in Figure 2.10. The receiver depth is 1392 m while sources are shown from depth 1376 m to 1405 m (291 traces). The maximum recorded time is 9.6 ms with sampling interval of 8 μ s (1200

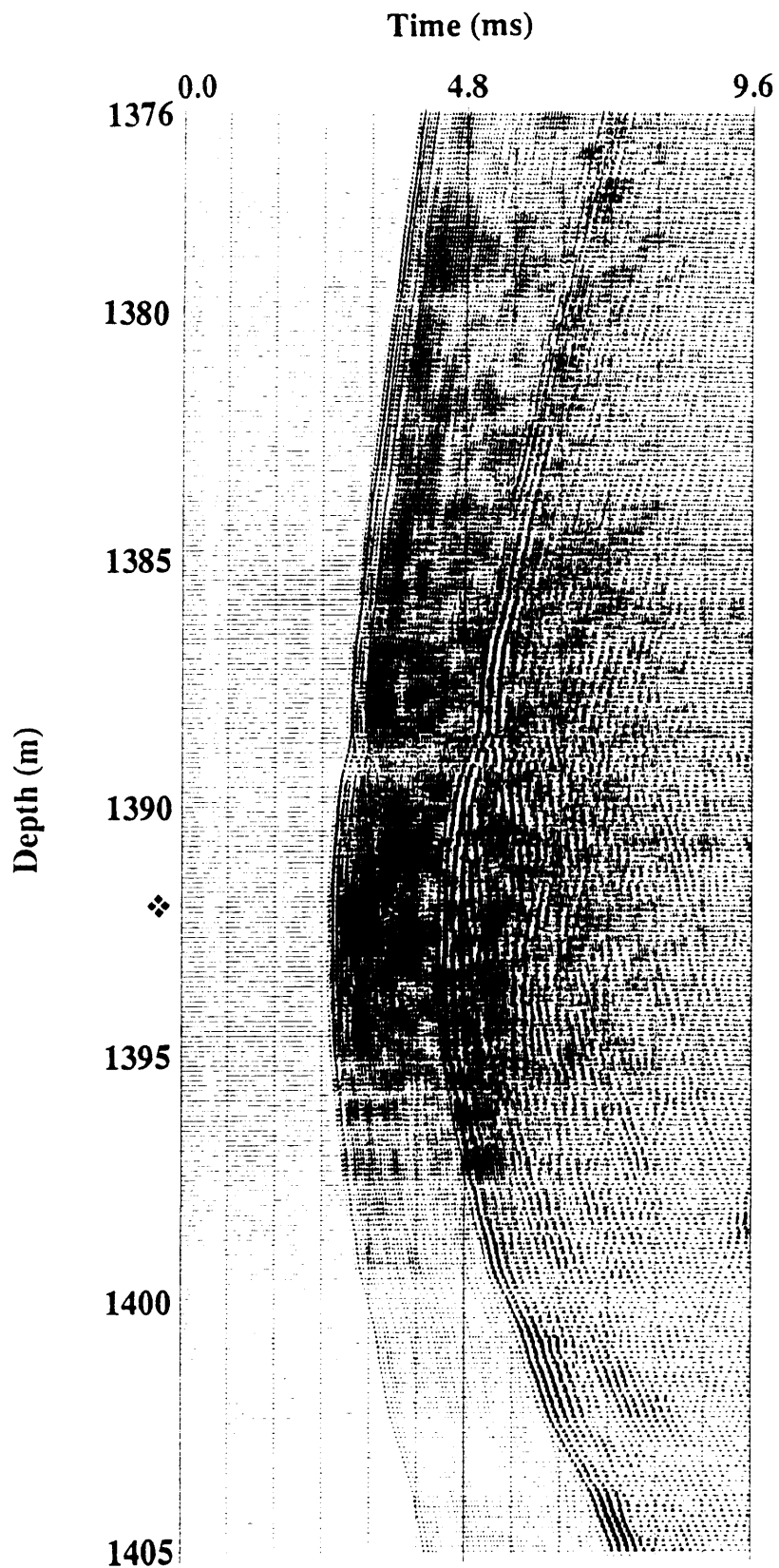


Figure 2.10: Raw receiver gather (no. 2) of the Midale field data. Receiver is at depth 1392 m (star).

samples). The experiment was originally conducted for transmission purposes; that is, focusing on the direct arrivals only. The data stored on tape are recorded to a maximum of 1200 samples. This represents an unfortunate disadvantage in these data for reflection processing as the reflections arrive at later times.

In Figure 2.10, we see that there is an amplitude variation between adjacent traces, especially in the lower part of the record. This may be due to the variations in source amplitude for shots at different levels. A trace equalization (trace balance) step is performed here to overcome this problem and equalize the traces. The procedure seeks a separate scale factor to be computed for each trace. The following steps are performed consecutively in the scale factor computation:

- A time window is determined within each trace. Here, the start time of the window is set at the first arrival sample of the trace while the end time of the window extends to the last sample of the trace (9.6 ms).
- Within the window, the mean absolute amplitude, \bar{A} , and the standard deviation of the absolute values, S , are determined. These are,

$$\bar{A} = \frac{\sum_{j=1}^N |a_j|}{N}, \quad 2.1$$

and

$$S = \sqrt{\frac{\sum_{j=1}^N (|a_j| - \bar{A})^2}{N}}, \quad 2.2$$

where a_j are the amplitudes from 1 to N in the window.

- The root mean square (rms) amplitude is then computed based only on samples within one standard deviation of the determined mean. That is,

$$\bar{A} - S < |x_i| < \bar{A} + S, \quad 2.3$$

and

$$A_{\text{rms}} = \sqrt{\frac{\sum_{i=1}^M x_i^2}{M}}, \quad 2.4$$

where x_i are the amplitudes from 1 to M that are within one standard deviation of the mean.

- Finally, the scale factor is the ratio of the desired output amplitude, here 2000, to the computed rms amplitude, A_{rms} .

Figure 2.11 shows the result of trace equalizing the receiver gather no. 2 (Figure 2.10). A more consistent trace amplitude is achieved, especially for the direct arrivals in the lower part traces.

Of the nine (9) receiver gathers provided in the data, receivers no. 2, 5, and 8 were chosen to represent what is called the three groups of the data (3 receiver gathers in each group). This can be seen in the depth locations of the receivers (section 2.5) where receivers no. 1, 2, and 3 (first group) are located in a zone that is considerably distant from that of receivers no. 4, 5, and 6 (second group). The same can be followed for receivers no. 7, 8, and 9 (third group). Figures 2.12 and 2.13 show the receiver gathers 5 and 8 respectively after trace equalization.

The three trace-equalized receiver gathers (Figures 2.11 to 2.13) show complex high-frequency features (arrow pointing in Figure 2.11) masking the coherent direct arrivals and their later events. Lovell and Hornby (1990) observed a second high-frequency

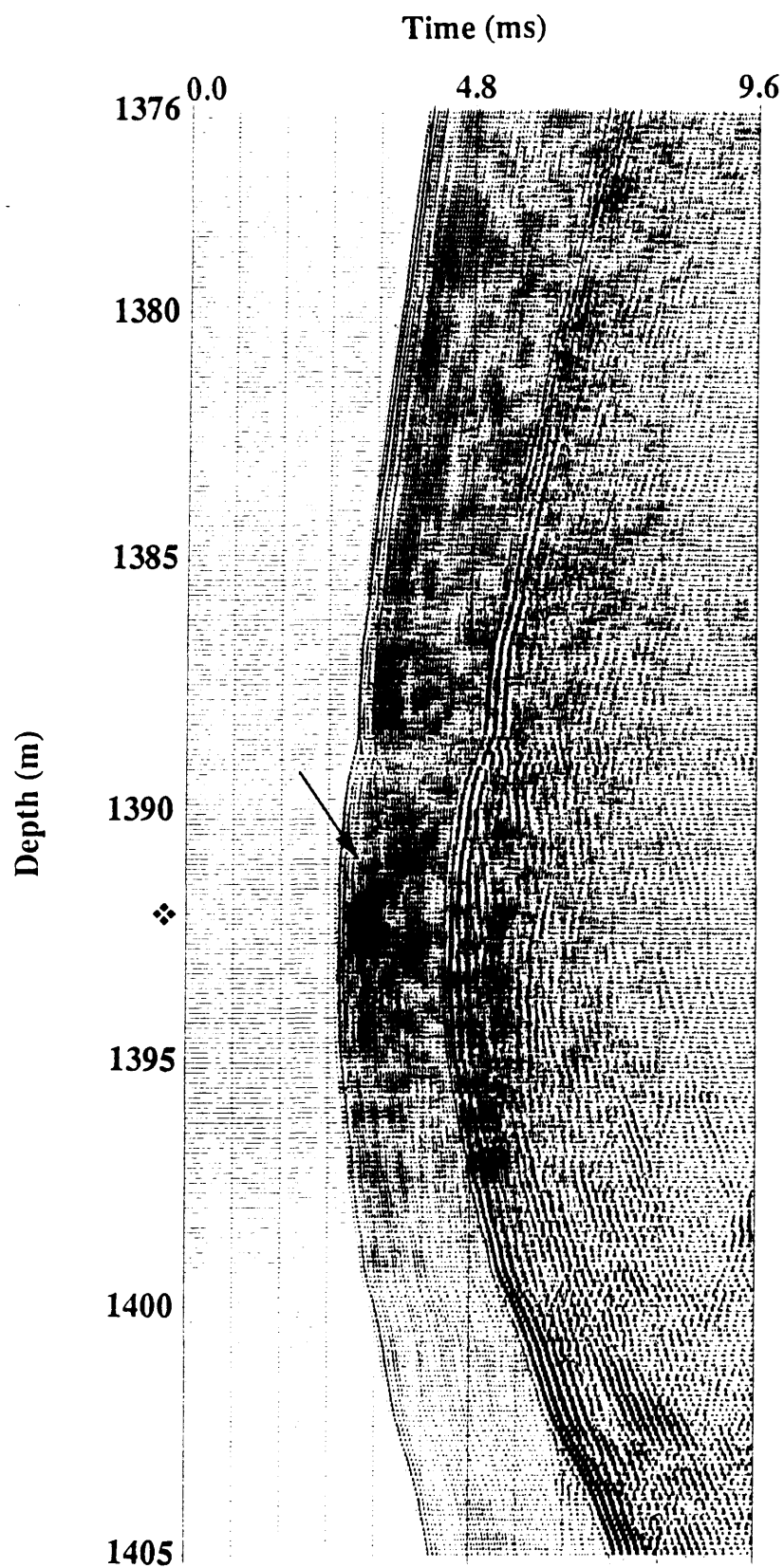


Figure 2.11: Trace-equalized receiver gather (no. 2) of the Midale field data. The arrow points at complex high-frequency noise.

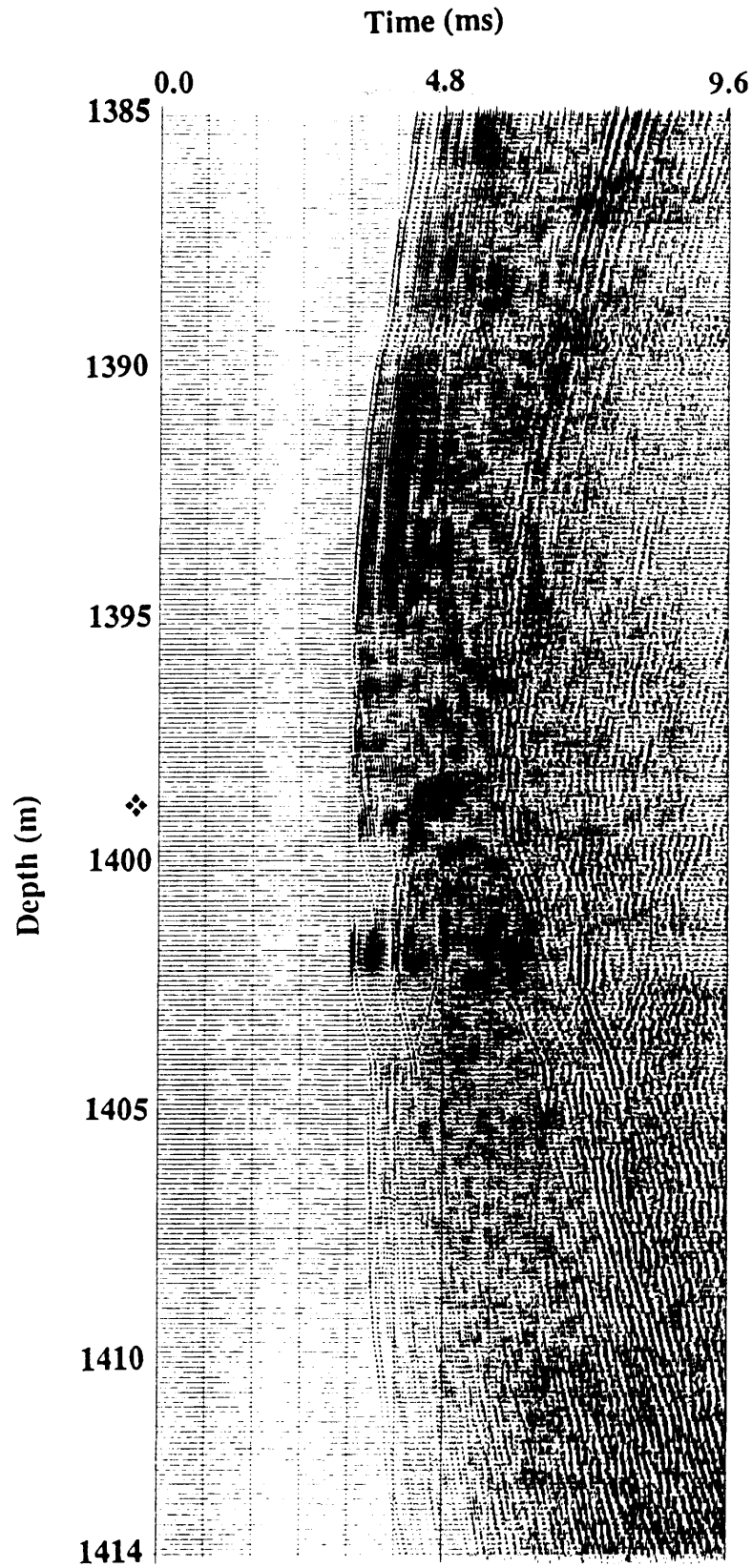


Figure 2.12: Trace-equalized receiver gather (no. 5) of the Midale field data.

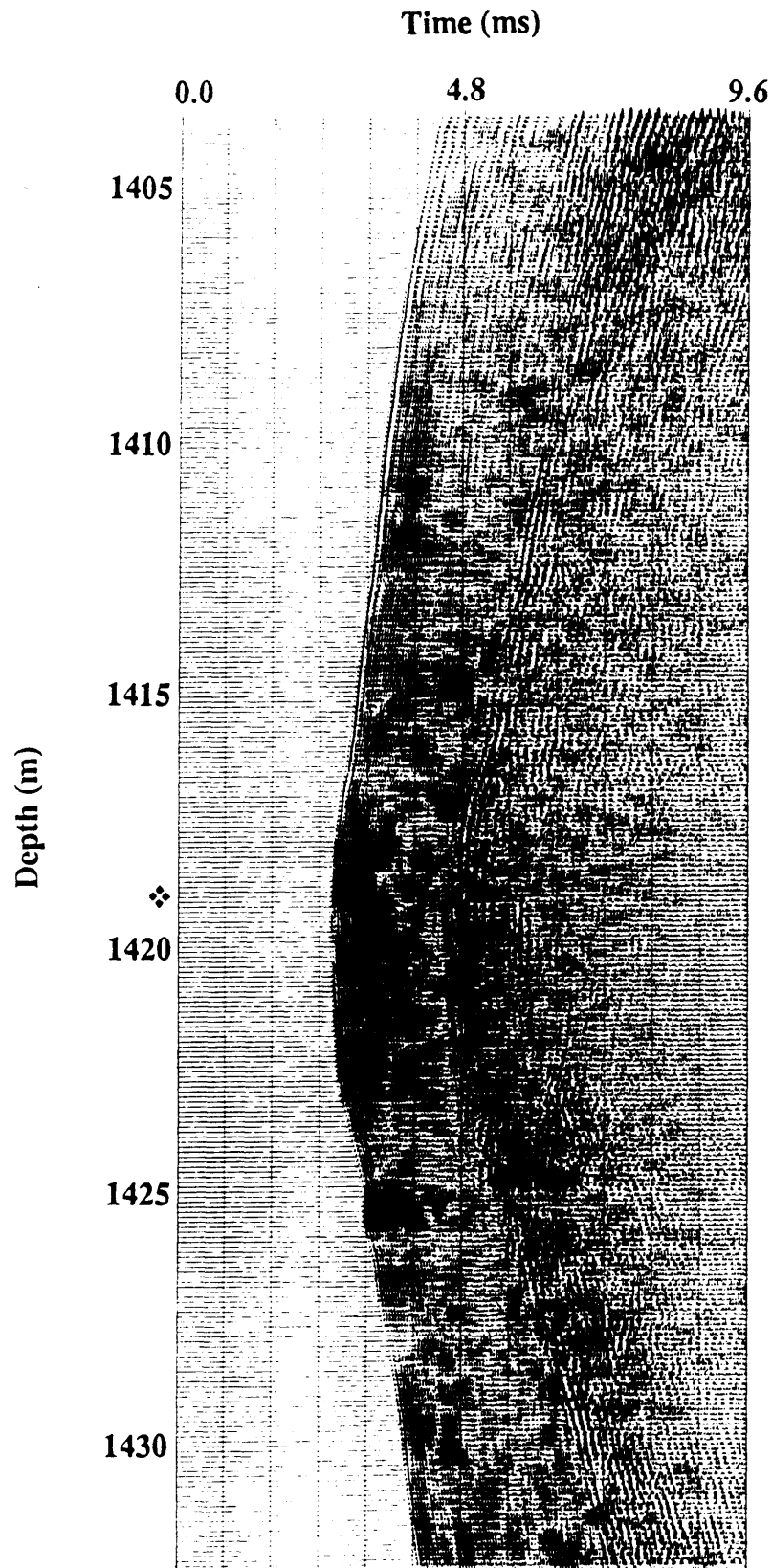


Figure 2.13: Trace-equalized receiver gather (no. 8) of the Midale field data.

(up to 20 kHz) resonance peak when they investigated borehole coupling through an elastic incident plane wave and the corresponding pressure along the borehole axis. To remove these high-frequency amplitudes and further investigate the wave types present in these crosswell data, a band-pass filter is applied in the time domain to the trace-equalized records. After testing many filter panels, the filter coordinates were chosen as 2.5, 3.125, 16.875, and 18.750 kHz with weights of .001, 1.0, 1.0, and .001 respectively. Figures 2.14 to 2.16 show the results of the band-pass filter on the trace-equalized records 2, 5, and 8 respectively. The quality of the data in receiver number 2 is significantly better than that of the other two gathers 5 and 8. However, events can generally be seen on all records with much more coherency. Although the magnetostrictive source and the hydrophone used in this experiment generate and record only P waves, P to S and S to P conversions at the borehole walls exist and enable the study of S waves as well as P waves. The same observation of conversion was noticed by Fehler and Pearson (1984). For example, direct P- and S-wave arrivals are labeled D-P and D-S as well as reflected upgoing and downgoing shear wave arrivals, RUSS and RDSS respectively. Note the strong amplitudes of the direct shear waves, particularly in Figure 2.14. Fehler and Pearson (1984) derived the expressions for the radiation patterns of P and S waves emitted by seismic sources or acoustic transducers in fluid-filled boreholes. The results of their derivations showed much larger S-wave amplitudes than those of P waves. Beydoun et al. (1989) observed similar radiation patterns, namely larger S waves in crosswell data recorded on both geophones and hydrophones. Other examples of strong shear waves include hydrophone-recorded VSP (Marzetta et al., 1988) and full-waveform sonic data (Hornby, 1989).

Another transmitted-wave type, T-SP, which is rather difficult to recognize on the band-pass record no. 2 (Figure 2.14), was identified by implementing a median filtering process (discussed in section 4.3). Figure 2.17 demonstrates the geometry of these

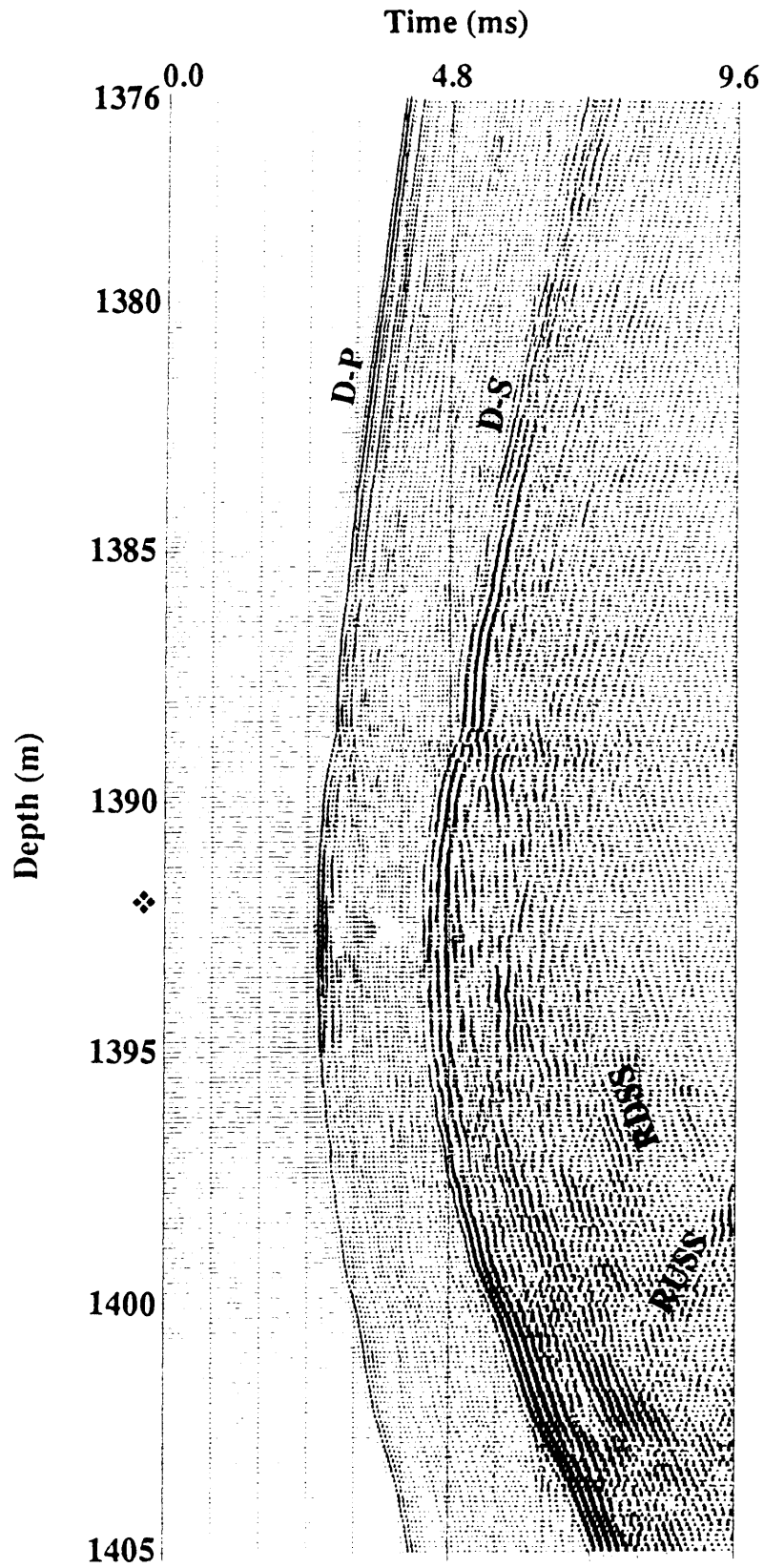


Figure 2.14: Band-pass receiver gather (no. 2) of the Midale field data. Annotated are D-P and D-S for direct P- and S-wave respectively, RUSS and RDSS for reflected upgoing and downgoing S waves.

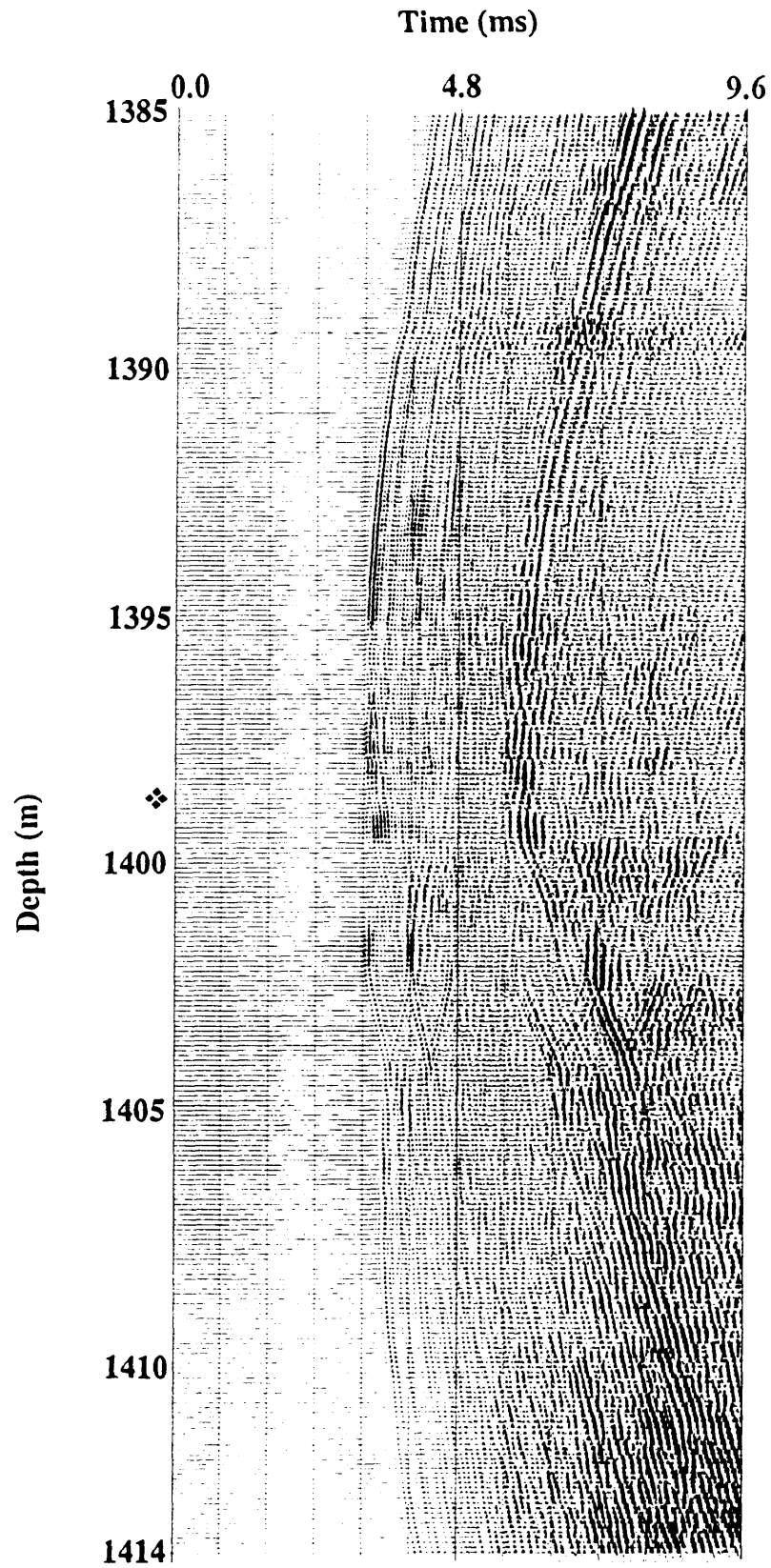


Figure 2.15: Band-pass receiver gather (no. 5) of the Midale field data.

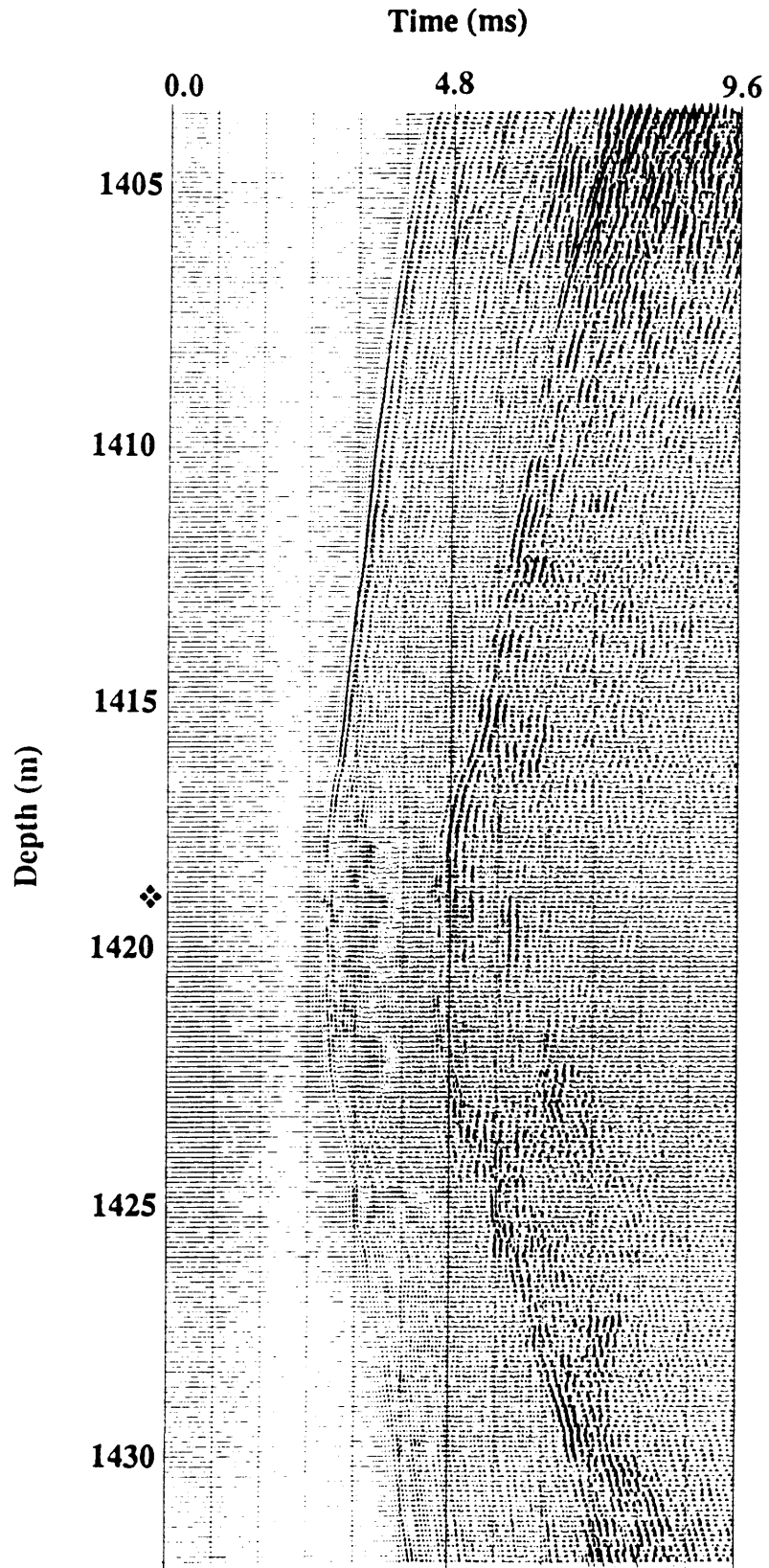


Figure 2.16: Band-pass receiver gather (no. 8) of the Midale field data.

transmitted arrivals. The median filter, designed on the P-wave direct arrivals, removed the wave trains that follow the same slope as the P-wave direct arrivals (Figure 2.18). The difference record (Figure 2.19) obtained by subtracting the filtered record (Figure 2.18) from the total input one (Figure 2.14) shows a transmitted type of wave that starts as an S wave from the source borehole wall and converts into a P wave at an interface before it gets recorded on the receiver. Two main T-SP events have been interpreted on the difference record. They truncate on the direct P-wave arrivals at depths of about 1387 m and 1390 m. There are two observations indicating that these arrivals follow that specific path.

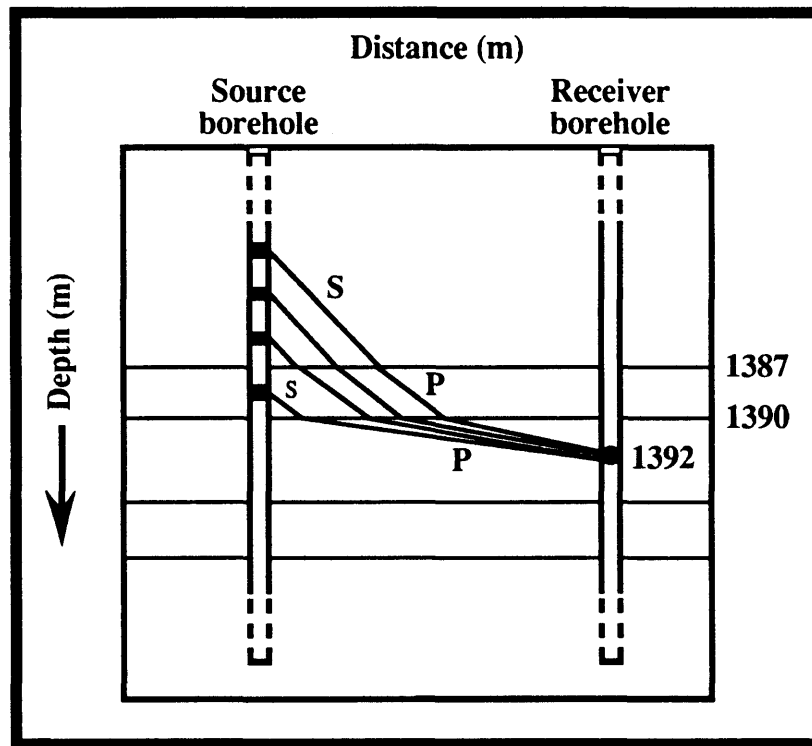


Figure 2.17: Geometry showing raypaths of transmitted-converted arrivals.

The first is that at the truncation points the transmitted events have almost the same arrival time as that of the direct P-waves. This means that closer to the interface where they converted, the shear segment of the raypath is minimal. The second observation is that their slopes get closer to that of the direct S-waves as the source location is further away (up)

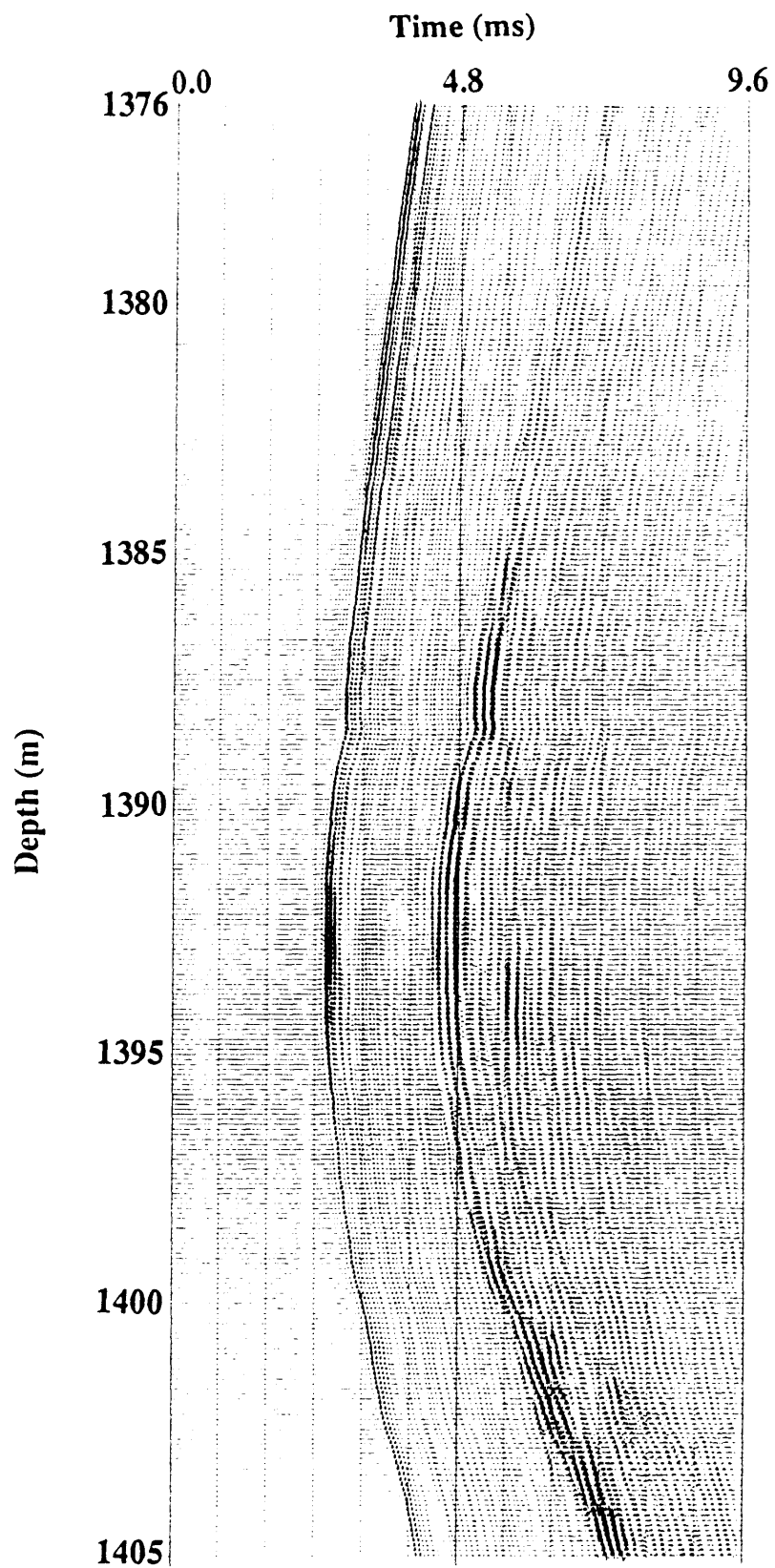


Figure 2.18: Median-filtered record (no. 2); filter is designed on the P-wave direct arrivals.

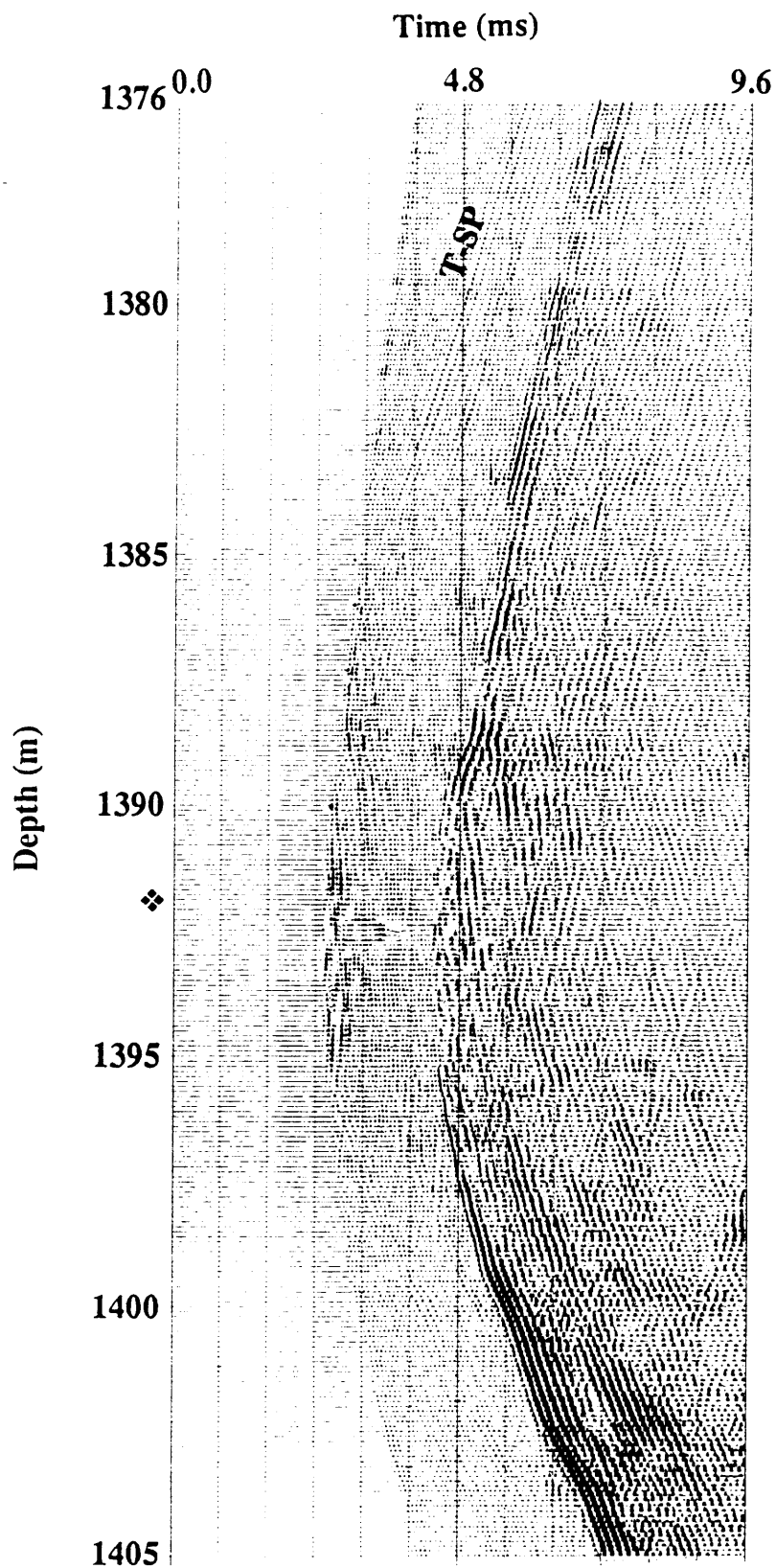


Figure 2.19: Difference record (no. 2) between the band-pass filtered record (Figure 2.14) and the median-filtered record.

from that of the receiver. The interpretation of these arrivals as tube waves is contradicted by the formation apparent velocity they possess. Also, there is no change of borehole radius that could lead to the generation of tube waves.

Numerical modeling using the Sierra® software package was carried out to check the previous converted-transmission interpretation. Figure 2.20 shows a comparison between the observed and computed traveltimes of the two T-SP events interpreted on

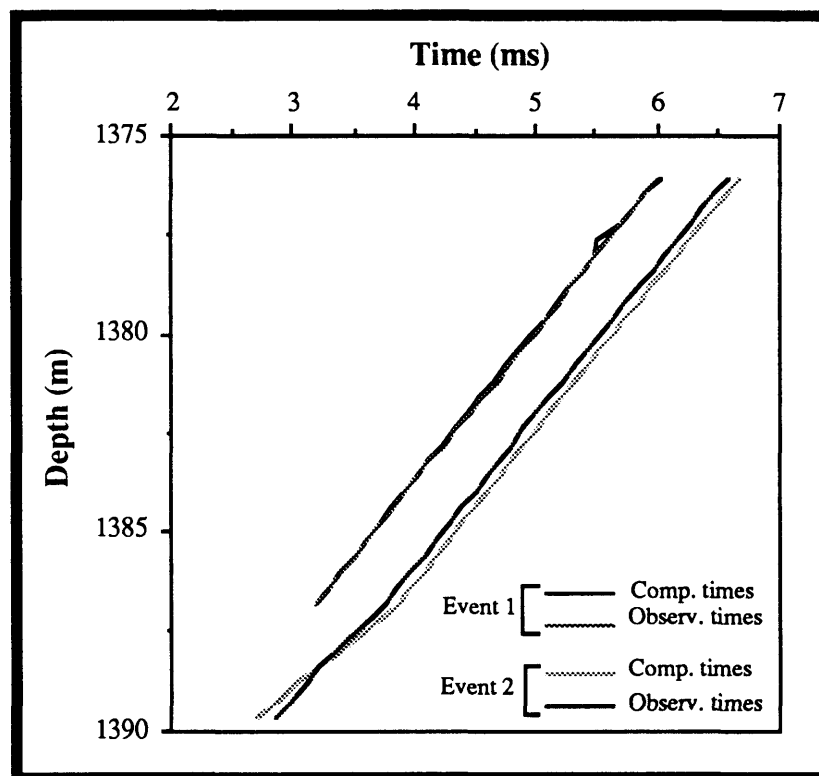


Figure 2.20: Comparison between computed and observed traveltimes of two T-SP events seen on Figure 2.19.

Figure 2.19. As shown in Figure 2.20, the two curves of event 1 agree quite well. The traveltimes of Event 2 exhibit a constant difference over most of the event. This is probably due to a consistent shift in the picking or a slight displacement of the conversion interface

while carrying out the modeling. In general, numerical modeling showed that the slopes and traveltimes of the observed and computed curves are similar which supports the interpretation of the raypaths of these transmitted arrivals.

The occurrence of these converted transmissions could assist in constructing the layering of a 1-D model needed for the inversion technique discussed in Chapter 3. It should also be noted from Figure 2.19, that consistent primary P-wave reflections are not apparent in these data. The reflected data are dominated by S waves in the form of S-S and possibly S-P raypaths. It is apparent that the acquisition geometry with its large angles of incidence favors shear-wave conversions (Beydoun et al., 1989). The use of P waves in this thesis will be limited to the inversion of direct P traveltimes arrivals.

A final event of interest can be seen in Figure 2.15 between depths 1399 m and 1406 m. Figure 2.21 is an enlarged version of that interval. The location of the receiver in this gather is 1399 m. Head waves, annotated as **H**, are present as a result of a low-velocity zone in the upper Midale formation. Also present are direct arrivals, annotated as **D**, around those head wave arrivals. A reflected upgoing event, annotated as **RU**, appears for a limited number of levels (about 1400 m to 1404 m). A significant feature related to the latter two events, **D** and **RU**, is a peg-leg multiple, annotated as **DM** and **RUM**, which is believed to have been evolved in the high-velocity zone of the upper Midale formation. One final note is that similar wave types to the ones discussed above can be observed later in the shear-wave arrivals in the record (about 5.6 ms).

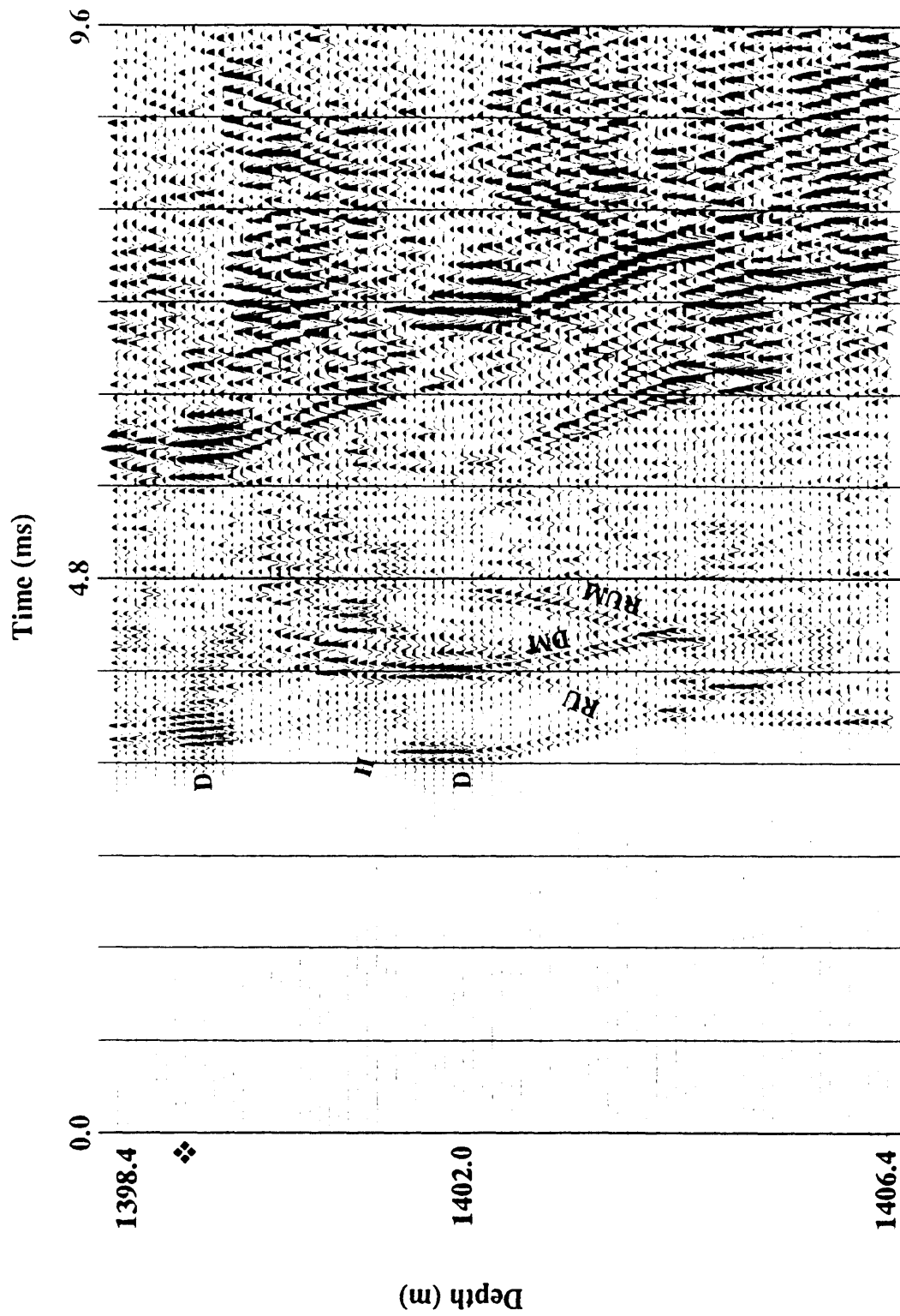


Figure 2.21: Source levels 1398.4 m to 1406.4 m of receiver 5 to show head waves, **H**, and peg-leg multiple events, **DM** and **RUM**. Receiver is at depth 1399 m.

Chapter 3 - Traveltime inversion

3.1 Introduction

The majority of crosswell studies have concentrated on tomographic inversion methods (section 1.1) that use the direct arrivals to construct 2-D models in terms of seismic velocities, mostly for compressional waves (Bois et al., 1972; Peterson et al., 1985; Ivansson, 1985; Macrides et al., 1988; Bregman et al., 1989a; Justice et al., 1989; Lines and LeFehr, 1989). The pictures produced (tomograms) can indicate subsurface structure and monitor EOR experiments by detecting velocity anomalies in two dimensions. The purpose of this study is to use the observed P- and S-wave direct arrivals in these crosswell data and seek respective (P and S) 1-D velocity information. Obtaining such information is of 2-fold interest. First, we would like to use the estimated interval velocities in further crosswell data processing that is motivated by the conventional processing of VSP data. Second, using both P and S velocity information, we can consider the rock property V_p/V_s and see its relation to the lithology information already available.

Further processing of the VSP requires velocity analysis to reconstruct the VSPCDP map (Wyatt and Wyatt, 1984; Dillon and Thomson, 1984). In the VSP geometry, Stewart (1984) developed a ray-trace based least-squares inverse method to arrive at a better estimate and statistical description of the P- and S-wave velocity functions. This model-based method minimizes the error between the observed and computed traveltimes through forward modeling iterations. Other authors have included primary reflection traveltimes in the inversion method to estimate subsurface two-dimensional dips (Lines et al., 1984) and interval P-wave velocity functions (Salo and Schuster, 1989). The work by Lines et al. (1984) involved a "layer-stripping" scheme in which the dips of the shallow layers are estimated before the deeper dips are estimated. The layer-stripping scheme was also used to invert traveltimes directly via raytracing and obtain interval

velocity and thickness of each layer in surface seismic surveys (Justice, 1986a) and interval velocities in VSP surveys (Justice, 1986b). Other traveltimes inversion techniques have considered the acoustic wave equation (Luo and Schuster, 1990a, b) to construct 1-D velocity profiles.

A reasonable estimate of the interval velocities can be extracted by blocking and interpreting the full waveform sonic log (Figure 3.1). However, an inversion technique is developed to accurately obtain such interval velocity information for crosswell P and S waves. The method, similar to that of Justice (1986b), is based on layer-stripping via raytracing. The geometrical and theoretical aspects of the method are discussed here in detail followed by synthetic and field data inversion results.

3.2 Inversion geometry

Available subsurface information (D. Henley, personal communications) about the Midale field in southeastern Saskatchewan and a limited separation between boreholes (13.5 m) indicate that a flat-layered model is appropriate for the inversion procedure. Also, as mentioned earlier, a 1-D solution of the velocity function is sought. The parameters given to the inversion program are the geologic model that specifies the layering between the boreholes, the experiment geometry (source and receiver locations), and the direct arrival picks of both P and S waves. If we let x be the distance between the boreholes and t^n be the observed traveltimes at the receiver in layer n from a shot in layer i (Figure 3.2), then it has been shown (Slotnick, 1959) that

$$x = \sum_{k=i}^n \frac{p v_k \Delta z_k}{[1 - p^2 v_k^2]^{\frac{1}{2}}}, \quad 3.1$$

and

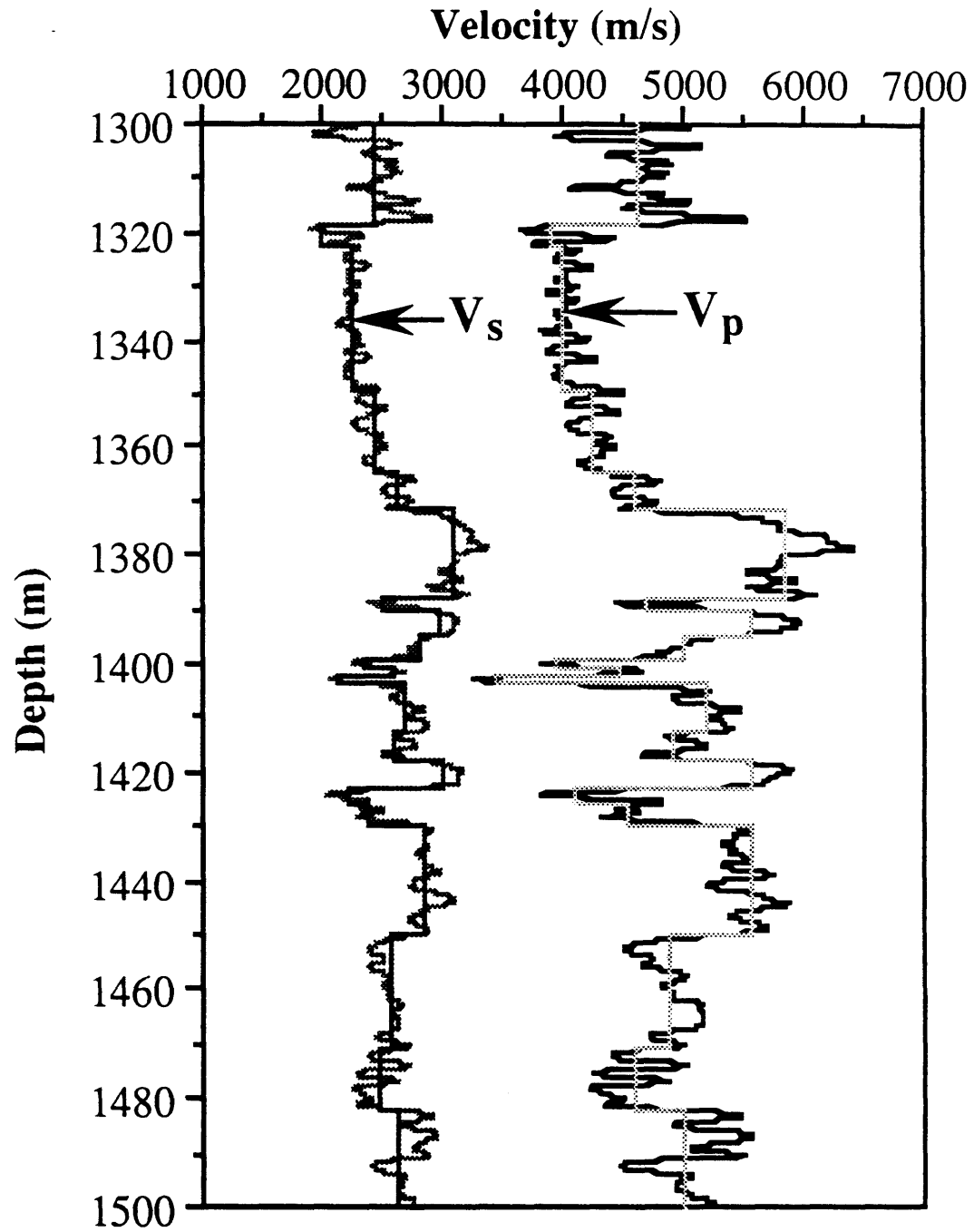


Figure 3.1: Blocked full-waveform velocity log of the Midale field data.

$$t^o = \sum_{k=i}^n \frac{\Delta z_k}{v_k [1 - p^2 v_k^2]^{\frac{1}{2}}}, \quad 3.2$$

where v_k is the interval velocity of layer k , Δz_k is the vertical distance of the ray in layer k , and p is the ray parameter,

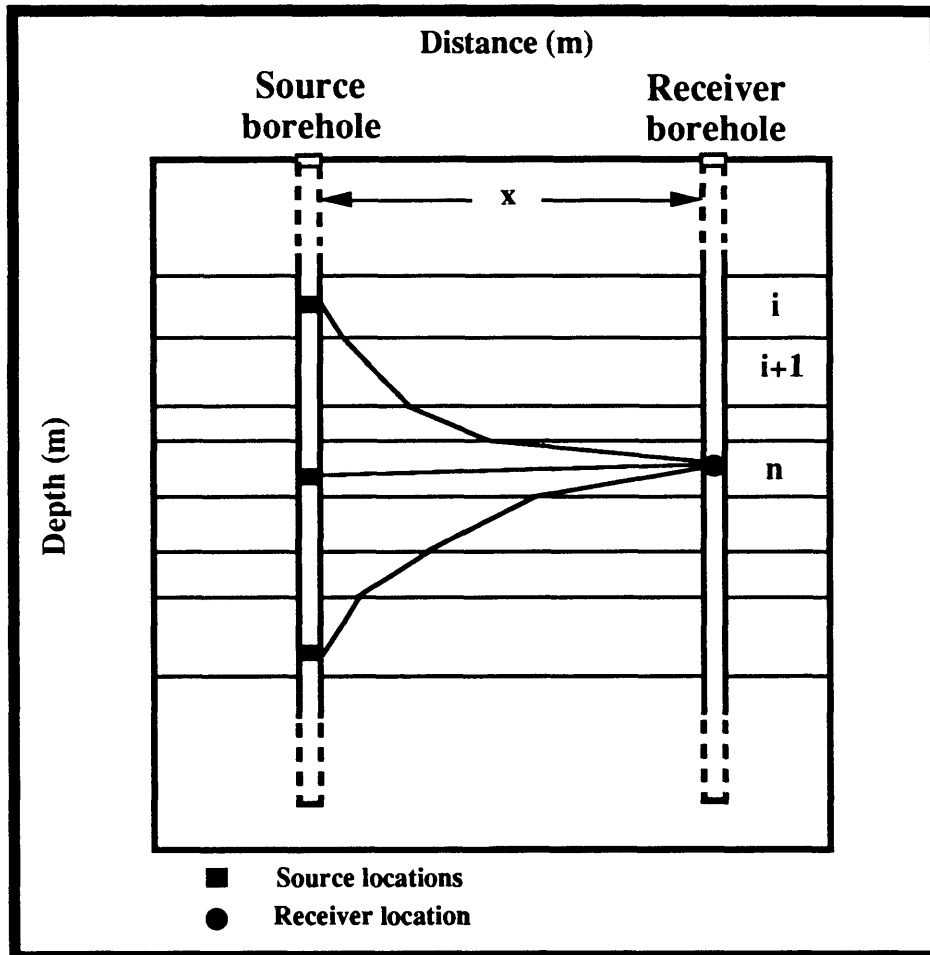


Figure 3.2: Layer-stripping via raytracing inversion geometry. x is the distance between boreholes. Receiver is in layer n while source is in layer i .

$$p = \frac{\sin \theta_k}{v_k} = \text{constant}, \quad i \leq k \leq n, \quad 3.3$$

where θ_k is the angle between the ray in layer k and the vertical.

The algorithm starts solving for the velocity of the interval in which both source and receiver are located. Then, from the receiver layer outward (upward and downward), the program proceeds solving for subsequent intervals using the previously calculated interval velocities. Thus, the method requires at least one direct arrival traveltime in the interval for which the velocity is to be estimated. Also, there are as many solutions for the same interval as there are sources located in it. This next section presents the derivation of the inversion technique and the use of numerical and statistical methods to find the desired solution.

3.3 Inversion formulation

There are basically two formulations in this scheme of inversion-via-raytracing. A straight raypath calculation is first performed to estimate the velocity for the layer in which the receiver and source(s) are located. That is

$$v_n = \frac{\sqrt{\Delta z_n^2 + x^2}}{t^o} \quad 3.4$$

Following this estimation, a bending raypath calculation (obeying Snell's law) is applied to all other sources (rays) located in layers outside the receiver layer. An example of a downgoing raypath from the layer i (source) to layer n (receiver) is shown in Figure 3.2. It is assumed that the velocities of layers n up to $i+1$ have been determined and it is desired to solve for the interval velocity of layer i . Also, for simplicity, reciprocity is assumed: source and receiver positions are interchangeable with respect to traveltime.

Now, consider the difference terms between the total raypath and the raypath only up to the layer before layer i ,

$$\Delta x_i = x - \sum_{k=n}^{i+1} \frac{p v_k \Delta z_k}{[1-p^2 v_k^2]^{\frac{1}{2}}}, \quad 3.5$$

and

$$\Delta t_i = t^o - \sum_{k=n}^{i+1} \frac{\Delta z_k}{v_k [1-p^2 v_k^2]^{\frac{1}{2}}}. \quad 3.6$$

From 3.1 and 3.2, we know that

$$\Delta x_i = \frac{p v_i \Delta z_i}{[1-p^2 v_i^2]^{\frac{1}{2}}}, \quad 3.7$$

and

$$\Delta t_i = \frac{\Delta z_i}{v_i [1-p^2 v_i^2]^{\frac{1}{2}}}. \quad 3.8$$

Solving for v_i by dividing 3.7 by 3.8

$$v_i = \sqrt{\frac{1}{p} \frac{\Delta x_i}{\Delta t_i}}, \quad 3.9$$

and multiplying 3.7 and 3.8 gives

$$\Delta x_i \Delta t_i = \frac{p \Delta z_i^2}{1-p^2 v_i^2}, \quad 3.10$$

$$\Rightarrow \Delta z_i = \sqrt{\Delta x_i \Delta t_i p^{-1} - \Delta x_i \Delta t_i p v_i^2}. \quad 3.11$$

Substituting 3.9 in 3.11

$$\Delta z_i = \sqrt{\Delta x_i \Delta t_i p^{-1} - \Delta x_i^2}. \quad 3.12$$

The term Δz_i is known (call it δz_i to denote the true vertical distance of the ray in layer i) since the model interface locations and source/receiver locations are parameters given to the inversion procedure. The idea here is to estimate \mathbf{p} so that it can be used in computing Δx_i and Δt_i in 3.5 and 3.6 respectively such that equation 3.12 holds. Once this is achieved, the raypath is completed and the interval velocity can be obtained from equation 3.9.

Consider the error function

$$\mathbf{E}(\mathbf{p}) = \delta z_i - \Delta z_i(\mathbf{p}), \quad 3.13$$

where δz_i is the known term and $\Delta z_i(\mathbf{p})$ is the term computed from the estimated \mathbf{p} . That is

$$\Delta z_i(\mathbf{p}) = \sqrt{\Delta x_i \Delta t_i \mathbf{p}^{-1} - \Delta x_i^2}. \quad 3.14$$

We require a solution for the equation

$$\mathbf{E}(\mathbf{p}) = 0, \quad 3.15$$

where \mathbf{p} is a root of the function \mathbf{E} . To find that root, the Newton-Raphson (Newton's) method is implemented (Hamming and Feigenbaum, 1971; Burden and Faires, 1985). Assume that Figure 3.3 represents the relation between the error function $\mathbf{E}(\mathbf{p})$ and the ray parameter \mathbf{p} . The idea behind the method is to fit a tangent line to the curve of the function at the point of the

current estimate p_n of the zero. As seen in Figure 3.3, the zero p_{n+1} of the tangent line T_1 provides the next guess for the zero of the function. In mathematical notation, let p_n be the current guess then the tangent line is represented by

$$\xi(p) = E(p_n) + E'(p_n) (p - p_n), \quad 3.16$$

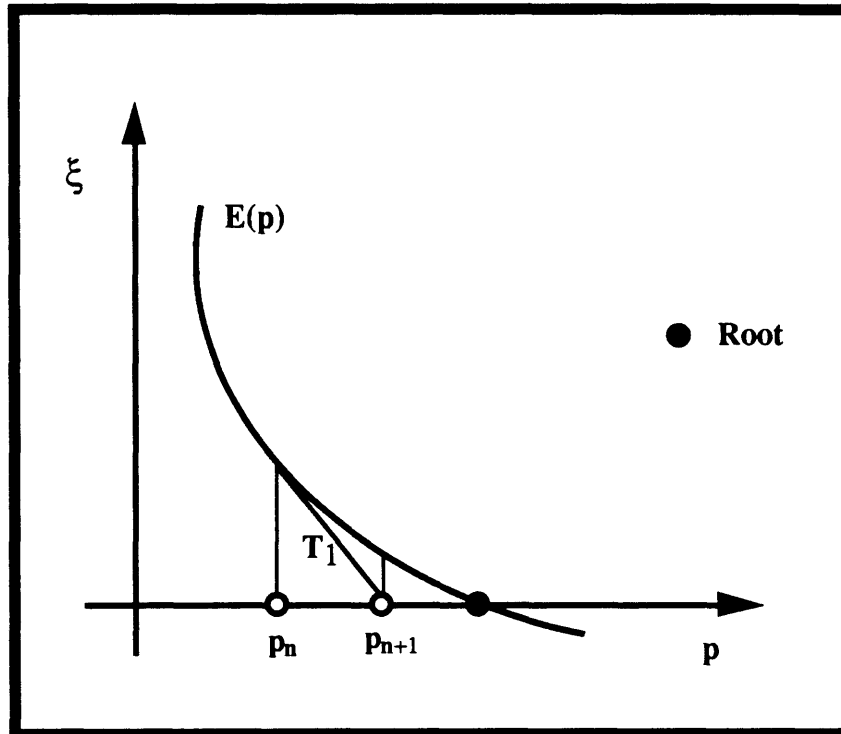


Figure 3.3: Geometrical representation of Newton's method for finding the real root of function $E(p)$.

and the value where $\xi(p) = 0$ is $p = p_{n+1}$ where:

$$0 = E(p_n) + E'(p_n) (p - p_n), \quad 3.17$$

$$\Rightarrow p_{n+1} = p_n - \frac{E(p_n)}{E'(p_n)}. \quad 3.18$$

This formula provides a method of going from \mathbf{p}_n to \mathbf{p}_{n+1} . This calculation of a new ray parameter (\mathbf{p}_{n+1}) involves some mathematical implementations which can be summarized as follows. The error function of the current guess can be obtained from equation 3.13 where we know δz_i , the exact vertical distance of the ray in layer i , and can compute $\Delta z_i(\mathbf{p})$ from equation 3.14. Also, the differentiation of the error function can be evaluated analytically by

$$\frac{d}{d\mathbf{p}} E(\mathbf{p}) = - \frac{d}{d\mathbf{p}} \Delta z_i(\mathbf{p}), \quad 3.19$$

$$\Rightarrow \frac{d}{d\mathbf{p}} E(\mathbf{p}) = - \frac{d}{d\mathbf{p}} \left\{ \sqrt{\Delta x_i \Delta t_i \mathbf{p}^{-1} - \Delta x_i^2} \right\}. \quad 3.20$$

We can see that the relation between $\Delta z_i(\mathbf{p})$ and \mathbf{p} is nonlinear since Δx_i and Δt_i (equations 3.5 and 3.6 respectively) are functions of \mathbf{p} themselves. So, differentiation of Δx_i and Δt_i with respect to \mathbf{p} is also required in evaluating equation 3.20. Undertaking this process gives

$$\frac{d}{d\mathbf{p}} E(\mathbf{p}) = \frac{1}{2} \gamma^{\frac{1}{2}} \left[\Delta x_i \Delta t_i \mathbf{p}^{-2} - (\Delta x_i - \Delta t_i \mathbf{p}^{-1}) \sum_{k=n}^{i+1} \frac{\mathbf{v}_k \Delta z_k}{[1 - \mathbf{p}^2 \mathbf{v}_k^2]^{\frac{3}{2}}} \right], \quad 3.21$$

where $\gamma = \Delta x_i \Delta t_i \mathbf{p}^{-1} - \Delta x_i^2 = \Delta z_i^2$. Finally, substituting equations 3.13 and 3.21 in equation 3.18 and simplifying results

$$\mathbf{p}_{n+1} = \mathbf{p}_n - \frac{2 [\delta z_i \gamma^{\frac{1}{2}} - \gamma]}{\left[\Delta x_i \Delta t_i \mathbf{p}_n^{-2} + \gamma \Delta x_i^{-1} \sum_{k=n}^{i+1} \frac{\mathbf{v}_k \Delta z_k}{[1 - \mathbf{p}_n^2 \mathbf{v}_k^2]^{\frac{3}{2}}} \right]}. \quad 3.22$$

The first guess of the ray parameter for every source/receiver pair is always taken from the ray parameter solved for the previous source/receiver pair. In an iteration, the current estimate of the ray parameter is used to evaluate $\Delta z_1(\mathbf{p})$ (equation 3.14) by calculating Δx_1 and Δt_1 . Then, a check for satisfying the capturing of the raypath is performed by equation 3.13 where we impose a tolerance of 0.1 cm (1 mm) to consider the ray captured at the receiver location. If the error tolerance is not met then the next iteration is undertaken and so forth until the ray is captured with the required tolerance. Note that the solution for the interval velocity is directly obtained from equation 3.9 once the ray parameter is accurately estimated. This may be seen as an appealing feature of this method over least-squares methods which involve matrix inversions and perturbations of model velocities to fit the arrival times.

If there is more than one solution for the interval velocity (more than one source per layer), then the median of the velocity values is selected to be representative velocity of that interval. That is if the number of values is odd. If the number is even, then the mean of the two middle values is taken to be the interval velocity. The decision of selecting the median value was taken among other choices of computing the mean of all values and the mean of a selection of values based on a 1.28 standard deviation interval. Further discussion about selecting a representative velocity is provided in the next section where inversion results are presented.

3.4 Inversion results

Using synthetic data generally helps in evaluating and enhancing computational techniques. Synthetic-generated data in the form of direct traveltimes are used to examine the accuracy of the inversion algorithm and the effect of errors (noise) on its solution. Specific approaches within the computational technique can also be investigated to select the approach that gives the best result.

Following the synthetic data examples, inversion of real crosswell data from the Midale field is presented. The computed velocity functions are then compared to their corresponding sonic logs. Finally, forward modeling using the inverted velocities is performed to analyze the differences between the observed and computed traveltimes.

3.4.1 Synthetic data examples

The traveltimes used in this section are generated by theoretical ray tracing through the model velocity section (Figure 2.5) for a source located at a depth of 116 m and receivers from 96 m to 158 m with a 2 m receiver interval. As discussed in section 3.3, the inversion method attempts to solve for the velocity of each interval that contains at least one receiver (or source depending on the gather type). So, from Figure 2.5, the intervals for which velocity solutions are desired start with layer number 3 (4600 m/s) and run to layer number 7 (4900 m/s). This would cover the depth interval from 95 m to 166 m. The objective in this section is to determine what accuracy the algorithm can offer in the presence of traveltime error. It is also of interest to find the best possible way to avoid such error problems.

First, consider noise-free traveltimes. This tests the derivation and the programming of the method. Figure 3.4 shows the results of inverting such traveltimes. There are actually two blocked curves, the input and inverted velocity functions, displayed in this figure. The solution is correctly estimated (within 0.7 m/s). The accuracy of the inversion method is based on the direct relationship (equation 3.9) between the interval velocity v_i and the ray parameter p . That is, the interval velocity is calculated directly once the ray parameter is accurately estimated.

In the next case, there is a picking error of up to 0.2 ms (two sample points). The inversion of such data produced an incorrect velocity estimate at each location where a timing error was introduced. Depending on whether the error is added or subtracted, the velocity estimate decreases or increases, respectively, from the true interval velocity. Ordering these velocity estimates in each interval, then selecting the median value, moves the incorrect estimates to either end of the sequence and chooses the correct velocity value for that interval. The result of this type of computational scheme is shown in Figure 3.5 where the true solution was well recovered. The possibility of obtaining the perfect solution

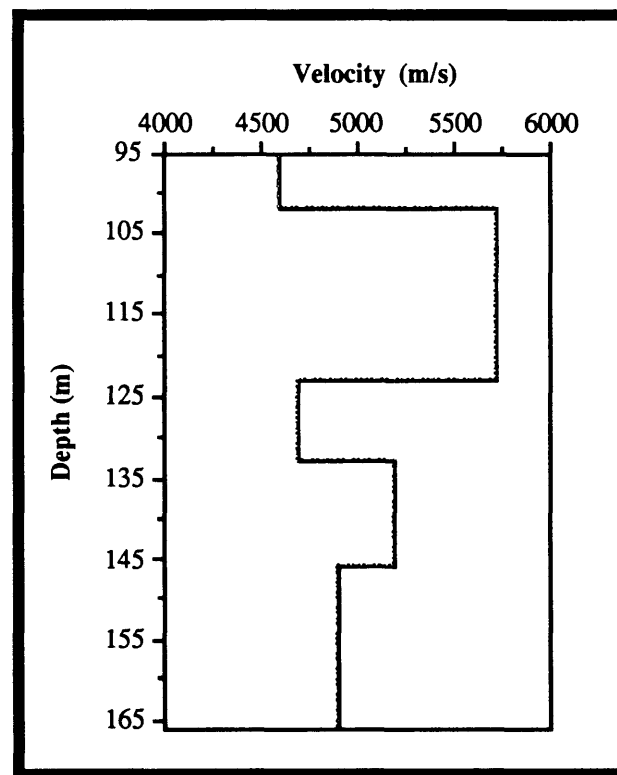


Figure 3.4: Inversion of synthetic data with no errors introduced. The two curves, true and estimated velocity functions, match well.

decreases if more timing errors are introduced particularly when the errors are only on one side (either added or subtracted). Another scheme is to compute the mean of the estimated velocities in every layer. However, when timing errors are present, the mean computation

always produces inaccurate velocity estimates. The scheme of selecting the median velocity value shows better performance than that of the mean calculation and therefore is used to obtain the velocity solutions in this inversion method.

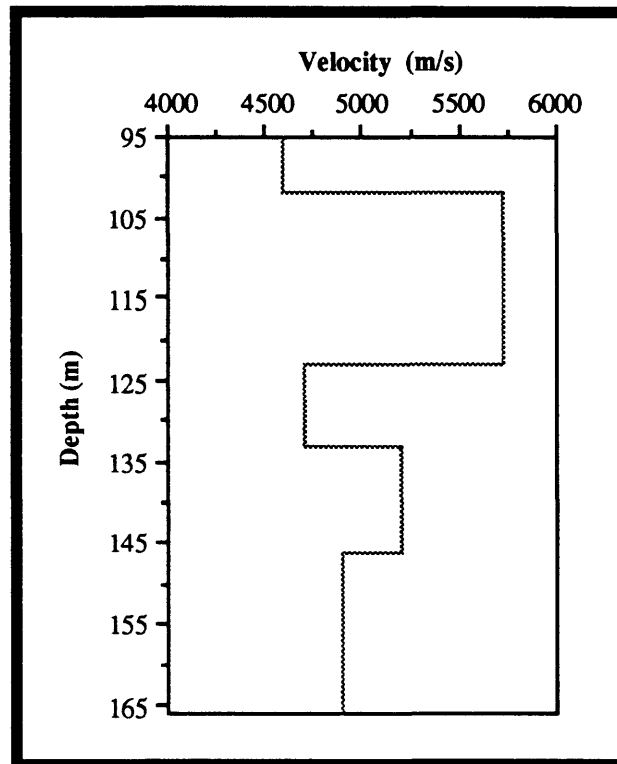


Figure 3.5: Inversion of synthetic data with an isolated error in each interval. The two curves, true and estimated velocity functions, again match well.

In the following case, a uniform timing error (1 sample point) is introduced in all the observed traveltimes. This represents the case where the picks are not taken exactly on the onset of the direct arrival. Figure 3.6 shows the inversion results of such data. The consistent error was negative corresponding to earlier arrivals than the correct ones which caused a consistent increase of the velocity function estimated (dotted block-curve) with respect to the true velocity function (solid block-curve). However, even with such an error, the velocity model is well constructed with respect to the true solution. Of course, the larger

the uniform error is, the greater the difference between the estimated and the true velocity functions.

A final case considered here is when random noise from -0.2 ms to 0.2 ms (2 sample points) is mixed with all the traveltimes. Figure 3.7 shows the estimated velocity function (dots) when every input time is contaminated with a random number. The overall solution is quite reasonable except the deepest interval where there is a difference of 173 m/s between the estimated (5073 m/s) and the true velocity (4900 m/s). However, this

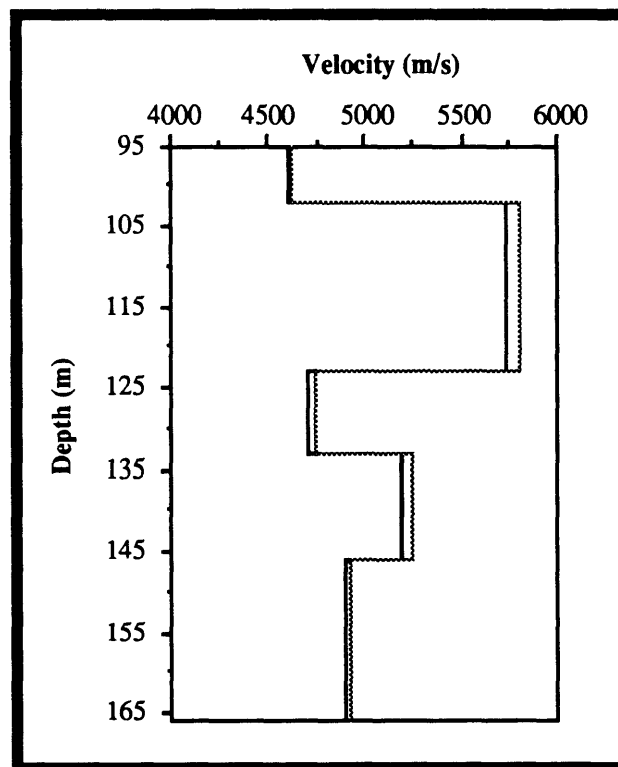


Figure 3.6: Inversion of synthetic data with a uniform error in all the picks. There is a consistent error in the estimated velocity function (dots) with respect to the true solution (solid).

difference may still be acceptable as it represents only 3.5 percent of the true interval velocity. One interesting observation is the accuracy of the estimates of the velocities in the first, second, and fourth intervals despite the presence of random errors (Figure 3.7). This

may be due to two features. First, there may be a small error at a particular point and second, the selection of the median of the interval values may lead to a highly accurate velocity estimate .

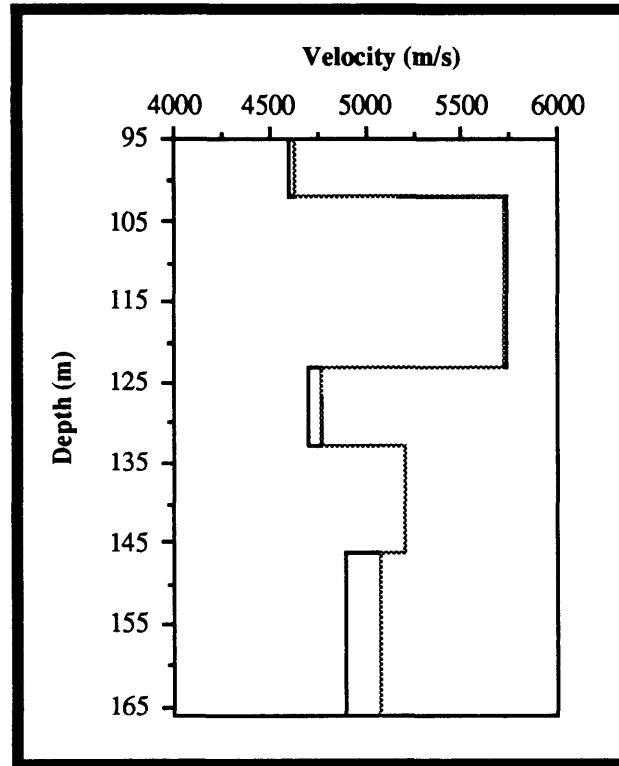


Figure 3.7: Inversion of synthetic data with a random error in all the picks. The dotted curve is the estimated velocity function while the solid one is the true solution.

In the above cases where an isolated error in every interval (second case) and random errors in all the picks (fourth case) are introduced, performing the inversion on every point is shown to be of advantage in selecting the optimum solution with the least timing errors present in the data. Having discussed the foregoing cases and gained an insight to the accuracy and sensitivity of the algorithm, we can now direct our attention to the inversion of real data from the Midale field.

3.4.2 Field data inversion

The parameters used in collecting the crosswell field data are described in section 2.5. Also, examples of trace-equalized receiver gathers 2, 5, and 8 are shown respectively in Figures 2.11 to 2.13,. Each of these records represents a group of three gathers that have similar quality of data acquired. The critical dependence of traveltimes inversion on the timing picks has led me to consider only the three gathers of the first group which is represented by gather number 2 (Figure 2.11). The confidence of picking the direct traveltimes on gather 2 is much higher than that on gathers 5 and 8 (Figures 2.12 and 2.13). This is due to the coherent and continuous arrivals present in the first group of gathers as opposed to those of the other two groups. Aside from possible acquisition discrepancies and by referring to Figure 3.1, the receivers of the first group, as presented in section 2.5, are all located in zones of high velocity compared to that of the surrounding zones. This is interpreted to be the primary reason for the presence of the direct arrivals as the first arrivals which are in turn picked as input for the inversion procedure. On the other hand, receiver number 5 (second group) exhibits discontinuous direct arrivals due to the presence of head waves in both P- and S-wave arrivals (Figure 2.12). Finally, the direct arrivals in receiver number 8 (third group) are of lower coherency and continuity (Figure 2.13) than those of receiver number 2 (Figure 2.11) particularly the S-wave arrivals.

From the previous discussion, it was decided that the traveltimes inversion of this study would be based on the three gathers of the first group. The other input component to the inversion algorithm is a depth model of the subsurface layering that contains source/receiver locations. From the source locations of the three gathers, the depth model extends from 1372 m to 1413 m. The model boundaries (layer interfaces) were then obtained using the full-waveform sonic information along with the prior information, provided by Shell Canada staff, about the lithology of the subsurface in the area. The top of the model is composed of the Ratcliffe beds, generally anhydrite interbedded with a thin

shale layer, then the upper Midale beds, dolomite, followed by the lower Midale beds, limestone.

Inverting the P- and S-wave arrivals of the three receiver gathers independently and overlaying the results according to the model boundaries gives Figures 3.8 and 3.9 respectively. The algorithm generally takes 3 iterations for a velocity estimate. Less than

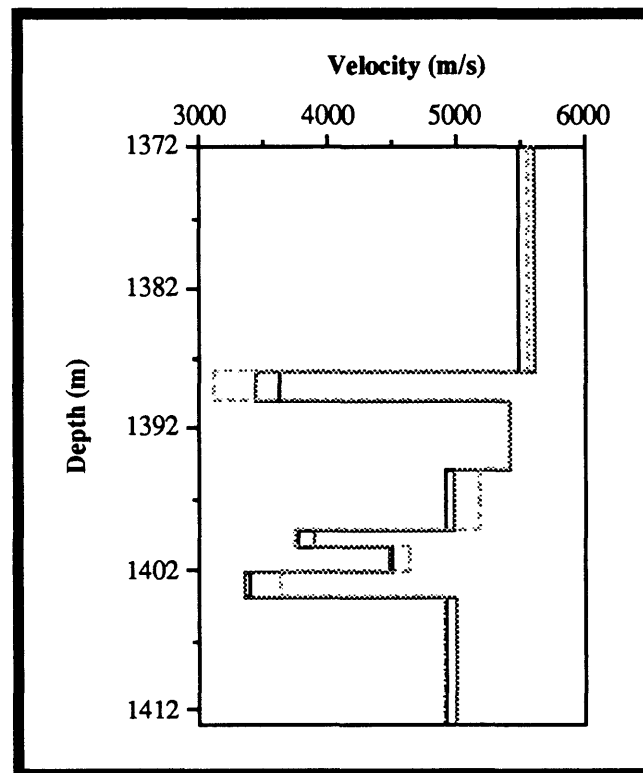


Figure 3.8: P-wave inversion of three independent receiver gathers.

half a minute (about 25 s) is needed to compute the velocities for an average of 390 points on a Zenith-AT personal computer. One observation here is the consistency of the three independent results for each wave type. In each interval of both cases, the estimated velocities lie within a reasonable range (around 200 m/s) except for the thin shale interval (1388 m to 1390 m) in the S-wave inversion (Figure 3.9) where one estimate was

significantly higher than the other two estimates. Ultimately, the median value of every three estimates in the same zone would be selected to represent the velocity of this interval.

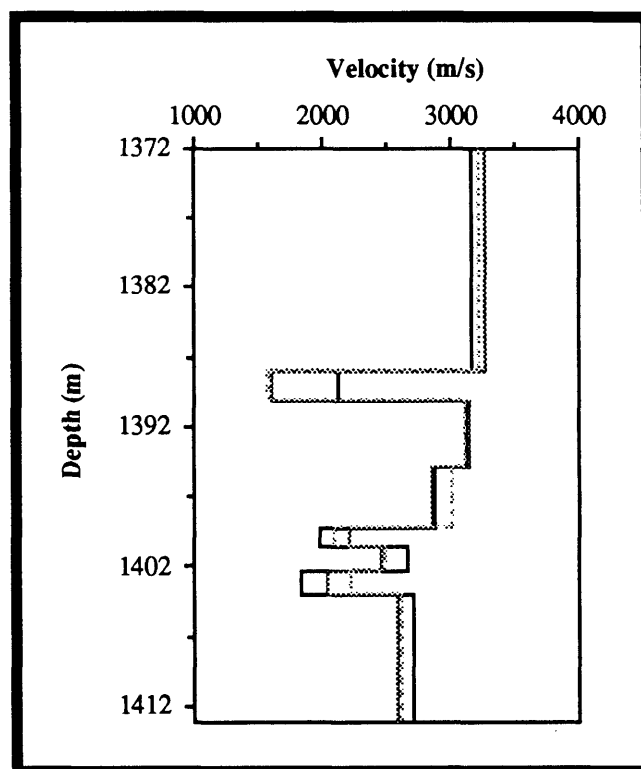


Figure 3.9: S-wave inversion of three independent receiver gathers.

To evaluate the inversion solutions, the constructed 1-D P- and S-wave interval velocity functions are displayed against the full-waveform velocity log recorded in well FS-1 (Figure 3.10) where the sources were placed. There is quite good agreement between the seismic and the sonic velocities in all the zones of the model except again at that thin shale layer. Had we chosen the higher velocity estimates in both P- and S-wave inversions of that interval, they would have agreed better with the sonic velocities. But that would not be consistent with the median selection scheme. The algorithm used here does not appear to have an instability problem in thin layer cases. Every interval of the upper Midale

Formation (1399 m - 1404 m) is thinner than the shale layer. Yet, the estimated velocities of these intervals are well in the range of the sonic velocities. The direct explanation to that difference of velocity is not completely known. However, a series of possible factors can be contributing to its presence. Firstly, core samples taken from well FS-1 by Shell Canada suggested that this shale layer has a thickness less than 1 m which puts in doubt the sonic readings of this zone as the log might not have resolved it. Secondly, as mentioned in section 2.5, the locations of the source/receiver array elements are not confirmed from the field experiment. This might introduce velocity estimation errors, particularly since the locations of the receivers in this group are around 1392 m, very close to the shale layer. Another possible explanation to that velocity discrepancy is that the sonic log depends on vertical transmissions while the seismic (crosswell in this case) depends on nearly horizontal transmissions. The thin interval is known to be of shale lithology, and some shale is known to be anisotropic whereby the velocity in the vertical direction is different from that in the horizontal direction (Banik, 1984). Finally, the raypath in this zone might be more complex than just a direct path from the source to the receiver, in which case the algorithm used can give false estimates. However, this is unlikely to be the source of the problem as it would be shown later in forward modeling and error analysis.

Another type of analysis is to take the estimated velocity of every interval and generate, based on raytracing, forward-modelled direct arrivals for the geometry of the crosswell experiment. Then, compare the produced traveltimes to those originally observed (picked) on the real records. This would provide the response of the estimated (1-D) interval velocity with respect to the recorded data. Figures 3.11 and 3.12 show the comparison of the computed times with the observed ones. The raytracing algorithm implements the same two equations 3.1 and 3.2 discussed in section 3.2. The algorithm uses Newton's method in a forward modeling manner to capture the rays at the correct receiver location, within 0.1 cm (1 mm) tolerance. It usually takes the raytracing algorithm

3 iterations to correctly compute the traveltime of the direct arrivals. A receiver gather of 390 rays (source locations) takes less than half a minute of simulation on a Zenith-AT personal computer.

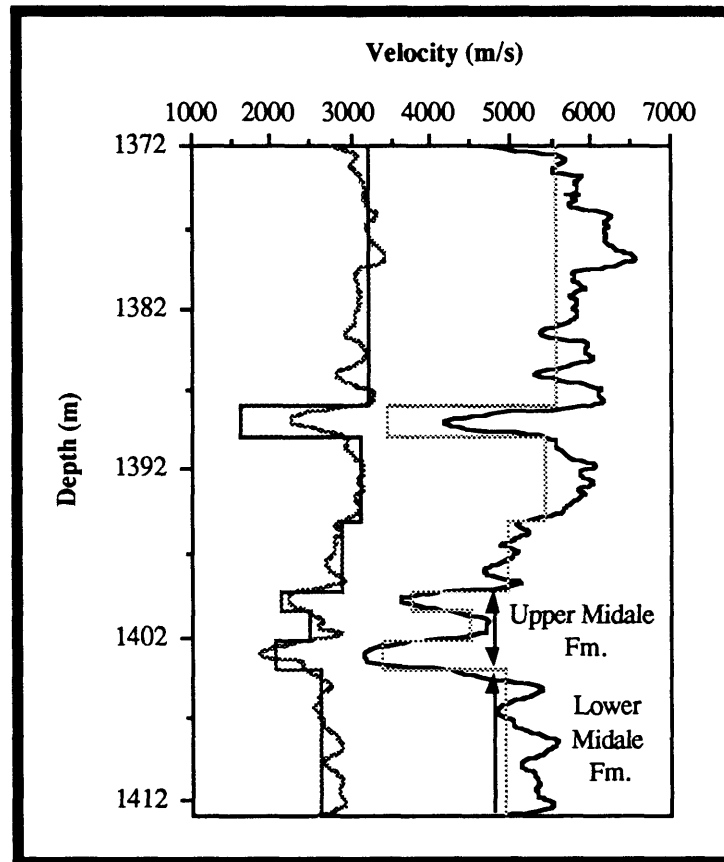


Figure 3.10: Comparison of P- and S-wave inversion results with the respective full-waveform velocity logs.

The results of forward modeling (Figures 3.11 and 3.12) are in good agreement with the recorded times. Both Figures are consistent within themselves and even have the same behavior compared to each other in matching the observed times. At a depth of approximately 1388 m (the top of the thin shale unit), there is a drift between the traveltimes up to about 1386.5 m. It is tempting to infer that the correct timing trend was missed while performing the interactive picking process. The agreement that follows the drift confirms that the estimated velocity is the correct answer since the zone from 1388 m

and above to 1372 m represents only one layer in the model. Another explanation to consider is that if the observed traveltimes in the drift zone were correct, then they perhaps represent head waves that arrive earlier than the direct waves. They are followed (at depth about 1385 m and up) by the direct waves arriving first where the agreement between the observed and computed traveltimes recovers again.

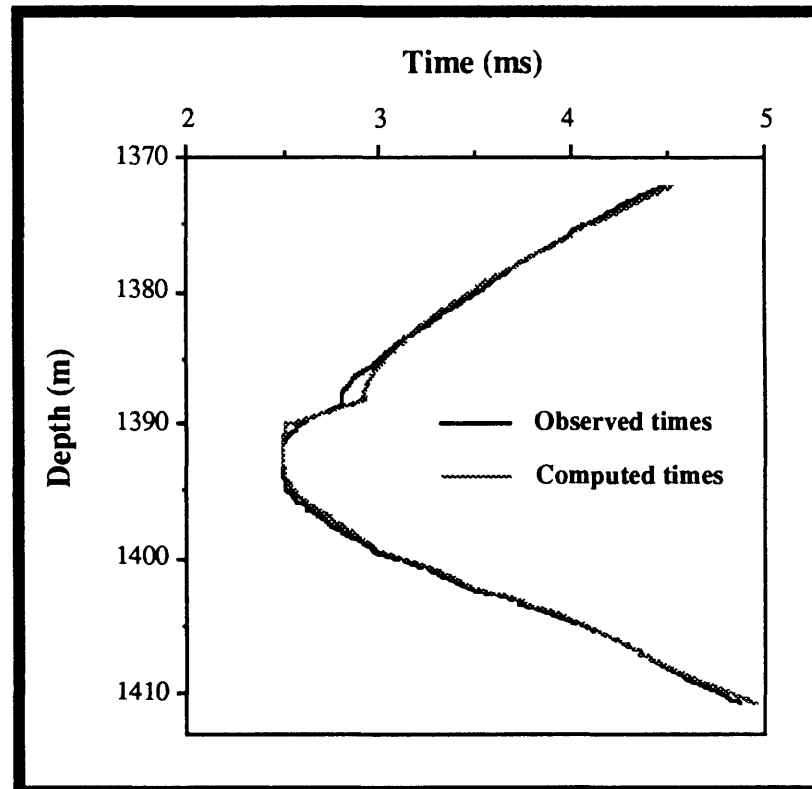


Figure 3.11: Comparison of the P-wave observed and computed direct arrivals. The computed traveltimes are obtained by forward modeling using the estimated velocities from the inversion.

A final effort to study the inversion results is to look at the residual average error in every interval. This is done by computing the average error magnitude of the observed and computed traveltimes. Figures 3.13 and 3.14 show such error analysis for the P- and S-wave inversions respectively. The solid curve represents the local error magnitude at every source point while the dotted (block) curve shows the average error of the local points in

every interval. The largest average error can be seen in the S-wave case (Figure 3.14) for the top interval (1372 m - 1388 m) where the error is computed to be 0.0584 ms. That

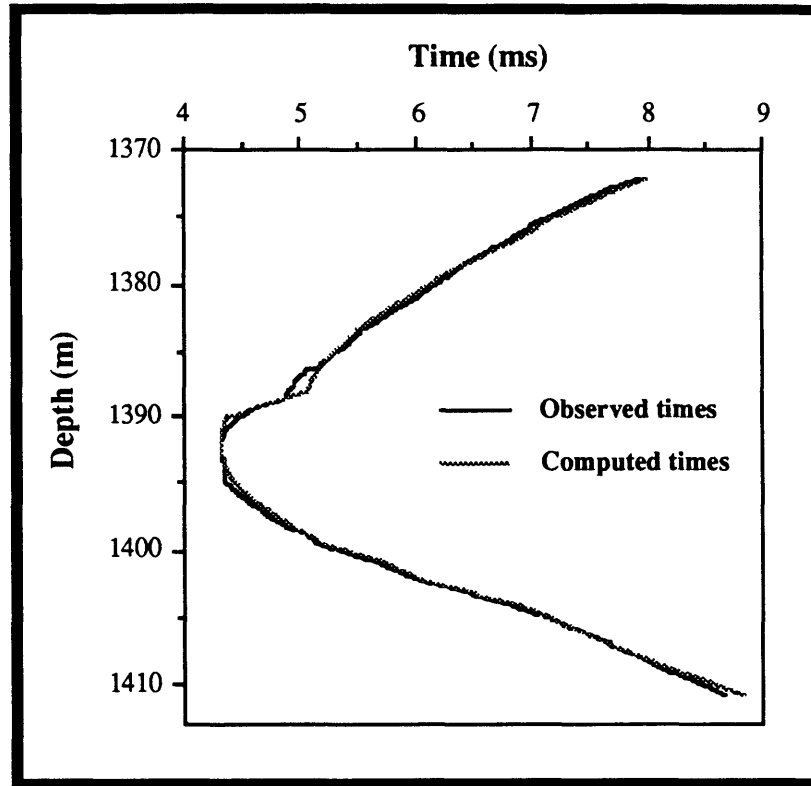


Figure 3.12: Comparison of the S-wave observed and computed direct arrivals. The computed traveltimes are obtained by forward modeling using the estimated velocities from the inversion.

average error was found to represent 0.936 percent of the average observed traveltime in the respective interval. Similar computations for the percent of the average error with respect to the average observed traveltime in all intervals of both P- and S-wave cases were carried out and found that the maximum relative error was 1.45 % in an interval in the P-wave case. Finally, note that in most of the intervals of Figures 3.13 and 3.14, the local error is minimum in areas at and around the middle. The estimated velocities were found to be picked by the algorithm from such areas.

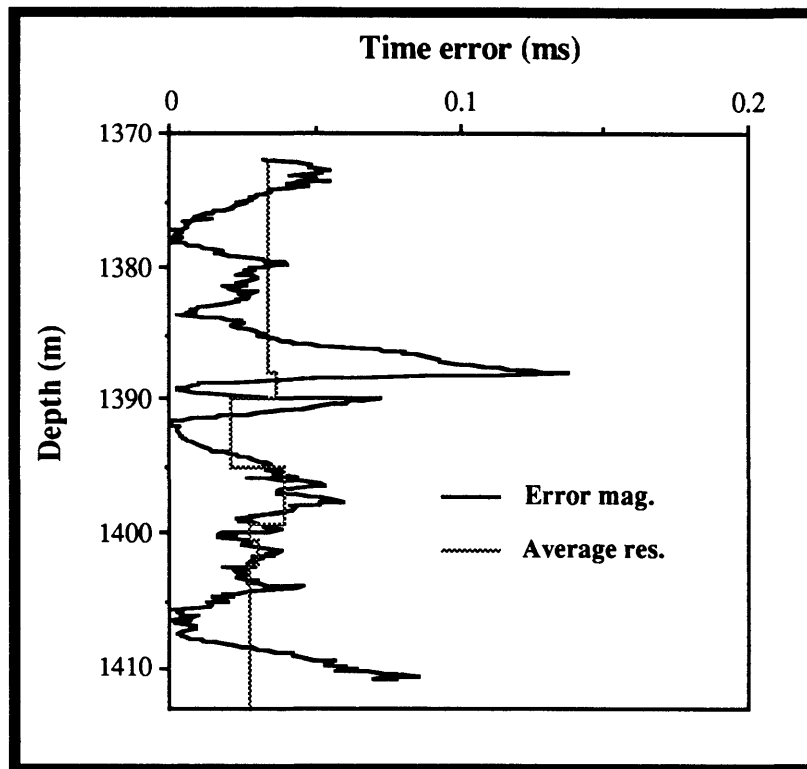


Figure 3.13: The magnitude of the local error between the observed and computed P-wave traveltimes of Figure 3.11. Also plotted is the average residual error in every interval.

3.5 Lithologic characterization

The P- and S-wave velocities obtained from the inversion (previous section) are plotted against each other in Figure 3.15. The points shown in the figure represent the velocity solutions for the assumed model intervals. Annotated in the figure is the lithology of each unit for which velocities were obtained. Despite the limited number of points, there is a general linear relationship between the P- and S-wave velocities that has been introduced by Pickett (1963) and also discussed by several other authors (Tatham and Stoffa, 1976; Castagna et al., 1985; Miller and Stewart, 1990). Efforts in lithologic characterization using the ratio of the P- and S-wave velocities (V_p/V_s) were also demonstrated in Pickett (1963), Rafavich et al. (1984), and Miller and Stewart (1990). Figures 3.16 and 3.17 show the relation of V_p/V_s with V_p and V_s , respectively, for the

results in Figure 3.15. The purpose of computing the ratio here is to compare its results with those observed in previous studies. In other words, this procedure is used to see how the inversion results fit in with measurements already available for similar lithologies.

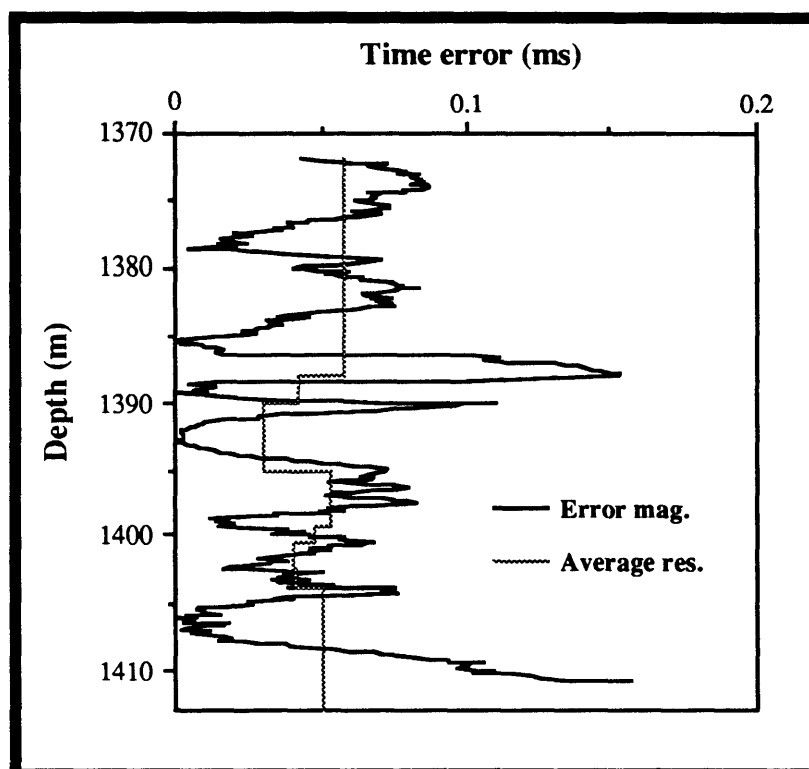


Figure 3.14: The magnitude of the local error between the observed and computed S-wave traveltimes of Figure 3.12. Also plotted is the average residual error in every interval.

In Figures 3.16 and 3.17, the V_p/V_s ratio for the anhydrite unit (interbedded with shale and dolomite) is around 1.73. This value is in the range of the findings of Rafavich et al. (1984) where the anhydrite ratio ranges from 1.71 to 1.84. V_p/V_s estimates of 1.79 and 1.88 for porous dolomite and limestone respectively are in good agreement with all previously cited measurements, 1.80 for porous dolomite and 1.90 for porous limestone. V_p/V_s for the shale unit is computed to be 2.14 which is similar to that of Castagna et al. (1985), Ostrander (1984), and Harrison (1989).

The results of this section provide a final analysis of the inversion solutions which are proven to be realistic and consistent with other independent measurements (well and lithology logs). The observations of this section should also help in obtaining lithological information from the crosswell data even if no logs are available for the area of the experiment.

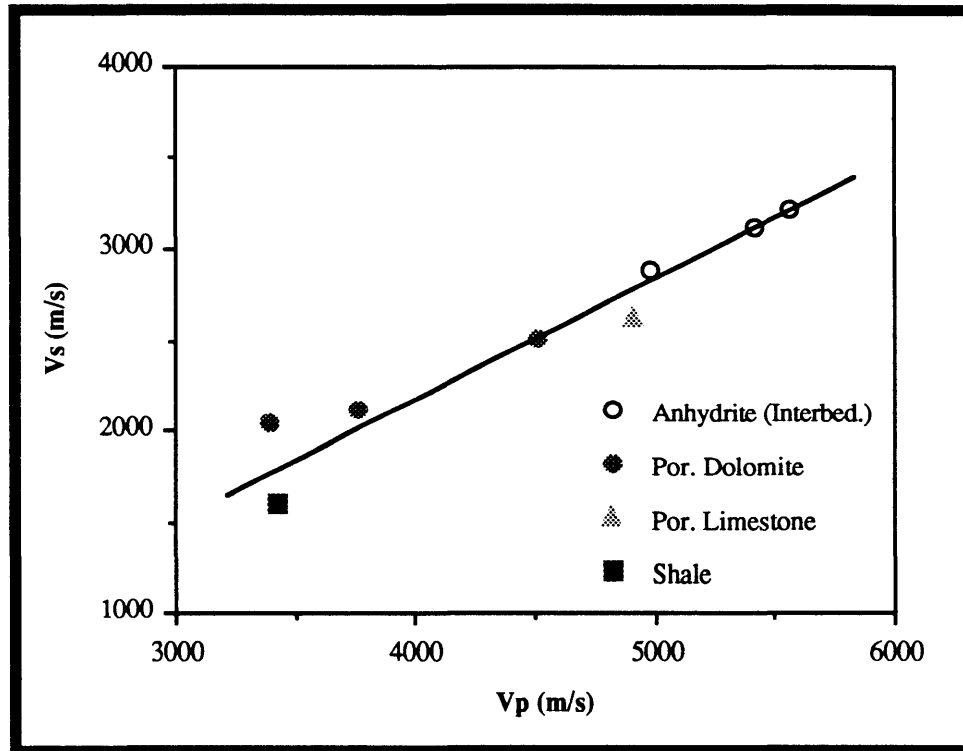


Figure 3.15: The relation between inverted V_p and V_s for the assumed model intervals. A linear relationship can generally be observed.

3.6 Conclusions

A simple inversion via raytracing is introduced here to obtain 1-D velocity functions of P and S waves in the subsurface area between the boreholes. The algorithm operates on every point and then attempts to choose the solution that best represents the interval velocity. Only three iterations are usually needed to reach a solution at every point. An entire run of the program, inverting about 390 points, takes about one half of a minute.

The velocities are solved by a direct relationship with the estimated ray parameter.

Synthetic data inversion offered some insights to the proposed algorithm in terms of accuracy and computational schemes. Operating on every point independently results in selecting the optimum solution that is least affected by timing errors present in the data even if these errors were random.

Inverting traveltimes of three independent gathers provided P- and S-wave results within a range of 200 m/s except one interval, the Ratcliffe shale bed, where one estimate was significantly faster than the other two estimates. Because the source/receiver locations are not confirmed, the discrepancy here might be a result of such problems in the field experiment, in particular, that the shale interval is possibly just outside the receiver locations. In other words, any distance error would significantly affect the limited observed traveltime.

A series of inversion result evaluations were carried out starting with a comparison of the estimated velocities of P and S waves to those from the respective velocity logs. Both types of information, sonic and seismic, are in the same range for the most part. A discussion of one zone of disagreement between the two, in the same shale interval for P and S, was attributed to doubts in the reliability of the sonic log, unconfirmed locations, possible anisotropic effects in shale, and finally raypath complexity. The global response of the estimated velocities was then evaluated by comparing the forward modelled (computed) traveltime for every point with its respective observed (picked) traveltime. To quantify this comparison, the residual average error in every interval was in turn considered and the maximum relative error with respect to its average observed traveltime was found to be 1.45 % in an interval in the P-wave velocity function. Finally, a different type of

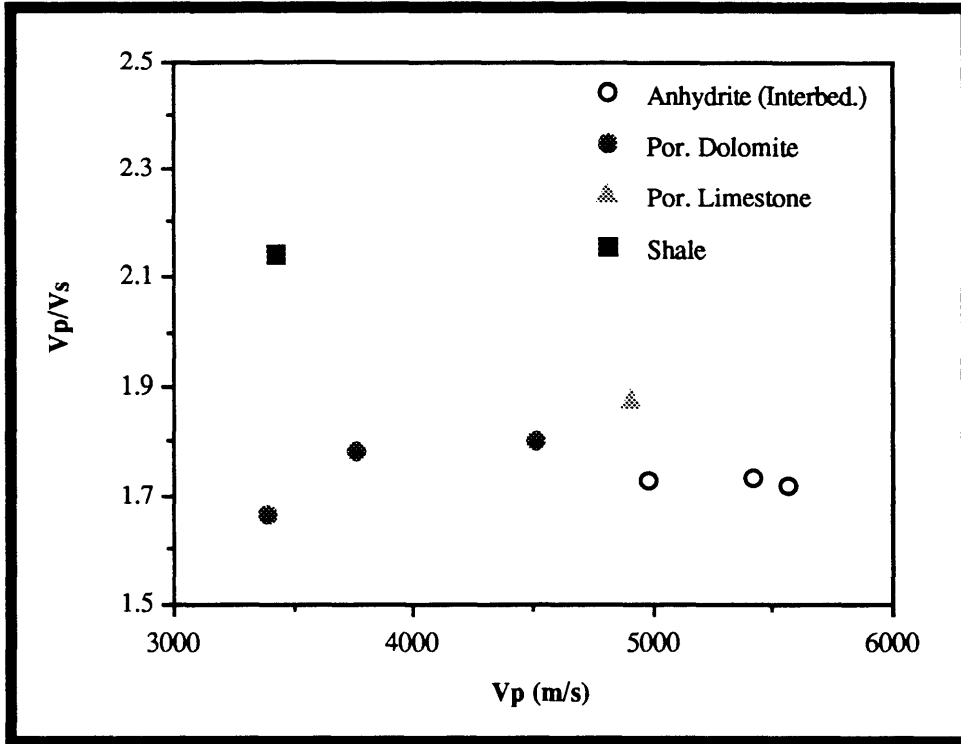


Figure 3.16: The relation between inverted V_p/V_s and V_p for the assumed model intervals.

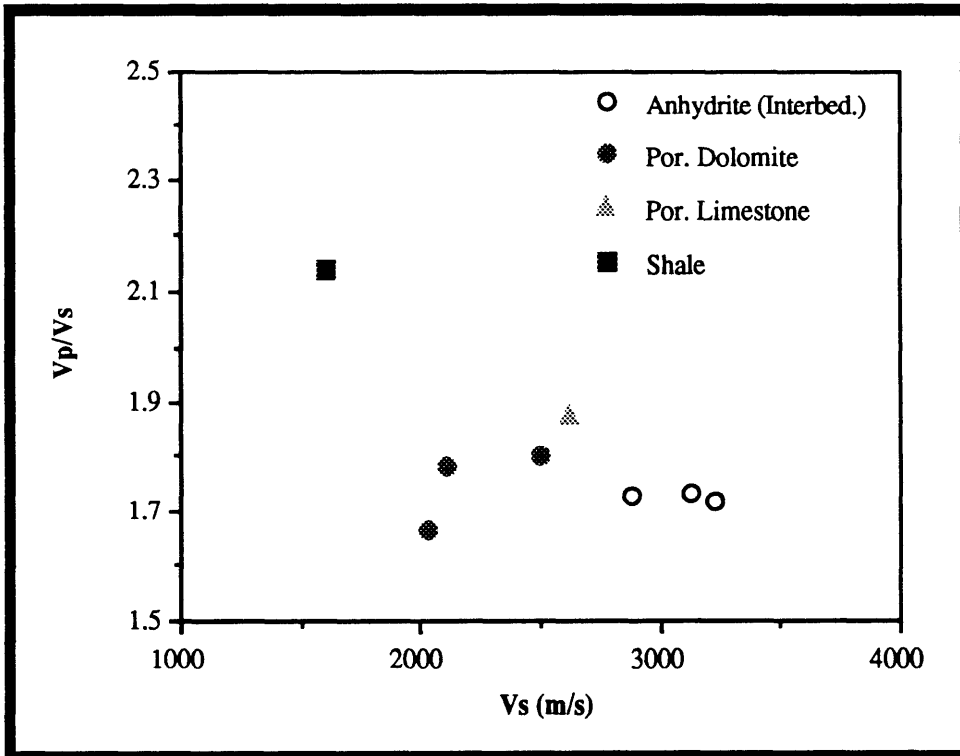


Figure 3.17: The relation between inverted V_p/V_s and V_s for the assumed model intervals.

evaluation was also conducted to check how the inversion results fit in with current measurements of V_p/V_s of the available subsurface lithology information. This provided another matching comparison which led to the confident acceptance of the inversion results in the form of 1-D velocity functions that would be used in the further processing steps of the later arriving reflected data.

Chapter 4 - Reflection processing

4.1 Introduction

Up to this point, only direct arrivals of P and S waves have been used to obtain information about the medium. The focus now is directed to the later arriving waves, namely, the reflected events.

As mentioned in the literature review (section 1.1), a few studies have considered back scattered data through different migration algorithms to construct depth sections for the area between the boreholes (Zhu and McMechan, 1988; Hu et al., 1988a; Beydoun et al., 1989). The depth sections produced from these studies suffered serious artifacts as a result of the migration process applied.

To my knowledge, Baker and Harris (1984) and Iverson (1988) are the only two studies that transformed crosswell reflected events from the domain of the field recording, i.e. receiver depth and time (z, t), to the domain of surface distance and subsurface depth (x, z) using the reconstruction technique of VSP data (Wyatt and Wyatt, 1984; Dillon and Thomson, 1984). This method makes use of both upgoing and downgoing reflections present in crosswell data in order to produce a depth section that is similar to the classic surface seismic section. The two studies, however, had a critical assumption: that is, the reconstruction was based on a constant-velocity model (straight raypath geometry). In the hydrocarbon-producing subsurface, velocities usually vary considerably. This would in turn result in considerable errors in depth placement of the reflectors.

This study is considered to be a continuation of the previous studies in terms of reflection processing of crosswell data. Effective wavefield separation techniques are implemented to enhance the reflected data. The crosswell coverage is introduced here based

on constant-velocity model expressions which provide general subsurface locations at which reflected wavefields evolved. Also, a proper transformation based on a multi-layer model is introduced. Due to limitations in some of the software to process data with such fine sampling in both synthetic (0.1 ms) and field data (0.008 ms), scale factors are used to make the data appear to be sampled at 1 ms. These scale factors do not affect any of the results obtained. The figures of such results were then relabeled using true scales.

Figure 4.1 presents the processing flow conducted in this study for both synthetic and field data. The following sections of this chapter consist of the presentation and discussion of the results of every processing step with detailed review if necessary.

4.2 Single-channel processing

The single-channel processing of synthetic data (3 source gathers) is limited to muting the direct arrivals, D , of Figures 2.6 to 2.8 since the focus here is on the reflected arrivals. Designing further processes, the median filter for example, is based on the reflected events themselves. No trace balancing is needed since the seismic wavelet is consistent for all the traces. The same applies for bandpass filtering as the data are noise free within the desired bandwidth.

The single-channel processing of the field data (9 receiver gathers) is, on the other hand, discussed in detail in section 2.5 where trace balancing (Figures 2.11 to 2.13) and bandpass filtering (Figures 2.14 to 2.16) results are shown and used in studying and identifying the different propagating wavefields. Muting the direct arrivals of P waves down to the start of the direct arrivals of S waves is performed following the bandpass filtering, as it is found in section 2.5 that the reflected events are limited to S -wave modes. So, from now on, processing and its associated analysis will be concerning only S -wave reflections.

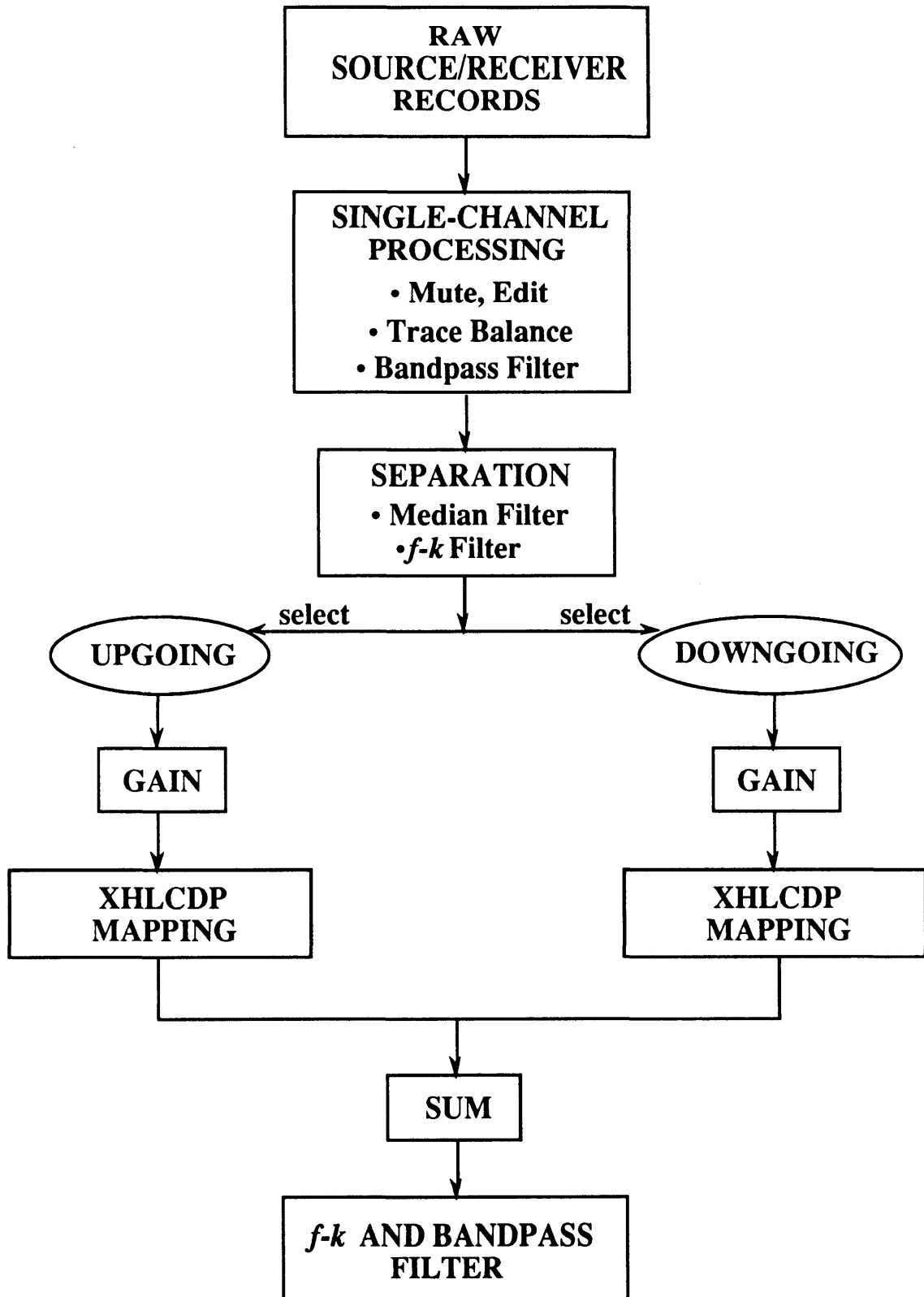


Figure 4.1: Processing flow of crosswell seismic data used in the thesis.

4.3 Median filtering

The first approach in processing the reflected arrivals in both synthetic and field crosswell data sets involves two different applications of the median filtering process. The first is to separate (after muting the first arrivals) the two reflected wavefields, upgoing and downgoing, of the synthetic data from each other. The second application is to remove the strong direct shear arrivals in the field data which follow both upgoing and downgoing directions (Figure 2.14) with respect to the receiver location. The median filter is used to achieve such goals by enhancing certain arrivals and then subtracting them from the total record to yield the desired arrivals.

Median filters operate by selecting the middle value of an ascending-ordered sequence of numbers. These numbers are taken from a moving window on the data to be processed. Hardage (1985) and Stewart (1985) offer extended reviews of the median filtering process and its applications in processing seismic data. The operation is used to reject noisy spikes as well as enhance discontinuities in the data. It has proved to be very useful in VSP processing and automatic editing of surface seismic data (Stewart, 1985). The running median filter can be applied along a given trace, or across adjacent traces. In general, a window of values will be used, a median extracted and placed on the output trace at the middle of the window. The process is repeated along the sequence until the entire sequence has been filtered.

Hardage (1985) gave considerable emphasis to the use of median filters in Vertical Seismic Profiling (VSP) data processing. He showed how they could be used to enhance events of interest. The method, removal of downgoing wave modes by subtraction, outlined by Hardage (1985) for VSP data is similarly followed here to separate the two wavefields in the synthetic data case. It is somewhat modified to serve the purpose of

removing the field-data direct arrivals from the later arriving reflections. The steps of applying the median filter to the individual crosswell gathers are described below;

- In an interactive mode, traveltimes are picked for the wave modes to be enhanced on the muted record of the synthetic data and for the direct shear arrivals on the band-pass record of the field data.
- The data are shifted by advancing each trace by its traveltimes pick. This would vertically align these wave modes to be enhanced. The data are placed at some reference time level.
- In this case, the median filter is applied across adjacent traces at each time sample. A median value is extracted from the specified window of traces at a specific time and assigned to the output trace at the midwindow position at that time. The window shifts over one trace and extracts the median sample again. The process is repeated until all traces at that time have been filtered. The process then moves to the next time sample and runs across the adjacent traces. This process is repeated for all times. The outcome of this process is called the filtered record which should contain the enhanced wave modes with the subsequent events that have the same slope.
- Both data sets of the input (total) and the filtered records are shifted back to the original time locations.
- The filtered record is then subtracted from the total record to yield what is called the difference record which should contain the desired arrivals on which further processing is needed while the filtered wave modes should be heavily attenuated.

Applying this procedure on shot 2 of the synthetic data (Figure 2.7) to separate both reflected wavefields from each other gives Figures 4.2 and 4.3, upgoing and downgoing respectively. In this median filtering process, the slope of the wavefield to enhance is picked and placed at some early part of the record. After aligning the events to enhance by the median filter, a 5-trace window is applied starting with the picked times until the end of the trace. Both reflected wavefields (Figures 4.2 and 4.3) are well separated with the exception of very minor residuals, particularly on the upgoing record (Figure 4.2). Also in the same figure, there is some damage to the wavelet of the first two events resulting from the mute of the direct arrivals on Figure 2.7. At this point, synthetic data are ready to be input to the transformation step of section 4.8 since deconvolution (only primary events are present), $f-k$ filtering, and gain are not required for these data.

For the second application of the median filtering process used here in this section, Figures 4.4 and 4.5 show the filtered and difference records resulting from median filtering receiver gather 2 of the field data set (Figure 2.14) with a 15-trace window starting with shear direct arrival times to the maximum trace length (9.6 ms). Effective direct arrival removal can be seen on the filtered record (Figure 4.4) and much stronger reflected events can now be traced with some other residual events on the difference record (Figure 4.5). Also, the median filter can create high frequency noise as can be observed particularly on the filtered record. A band-pass filter is usually used to remove these high frequencies introduced by the median filter.

The next step involves using 2-D ($f-k$) filters to separate the upgoing and downgoing reflections from each other to prepare them for further processing. Before considering this step, though, deconvolution of these data is attempted and discussed.

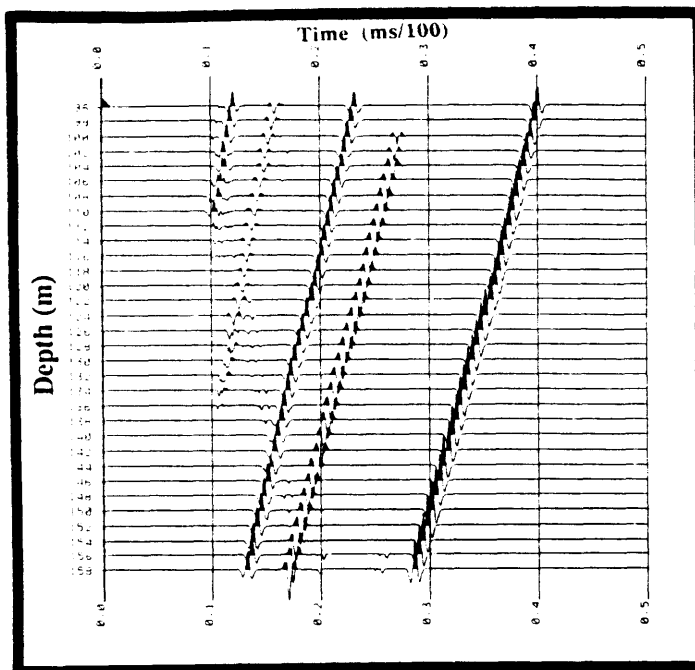


Figure 4.2: Median-filtered upgoing wavefield of synthetic shot record 2.

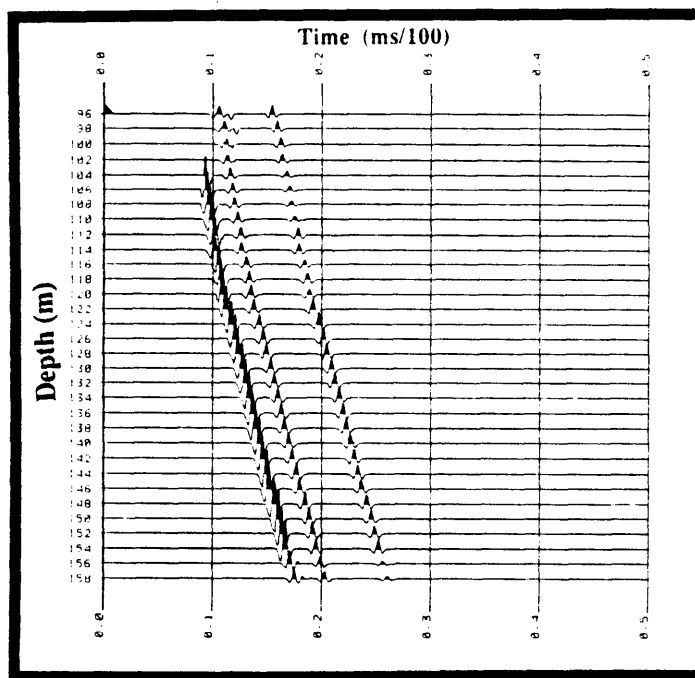


Figure 4.3: Median-filtered downgoing wavefield of synthetic shot record 2.

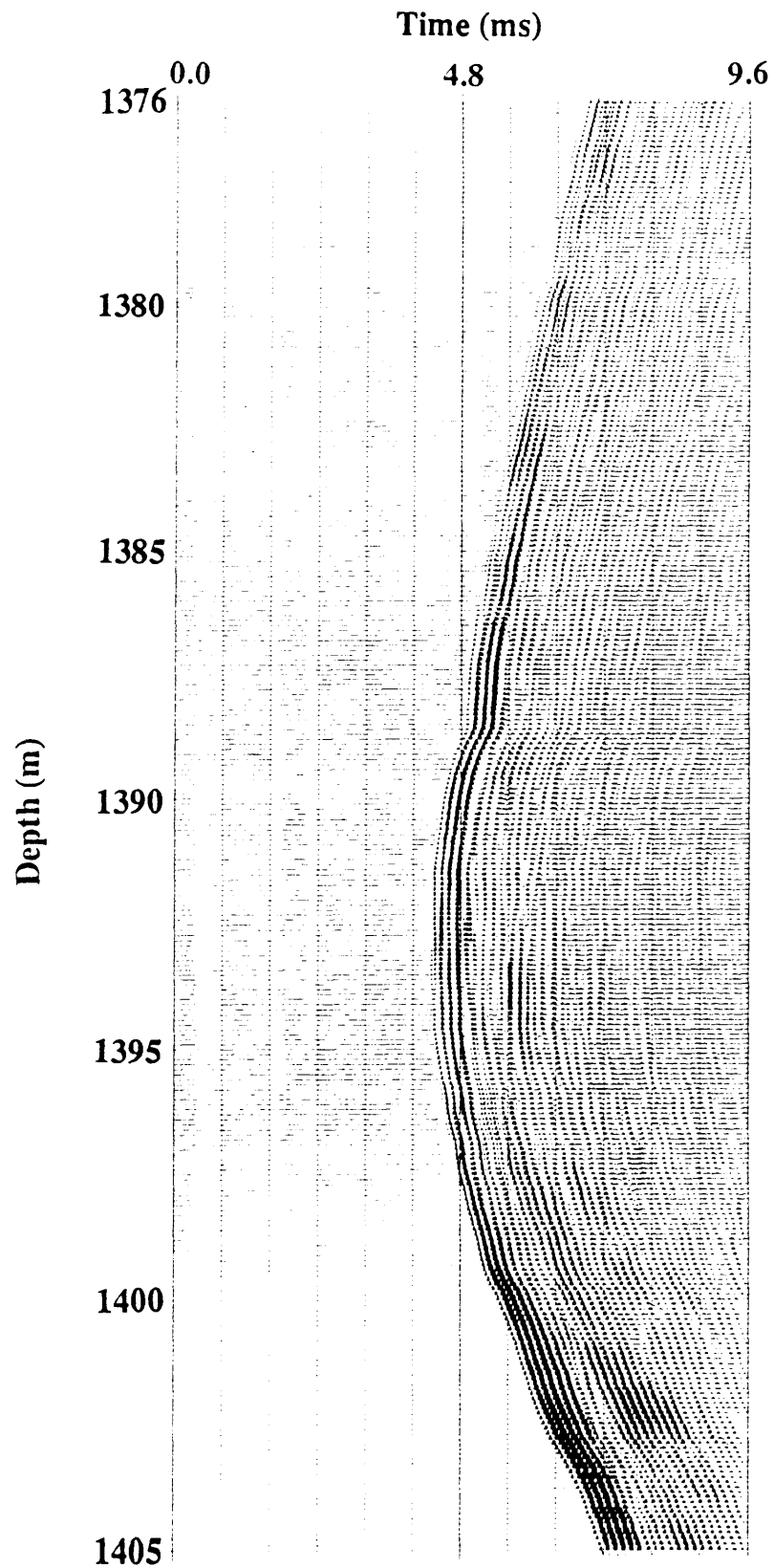


Figure 4.4: Median-filtered record of field-receiver gather 2. This figure represents the S-wave direct-arrival component of the record.

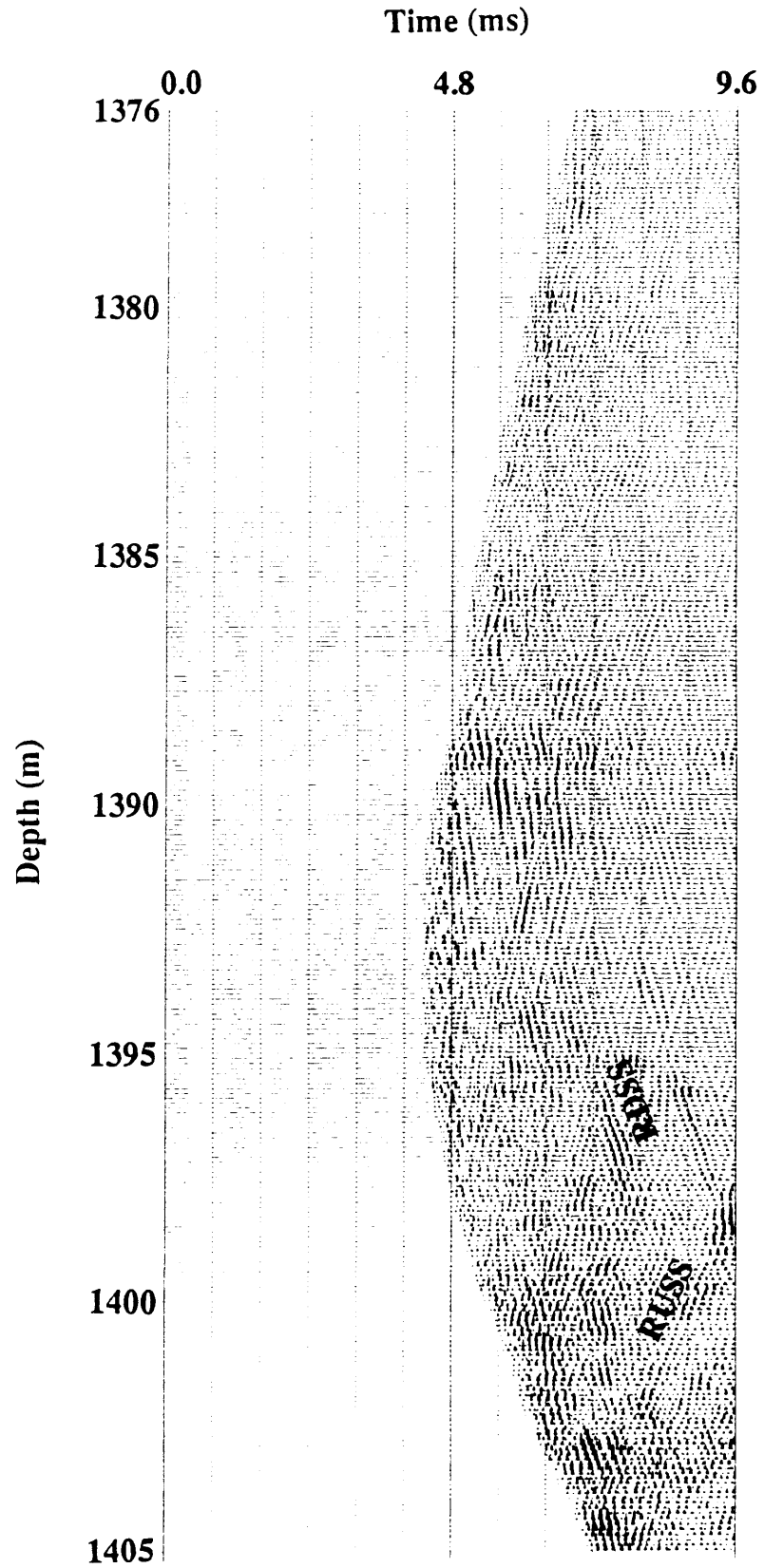


Figure 4.5: Difference record between the bandpass-filtered record (Figure 2.14) and the median-filtered record. This figure represents the reflection arrival component of the record.

4.4 Deconvolution

Deconvolution is a process used to improve the temporal resolution of seismic data by compressing the basic seismic wavelet. Deconvolution is also used to remove parts of the multiple energy from the seismic data under investigation. The process is based on the theory of the convolutional model of the recorded seismogram (Robinson, 1983). That is

$$\mathbf{x}(t) = \mathbf{w}(t) * \mathbf{e}(t) + \mathbf{n}(t), \quad 4.1$$

where $\mathbf{x}(t)$ is the recorded seismogram, $\mathbf{w}(t)$ is the basic seismic wavelet, $\mathbf{e}(t)$ is the earth's impulse response, $\mathbf{n}(t)$ is the random noise component, and $*$ denotes convolution. There are some assumptions that are necessary for obtaining a solution of the impulse response $\mathbf{e}(t)$ which represents the reflectivity function of the earth. One assumption is that the source waveform does not change as it travels in the subsurface. That is it is stationary. Also, the fact that there is no prior knowledge of the noise function $\mathbf{n}(t)$ leads to making the assumption that this noise component is zero. This would reduce the convolutional model to the form

$$\mathbf{x}(t) = \mathbf{w}(t) * \mathbf{e}(t). \quad 4.2$$

There are many types of deconvolution, including deterministic and statistical methods. If the source waveform is known (such as the recorded source signature), then the solution to the deconvolution problem can be obtained deterministically. If the source waveform were unknown, then the solution to the deconvolution problem will need to rely on some other information (e.g. statistical).

Optimum Wiener filtering can be employed in both deconvolution types. That is a least-squares inverse filtering process where the error between the actual output and the desired output is minimum (Robinson and Treitel, 1980; Yilmaz, 1987). In the

deterministic case where the wavelet is known, the filter operator is based on the autocorrelation of the wavelet and the crosscorrelation of the wavelet with the desired output. While in the statistical case where the wavelet is not known, the filter operator is based on the autocorrelation of the recorded seismogram and the crosscorrelation of the recorded seismogram and the desired output. In the latter case, the impulse response (reflectivity) is assumed to be random which indicates that the seismogram has the characteristics of the seismic wavelet in that their autocorrelation and amplitude spectra are similar (Yilmaz, 1987).

Attempts to deconvolve the crosswell records of the field data are carried out using the two previous types of deconvolution. The first is performed assuming that the seismic wavelet is known (deterministic). This is taken to be the separated direct-arrival record of the median filtering process (Figure 4.4), analogous to the conventional use of the downgoing wavefield as the seismic wavelet in VSP data processing. The filter operator is theoretically defined to be the inverse of the seismic wavelet. This operator, when convolved with the difference record (Figure 4.5) should compress the wavelet and yield the impulse response (reflectivity).

The second deconvolution (statistical) is applied on the total record (Figure 2.14) containing the full waveform starting at the shear wave direct arrival times. This is similar to conventional surface seismic deconvolution. A critical assumption here is that the wavelet is minimum phase in addition to the previously stated assumption that the reflectivity is a random process. For both types of experiments, zero-phase deconvolution is specified. Also in both cases, a separate operator is designed for every trace.

The result of the first case of deconvolution is shown for the deterministic algorithm in Figure 4.6. The comparison between the input record (Figure 4.5) and the deconvolved

record (Figure 4.6) suggests that the filtered record (Figure 4.4) used to compute the inverse filter does not represent any approximation of the seismic wavelet. Reflected data are very disturbed along the entire record and completely damaged in levels near the receiver location (1392 m). This may be attributed to factors affecting the direct arrivals in Figure 4.4 that do not correspond to the reflected arrivals in Figure 4.5. Medium effects and radiation patterns due to the different propagation directions of both direct and reflected waves are two possible factors that can be responsible for such discrepancy between the two waveforms. Another possible explanation for the distortion created by the deconvolution in Figure 4.6 is that the direct arrivals were not minimum phase wavelets and the program failed to compute proper filter operators that could compress the wavelets.

Now, consider the second case of deconvolving the total record (Figure 2.14) by operating a statistical algorithm. The quality of the output record, shown in Figure 4.7, is still distorted considerably. However, reflections are somewhat distinguishable. The previously stated factors (medium effects and radiation patterns) do not represent a problem in this case since the wavelet is assumed unknown and statistical computations based on the specified assumptions are carried out. It is the assumption of minimum phase wavelet again that can be affecting the results of the deconvolution in this case. Further processing steps would also consider the two deconvolution results shown here to compare them to the undeconvolved record (Figure 4.5). The latter record is the result of applying only median filtering to separate the reflected waveforms from the direct arrivals. Up to this point, it can be observed that this difference record contains better coherent reflections to focus on in further development of the processing flow.

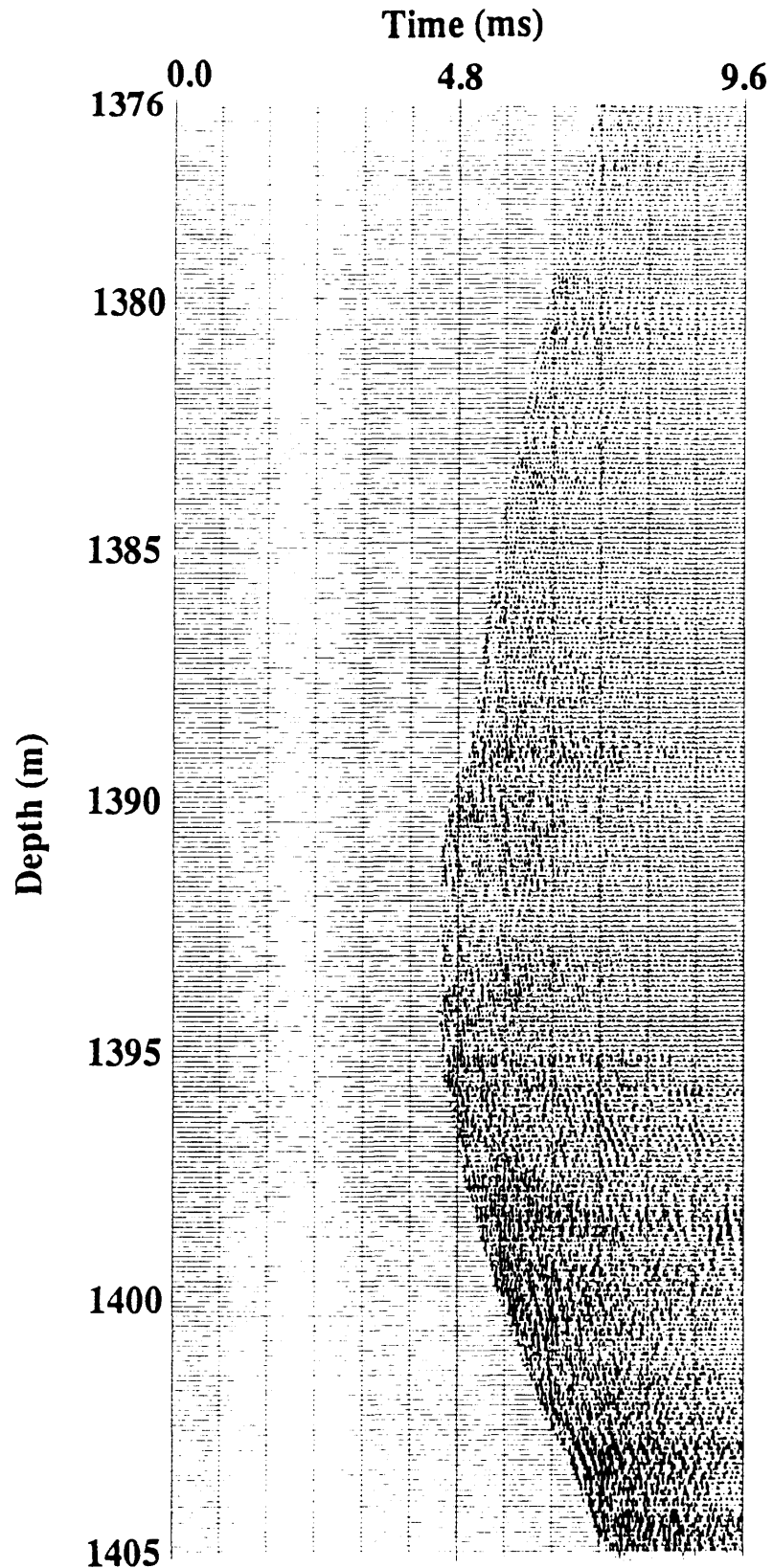


Figure 4.6: The result of applying deterministic deconvolution. The direct arrivals of the filtered record (Figure 4.4) are assumed to be the seismic wavelet.

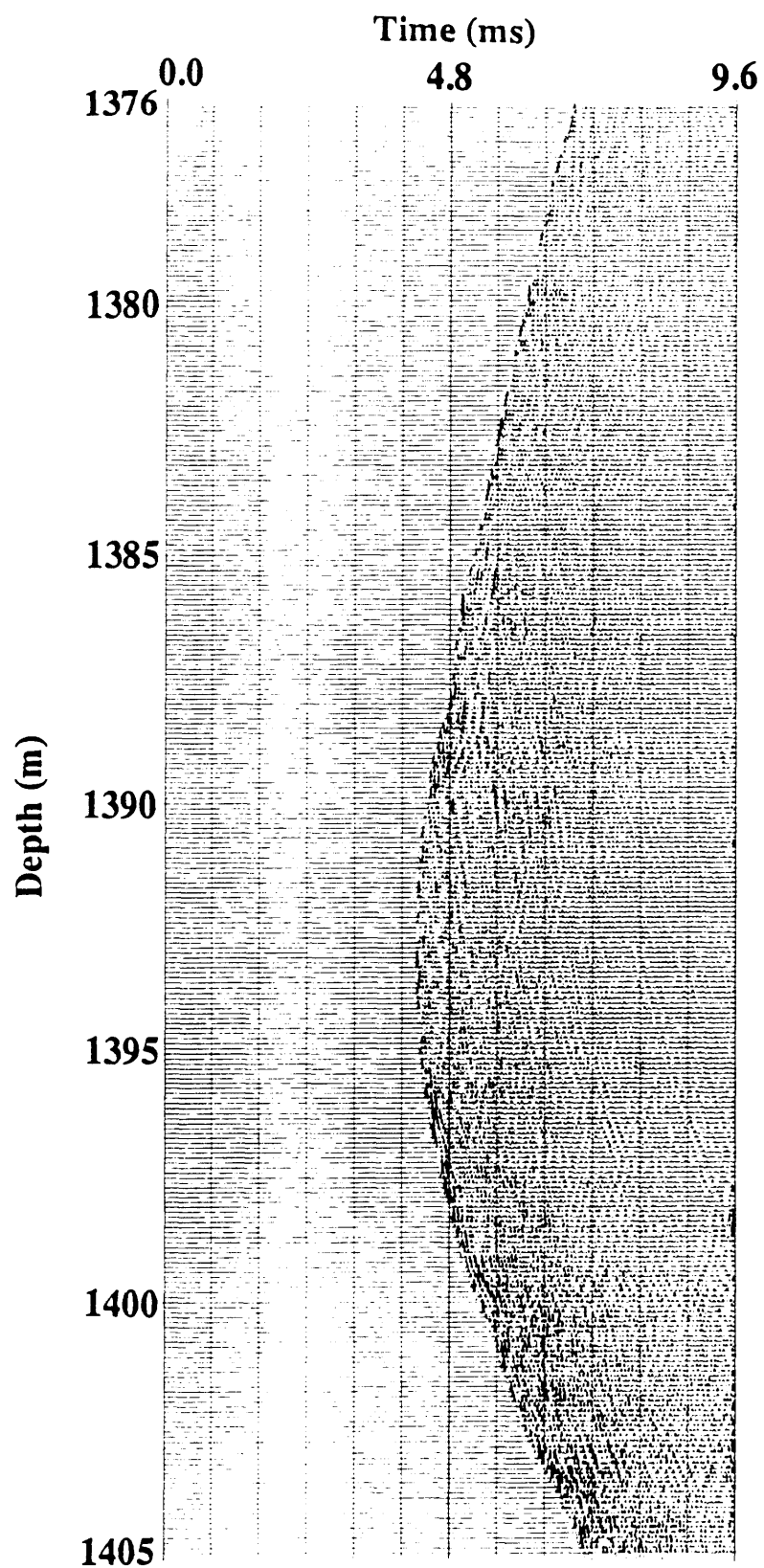


Figure 4.7: The result of applying statistical deconvolution. The total record (Figure 2.14) is deconvolved to remove the seismic wavelet.

4.5 $f-k$ filtering

Like median filters, the $f-k$ filter is a multichannel process that operates on several data traces simultaneously. It is useful in discriminating against noise and enhancing signal on the basis of a criterion that can be distinguished from trace to trace, dip in this case. Here, the $f-k$ filter is based on the concept that events with different dips that may interfere in the (t,z) domain can be isolated in the (f,k) domain. Thus, the operation requires the transformation of the data from the (t,z) into the (f,k) domain through the 2-D Fourier transform, two 1-D Fourier transforms.

The purpose of using the $f-k$ dip filter in this thesis is to separate the upgoing reflections from the downgoing ones since they have opposite dips. Here, the convention used (Western Geophysical software) to determine the dip of each wave type is that an event has a positive dip if the reflection time decreases as the depth increases while an event has a negative dip if the reflection time increases as the depth increases. So, applying this rule on both wave types, upgoing (RUSS) and downgoing (RDSS), in Figure 4.5 indicates that upgoing events have positive dips while downgoing events have negative dips. Positive dips in the (t,z) domain are associated with positive wavenumbers in the (f,k) domain. Negative dips in the (t,z) domain are associated with negative wavenumbers in the (f,k) domain.

Yilmaz (1987) discusses the practical issues associated with the spatial aliasing, the 2-D Fourier transform, and choice of pass/reject zones when performing $f-k$ dip filtering. Removal of selected wave modes by the $f-k$ filter in the case of VSP data is outlined by Hardage (1985). The process followed here would ultimately pass one wave type, say upgoing events (positive wavenumbers), while rejecting the other wave type, downgoing events (negative wavenumbers), completely from an input record that contains both of

them, say the produced median filtered record after attenuating the direct arrivals. The same process is repeated separately with reversing the action of the filter with respect to the wave types for the same input record. Figure 4.8 shows the steps involved in this process.

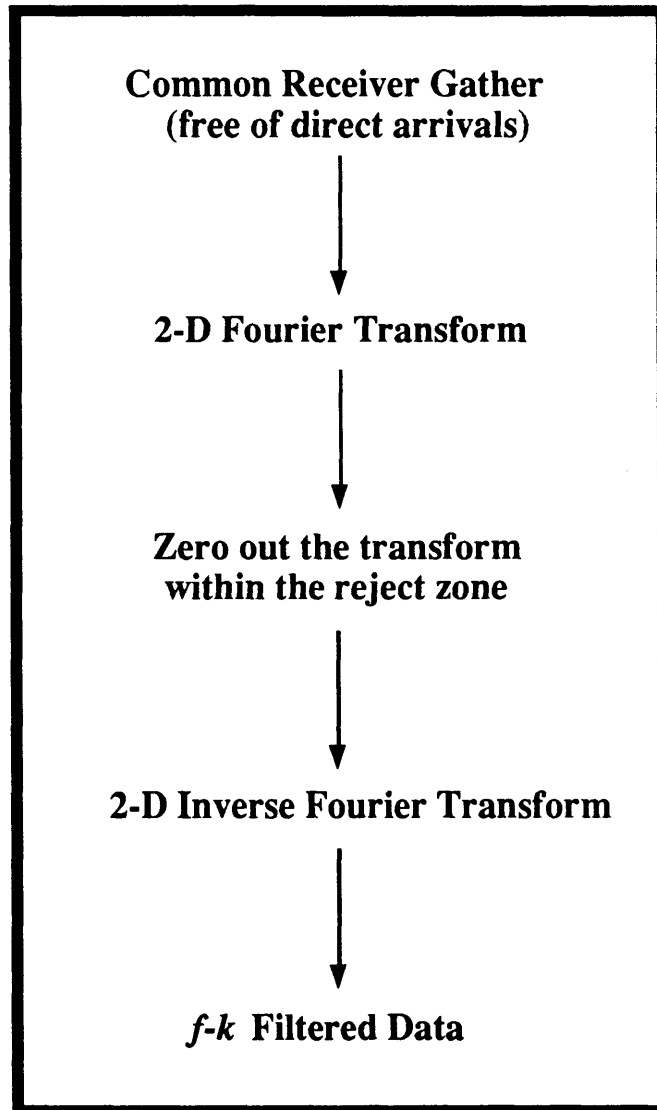


Figure 4.8: Processing steps of the f - k dip filter.

Taking the difference record (Figure 4.5) of median-filtered field data to be the input record, the separated wavefields resulting from following such a procedure independently for each wave type are shown in Figures 4.9 and 4.10 for upgoing and downgoing wavefields

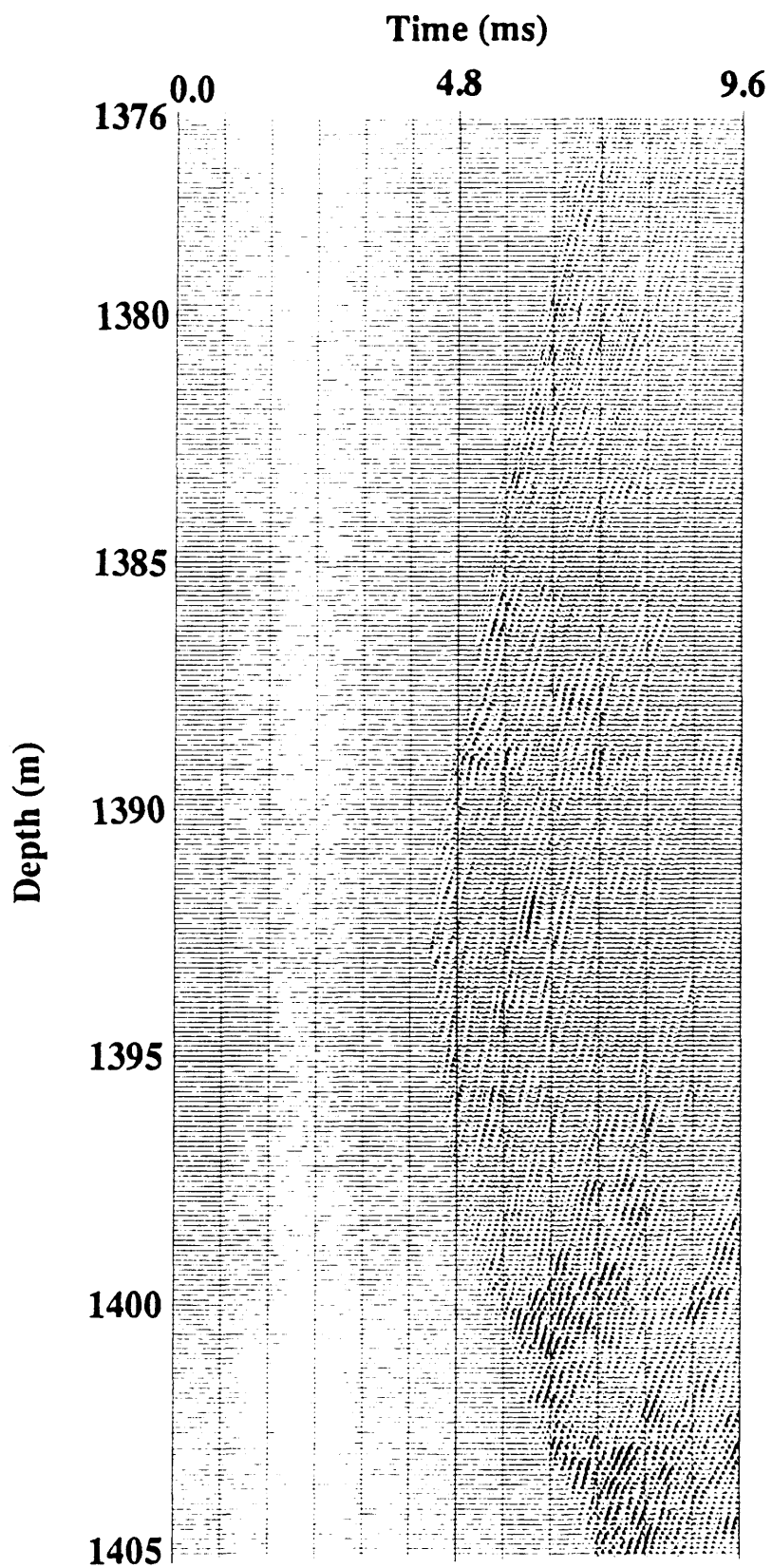


Figure 4.9: Upgoing reflected wavefield after f-k dip filtering of the difference record (Figure 4.5).

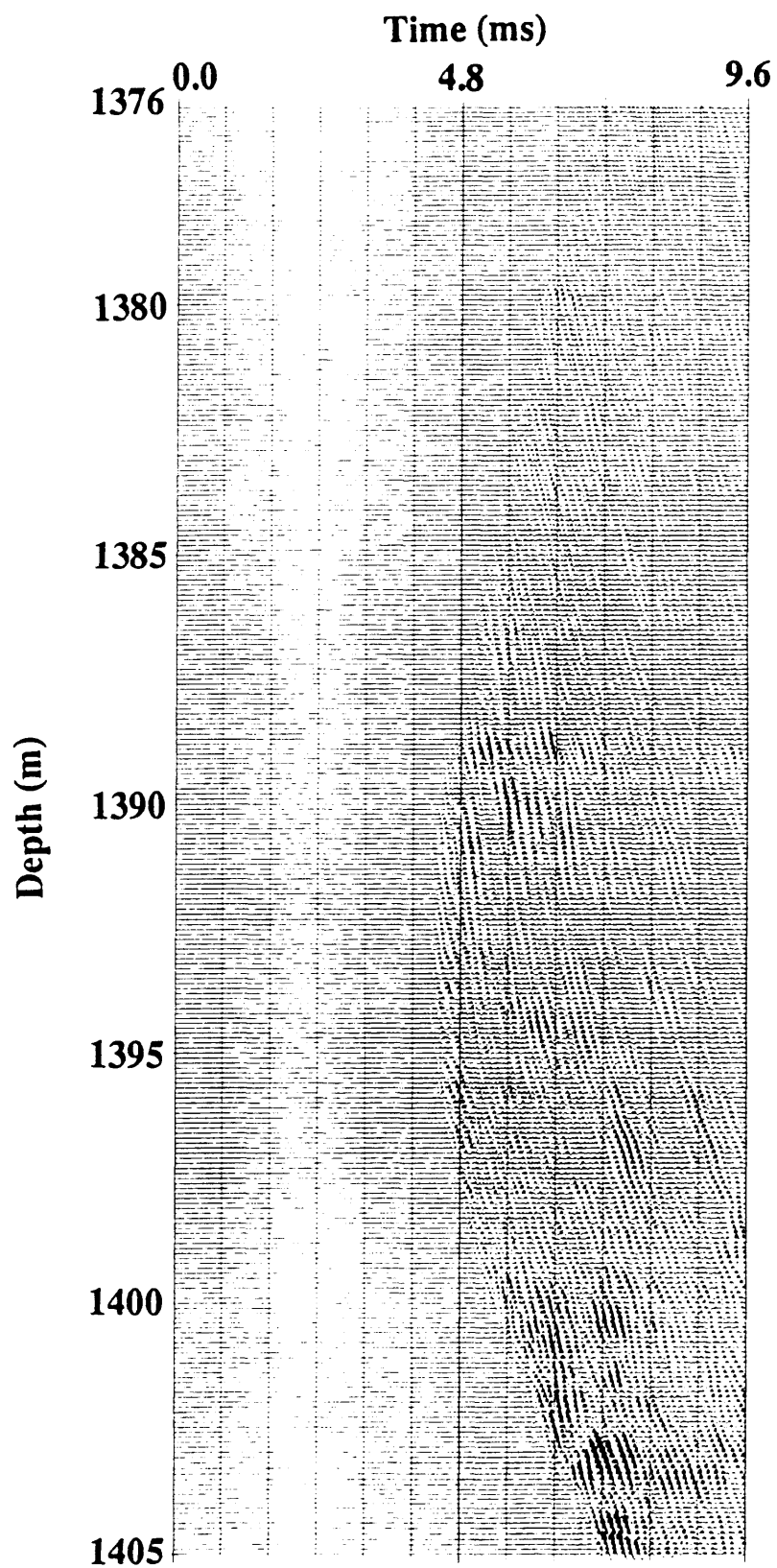


Figure 4.10: Downgoing reflected wavefield after f-k dip filtering of the difference record (Figure 4.5).

respectively. Numerous reflected events can now be seen on both records. As a reminder, these events represent symmetrical shear, S-S, reflections off the subsurface interfaces between the boreholes. The f - k filter has smeared some high-amplitude noise. These are residual events on the difference record (Figure 4.5) resulting from the median filtering operation. Further processing of these crosswell data such as mapping, which involves a binning step, and summing different receiver maps should help to cancel these events out since they would not be correctly flattened as the primary reflections. In general, the reflections are prominent and promise good results in further development. The next step is to gain these reflected data to account for amplitude losses.

4.6 Gain

Application of gain is shown here only for the crosswell field data set. The separated wavefields (Figures 4.9 and 4.10) need to be gained in terms of their amplitudes especially those of the reflections. This gives rise to time-variant gain, conventionally used in VSP and surface seismic data processing to compensate for amplitude decays resulting from geometrical spreading (Newman, 1973), transmission losses, and scattering (Hardage, 1985; Yilmaz, 1987). While reflections are increased in strength, noise components in the data are also boosted. This is one undesirable aspect of any type of gain application (Yilmaz, 1987). A trace-equalization process would be in order to balance the amplitudes of the record along the entire set of traces. This is particularly needed as the high amplitudes in Figures 4.9 and 4.10 would be even higher after the time-variant gain. Note that in section 2.5, a first step in recovering the amplitudes is presented in a trace equalization scheme to bring a group of traces to the same level before performing the median filtering process. Both time-variant gain and trace equalization are used here in this section for the purpose of preparing the reflected data for the mapping and summing processes discussed later.

Amplitude-recovered, gained and balanced, records of the deconvolution results (discussed in section 4.4) after separation are also shown here. This should provide a fair comparison between the deconvolved and the undeconvolved records that would potentially be selected and used in further processing of the crosswell data.

4.6.1 Time-variant gain

Signal amplitude decay is evident in the separated records of Figures 4.9 and 4.10. Note the weak appearance of reflections particularly in source levels farther away from the receiver location (1392 m). This does not mean that there are no strong reflections present in these parts of the data. Because of the amplitude decay, low-level signal is recorded.

The gain function applied here is modified from (Hardage, 1985) in which the raw amplitudes $A(t)$ in every trace are multiplied by a gain function $G(t)$. That is

$$A_{\text{gained}}(t) = A(t) G(t), \quad 4.3$$

where $G(t)$ has the form:

$$G(t) = \left(\frac{t}{c}\right)^x, \quad 4.4$$

where t is time in ms, x is chosen from several tests to be 1.52 and c is a constant for normalizing purposes. This constant, c , is selected to be 4.3 ms as the earliest time of the data to gain. The results of applying such a gain function on the data boosted up the residuals (noise component) left after the median filter as it boosted the primary reflections present.

4.6.2 Time-invariant balance

Trace balancing is applied to the group of traces in the record so that they all have the same desired rms amplitude level. This is to bring down the signal level in the traces

containing the high noise component while preserving the signal level in the traces containing the primary reflections. A trace balance scheme based on the peak amplitude criterion is performed here to obtain a separate scale factor for each trace. This is somewhat similar to the trace balance process undertaken in section 2.5. However, the present scheme scans the entire trace to pick the maximum absolute amplitude. The scale factor, S , is given by

$$S = \frac{1.414}{A} r, \quad 4.5$$

where A is that maximum absolute amplitude found on the entire input trace, and r is the desired rms amplitude for the output trace (consistently chosen as 2000).

The results of applying both the gain and balance steps on the separated upgoing and downgoing wavefields of Figures 4.9 and 4.10 are shown in Figures 4.11 and 4.12 respectively. Stronger and more continuous primary reflections can be seen along the entire record. In the same time, high-amplitude residuals of the median filter are heavily attenuated. The two points of interest stated above prove to be effectively achieved. Note that the results shown here (Figures 4.11 and 4.12) represent the median filtered record on which there is no deconvolution applied.

To further test the deconvolution records, similar processing steps (f - k filter and gain) are carried out for both the deterministic and statistical deconvolution records (Figures 4.6 and 4.7). This should provide a valid comparison between the undeconvolved and the two differently deconvolved records particularly since the reflections are now separated and enhanced. Figures 4.13 and 4.14 represent the upgoing and downgoing wavefields of the deterministically deconvolved record (Figure 4.6). The same type of wavefields appear in Figures 4.15 and 4.16 for the statistically deconvolved record (Figure 4.7).

By inspecting similar-type wavefields, upgoing (Figures 4.11, 4.13, and 4.15) or downgoing (Figures 4.12, 4.14, and 4.16) of the three cases, it is evident that both types of deconvolution introduce high frequency components to the data since they are attempting to spike the wavelet. However, there is a severe degradation of reflections in both deconvolved records. The undeconvolved record has relatively more continuous and pronounced events than the other two records. Within the two deconvolved records, the statistical record appear to have relatively better preservation of reflections than that of the deterministic one. However, these reflections lack the continuity that is desirable from a process like deconvolution. It is the quality of the undeconvolved records that led to the decision of selecting these records and proceeding with them in further processing steps.

4.7 Crosswell subsurface coverage

Before proceeding with reflection processing of the separated wavefields, subsurface coverage of the crosswell experiment is investigated. The objective here is to develop a mathematical expression for the location of reflection points in a crosswell geometry. This can provide an insight as to how a reflected image should look and which areas may have useful reflection information. The following derivation is based on a constant velocity model for a single source/receiver array.

Consider the geometry shown in Figure 4.17. A source **S** located at depth s in a borehole and a receiver **H** is placed in another borehole at depth h . X is the distance between the source and the receiver boreholes. Point **H'** is the image point for receiver **H** with respect to a reflector **R**, with depth r from the surface (or any reference level). Point **S'** is at the same depth level as point **S** (the source). The problem is stated as follows;

Knowing the travelttime from the source to a receiver, the depths of the source and that receiver and the distance between the boreholes, can we map crosswell traveltimes

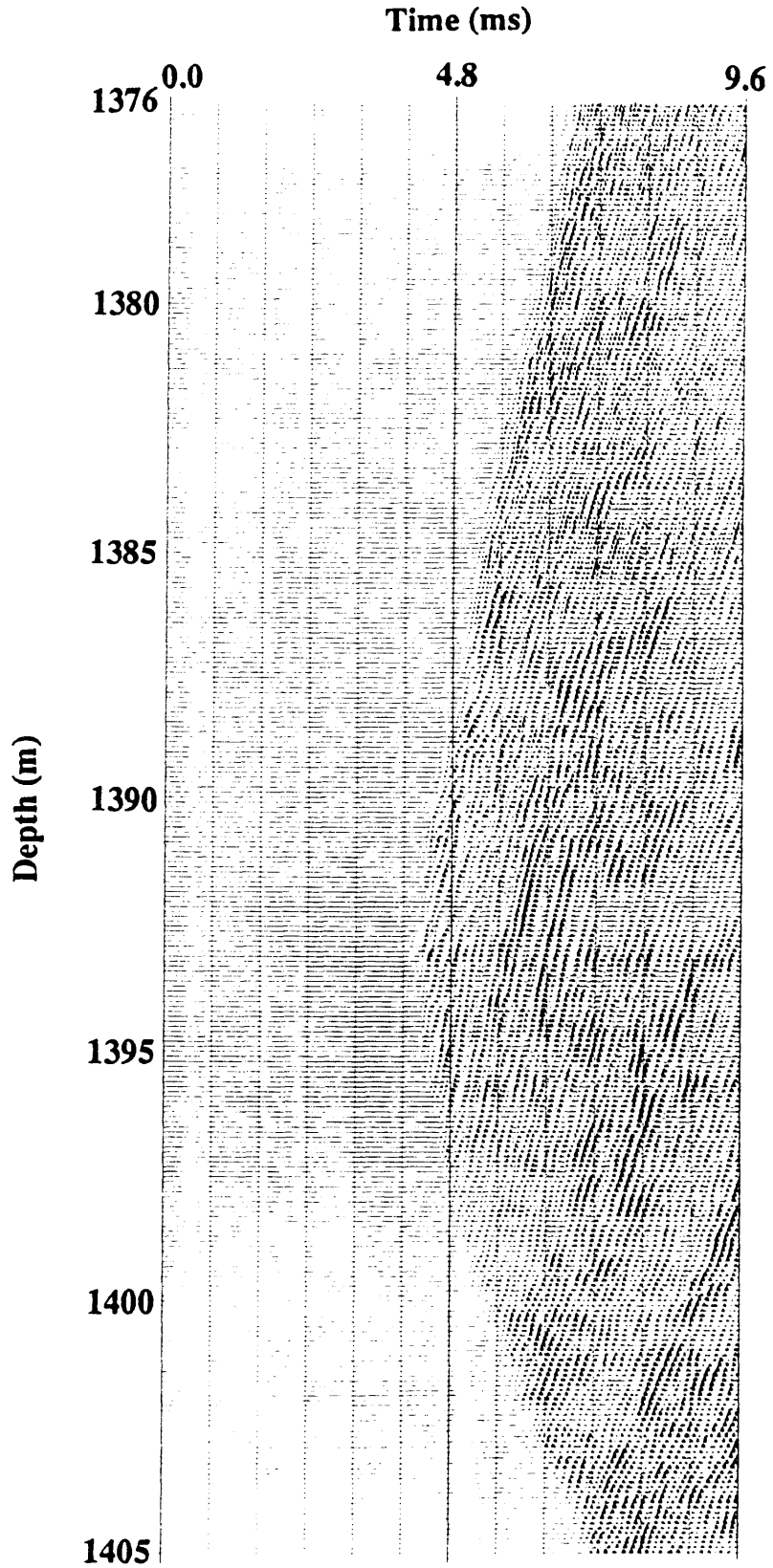


Figure 4.11: Gained upgoing reflected wavefield. No deconvolution is used.

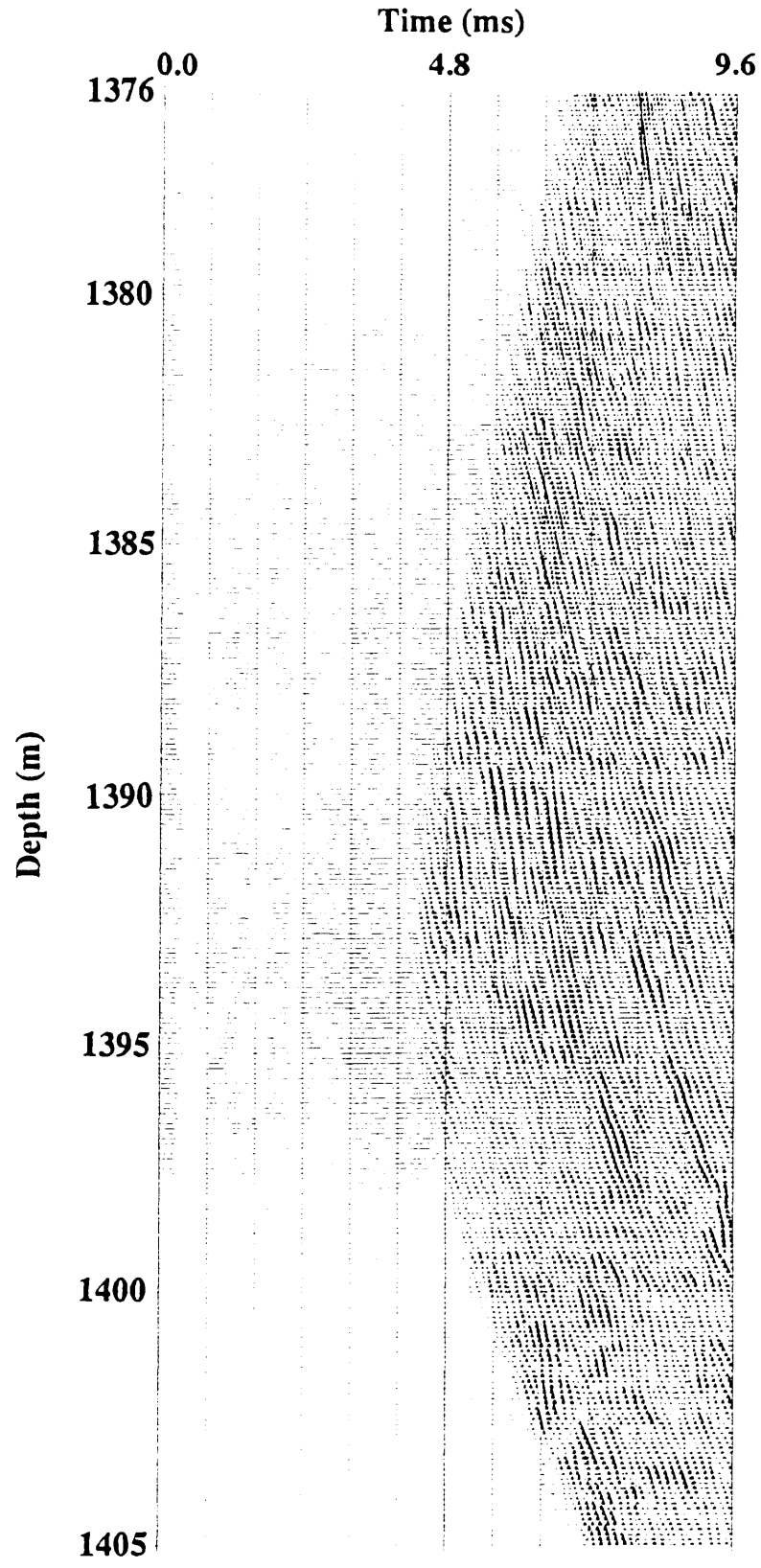


Figure 4.12: Gained downgoing reflected wavefield. No deconvolution is used.

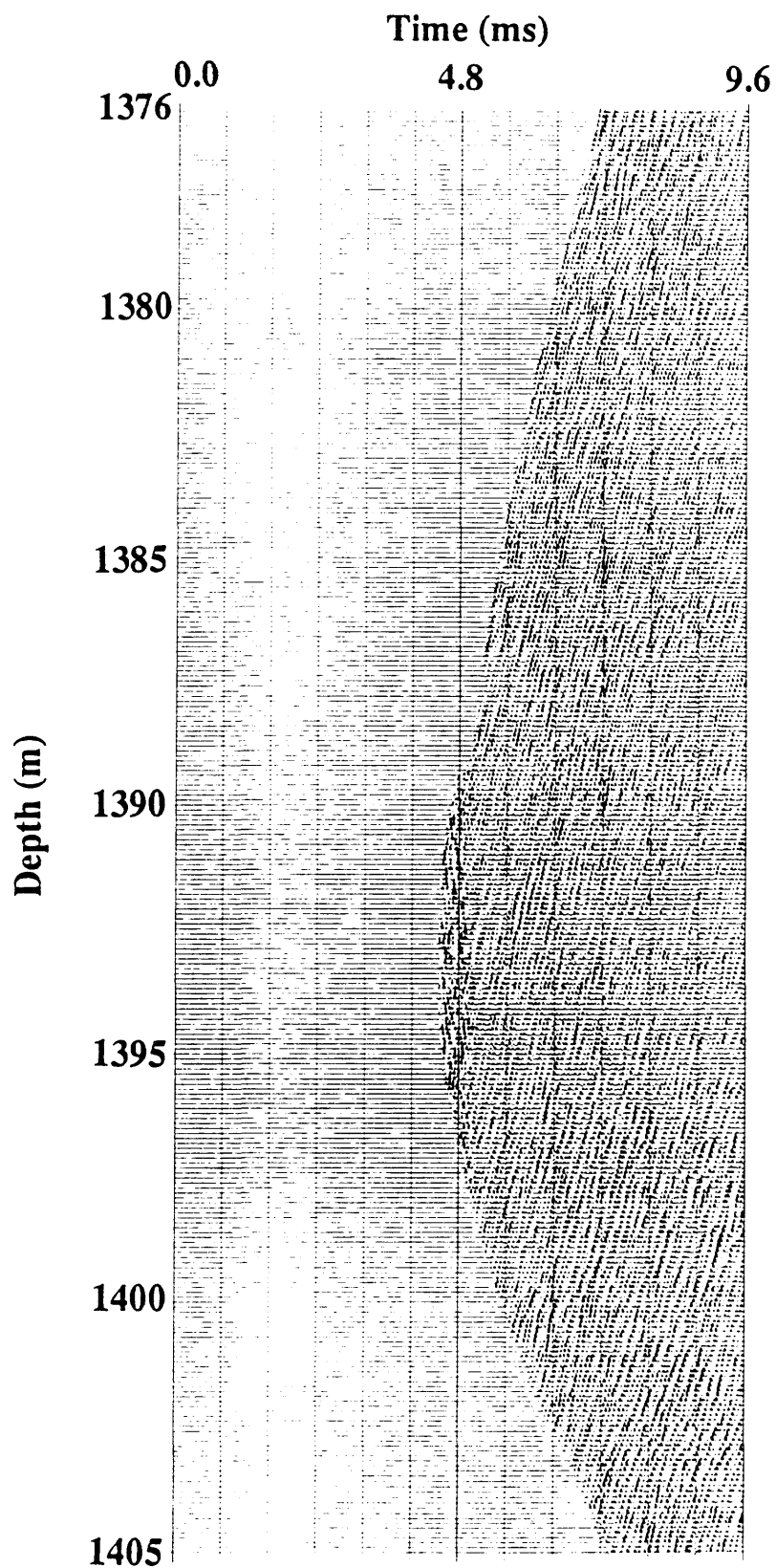


Figure 4.13: Gained upgoing reflected wavefield. Deterministic deconvolution is used.

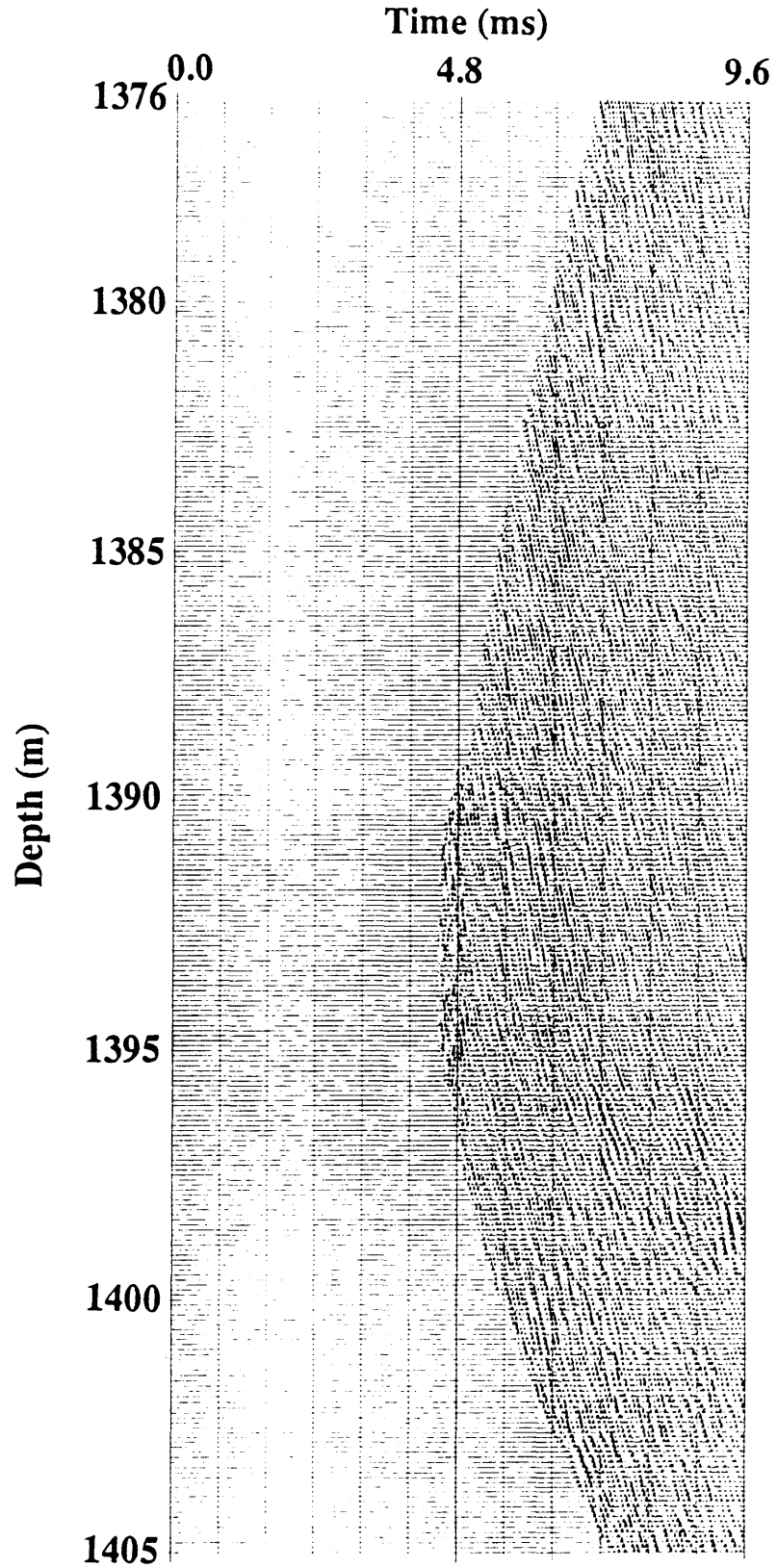


Figure 4.14: Gained downgoing reflected wavefield. Deterministic deconvolution is used.

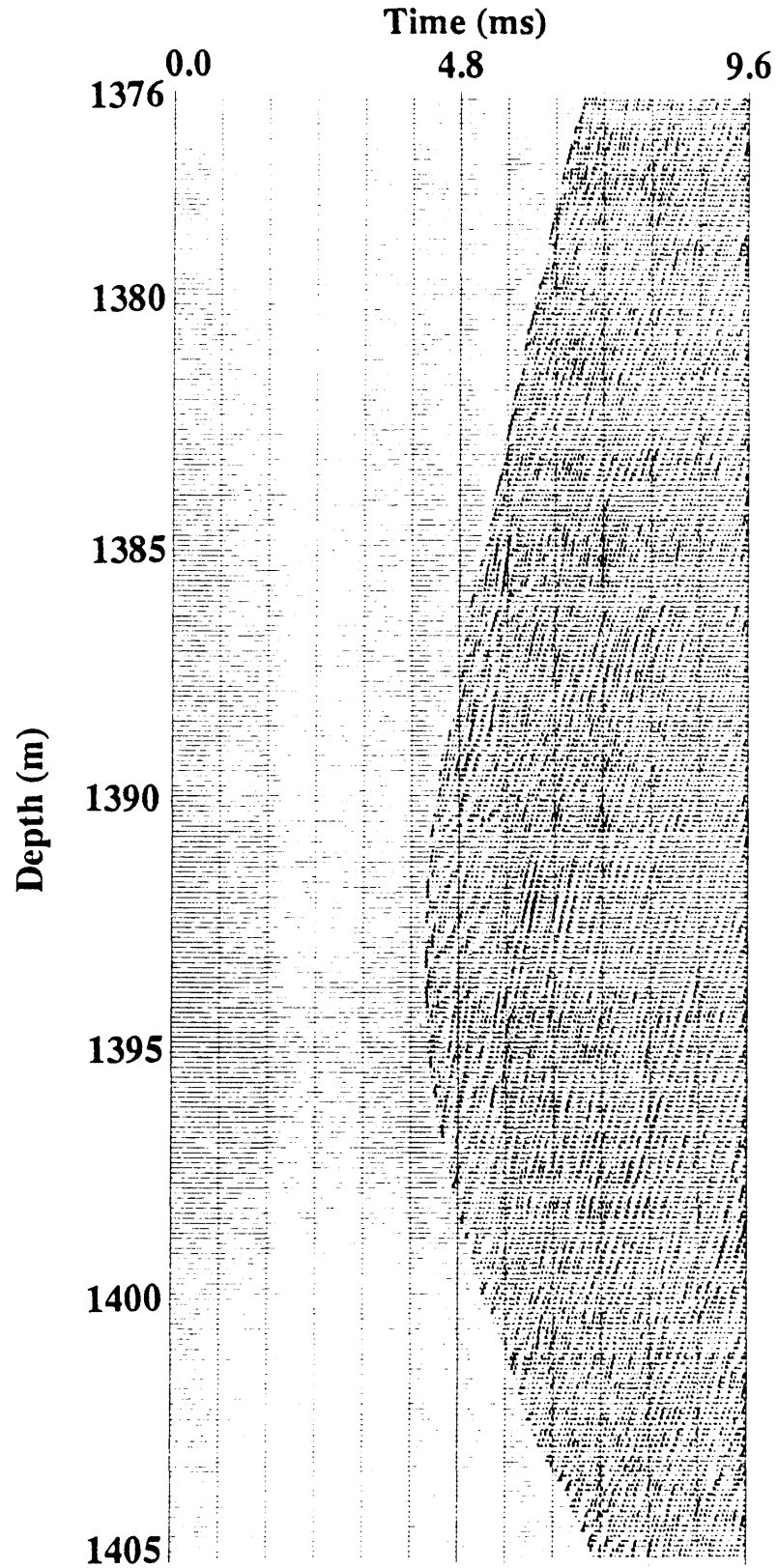


Figure 4.15: Gained upgoing reflected wavefield. Statistical deconvolution is used.

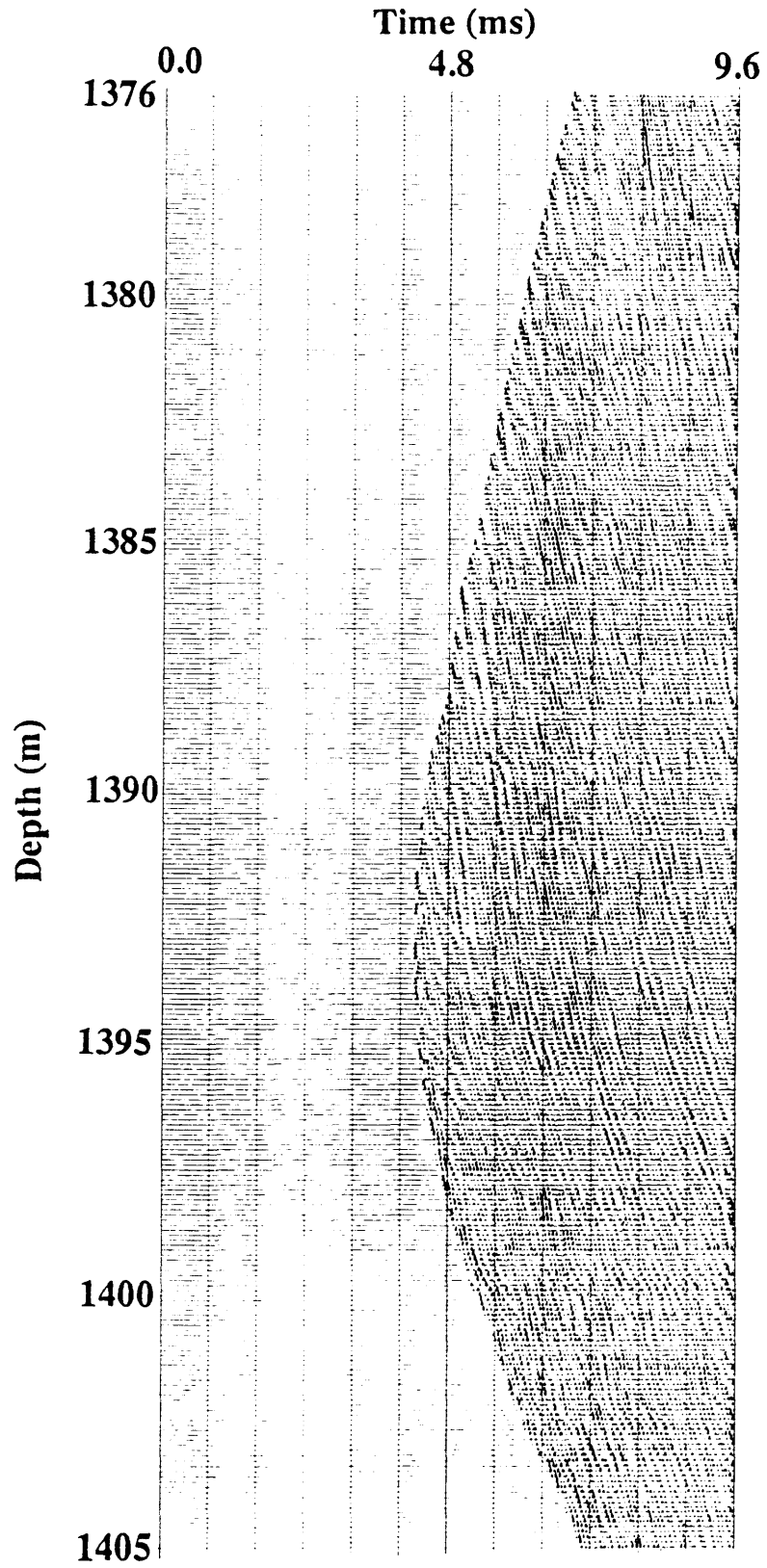


Figure 4.16: Gained downgoing reflected wavefield. Statistical deconvolution is used.

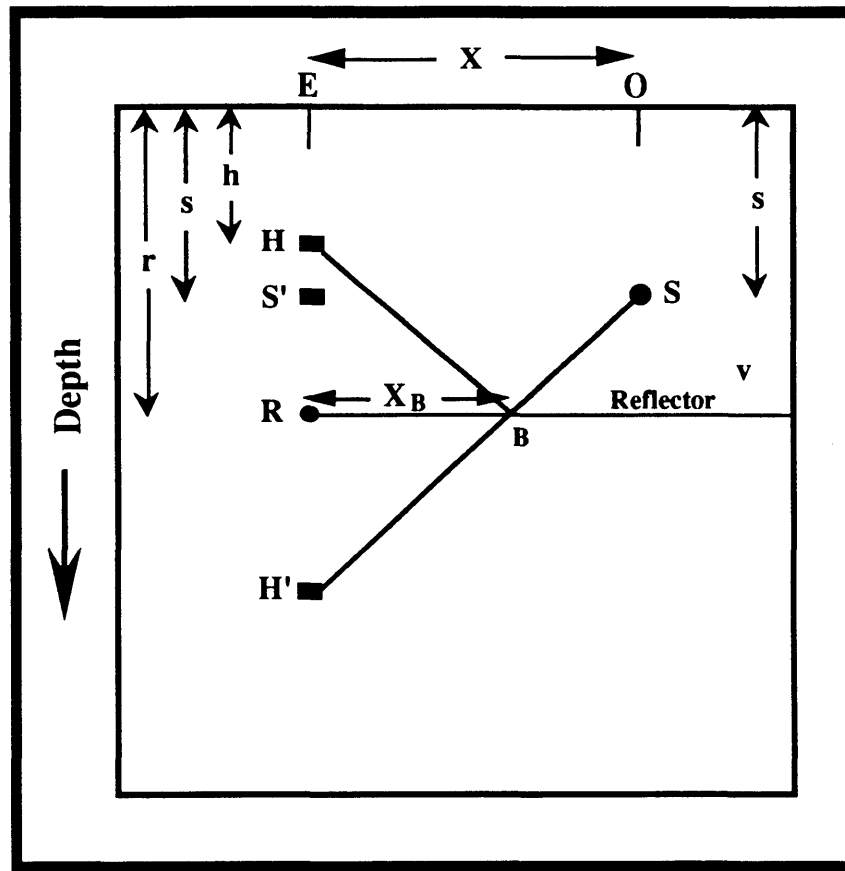


Figure 4.17: A constant-velocity case to derive the 2-way normal-incidence time and subsurface reflection point.

into two-way vertical time and reconstruct the sample points into the surface locations vertically above their reflection points ?

The following derivation hopes to answer this question for the geometry considered in Figure 4.17. The method follows Stewart's (1988) scheme for VSPCDP map of P waves. For source S and receiver H,

The total length of the ray is

$$\overline{SBH} = [(2r-h-s)^2 + X^2]^{\frac{1}{2}}.$$

4.6

⇒ The traveltime of the wave along the ray is

$$t = \frac{[(2r-h-s)^2 + X^2]^{\frac{1}{2}}}{v} \quad 4.7$$

By squaring both sides of equation 4.7 and solving for r , one obtains:

$$r = \frac{1}{2} \left[\left(t^2 v^2 - X^2 \right)^{\frac{1}{2}} + h + s \right] \quad 4.8$$

The two-way vertical time t_v ,

$$t_v = 2 \frac{r}{v} \quad 4.9$$

$$t_v = \left\langle t^2 - \frac{X^2}{v^2} \right\rangle^{\frac{1}{2}} + \frac{h+s}{v} \quad 4.10$$

Now, to find where the reflection point B is with respect to the receiver borehole we use similar triangles BRH' and $SS'H'$, from which:

$$\frac{BR}{X} = \frac{RH'}{S'H'} \quad \langle BR = X_B \rangle \quad 4.11$$

then,

$$X_B = X \left[\frac{r-h}{2r-h-s} \right] \quad 4.12$$

After some algebra,

$$X_B = \frac{X}{2} \left[1 + \frac{s-h}{\left(t^2 v^2 - X^2 \right)^{\frac{1}{2}}} \right] \quad 4.13$$

or $\left\langle \text{by } r = \frac{v t_v}{2} \right\rangle$

$$\mathbf{X}_B = \frac{\mathbf{X}}{2} \left[\frac{\mathbf{v} t_v - 2 \mathbf{h}}{\mathbf{v} t_v - \mathbf{h} - \mathbf{s}} \right]. \quad 4.14$$

These formulae are applicable for all receivers and sources located above the interface where reflections may occur. If the receiver is at the same depth as the source ($\mathbf{s}=\mathbf{h}$), then the formulae become

$$t_v = \left\langle t^2 - \frac{\mathbf{X}^2}{v^2} \right\rangle^{\frac{1}{2}} + \frac{2 \mathbf{h}}{v}, \quad 4.15$$

and

$$\mathbf{X}_B = \frac{\mathbf{X}}{2}. \quad 4.16$$

As we can see, these formulae are only adequate for a constant-velocity medium. Nevertheless, the only two previous studies that considered crosswell mapping (Baker and Harris, 1984; Iverson, 1988) used a constant-velocity model. This would be adequate only if the velocity contrasts are not very high. In the presence of low-velocity producing zones and if the assumed velocity was higher than the true velocity, the mapped events are going to be shifted up in their 2-way normal time (and consequently in their depth), and also the reflection point locations are not going to be correctly computed.

Based on the formulae derived above, Figure 4.18 demonstrates the subsurface zones covered for shot 2 (at depth 124 m) of the synthetic crosswell data set used in this study. For the field data case, the subsurface coverage of receiver gather number 2 is also approximated and shown in Figure 4.19. In both figures, a significant feature of the crosswell geometry is the extended coverage from the midpoint toward the source borehole (in the synthetic data case) and the receiver borehole (in the field data case) for both upgoing and downgoing wavefields. This represents an advantage compared to the VSP

geometry whose coverage only extends up to the midpoint between the source and receiver boreholes.

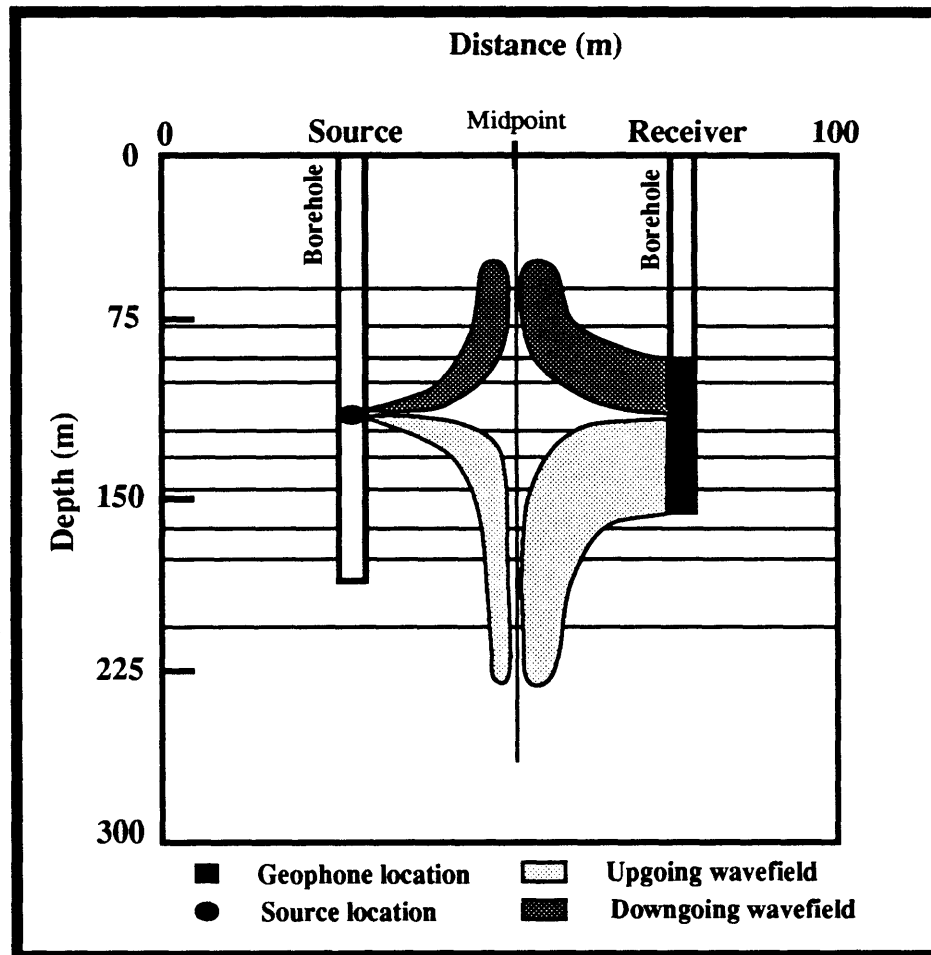


Figure 4.18: Subsurface coverage of shot record 2 of the synthetic data.

4.8 Crosswell transformation

As in VSP data, raw crosswell data in the domain of recording time and depth are difficult to interpret in terms of lateral subsurface geology. This study considers a process conventionally known in VSP data processing as VSPCDP mapping (Wyatt and Wyatt, 1984; Dillon and Thomson, 1984). Since the downgoing events in VSP are either direct arrivals or multiple energy from the subsurface reflectors, the method only transforms the upgoing wavefield from the domain of recording time and depth into the domain of lateral

surface distance and two-way normal time. This presents the VSP data as a classic surface seismic section and enables one to improve horizon interpretation in the zone near the borehole (Poel and Cassell, 1989; Stewart, 1989; Geis et al., 1990). The information required to perform this process is the geophone location, the source location, and a velocity profile. The method can be thought as a trace-by-trace moveout correction (single channel process) followed by stacking the traces that lie within a specific bin width. Hence, the mapping procedure is not a migration since it can handle neither diffractions nor complex structures (Dillon and Thomson, 1984).

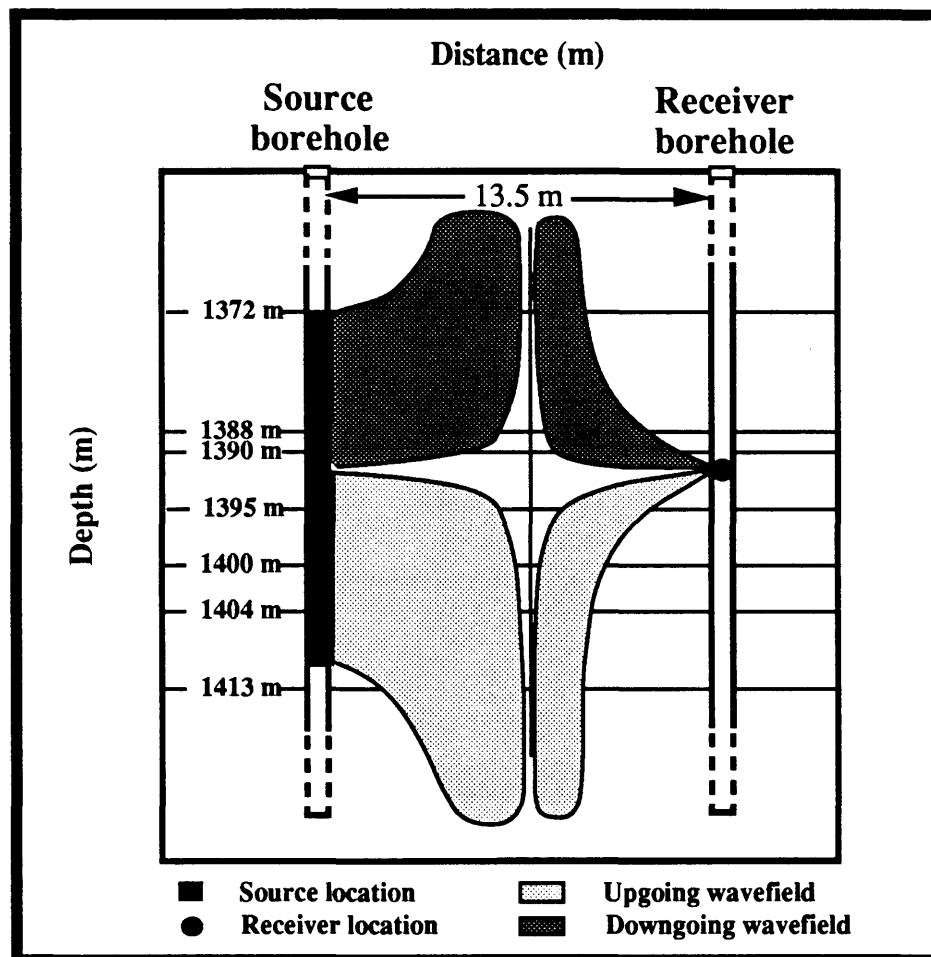


Figure 4.19: Subsurface coverage of receiver gather 2 of the field data.

The interest of this study in the previous transformation technique is to apply similar reconstruction procedure to crosswell reflected data and use its benefits in delineating the medium between the boreholes. Note that the only experimental difference between VSP and crosswell data is the source depth. In VSP, the source is at or near the surface (always above the receiver level). In crosswell, however, the source is at greater depths and can be above or below the receiver level. For this reason, and by inspecting Figures 4.18 and 4.19, the crosswell geometry has a subsurface coverage that is similar, but more extended than that of the VSP geometry.

The current study demonstrates crosswell mapping based on a multi-layered model with its proper transformation attributes (Abdalla et al., 1990). This may represent an advantage over the two previous studies (Baker and Harris, 1984; Iverson, 1988) that considered a constant-velocity model in their transformation process. Here, the mapping procedure is called the XHLCDP transformation to indicate that upgoing and downgoing primary reflections are used. Based on Western Geophysical software, the reconstruction is performed separately on both the upgoing and the downgoing reflected wavefields based on the shear velocity profile obtained from the travelt ime inversion procedure presented here in Chapter 3. Since the crosswell experiment is only acquired for subsurface areas around the zone of interest (1380 m - 1420 m), the results of the reconstruction process are plotted in depth so that direct comparison between crosswell and log information can be undertaken.

As in most of the previous processing steps, synthetic data examples with their known solutions are shown first to support the validity of the processing step. Figures 4.20 and 4.21 show the mapping results for both upgoing and downgoing wavefields of shot record 2 (Figures 4.2 and 4.3) respectively. It can be observed that the mapping has placed the reflectors correctly in their subsurface locations (see the model in Figure 2.5).

There is however one reflector that seems to be distorted in the upgoing image (Figure 4.20) that is the uppermost reflector (of positive amplitude). This is apparent in the upgoing wavefield input of this map (Figure 4.2) as the first event is very limited and also somewhat distorted due to the mute of the direct arrivals (discussed earlier in section 4.3). The mapping of more records is expected to cover more subsurface reflections that can all be summed in one final image for both upgoing and downgoing wavefields.

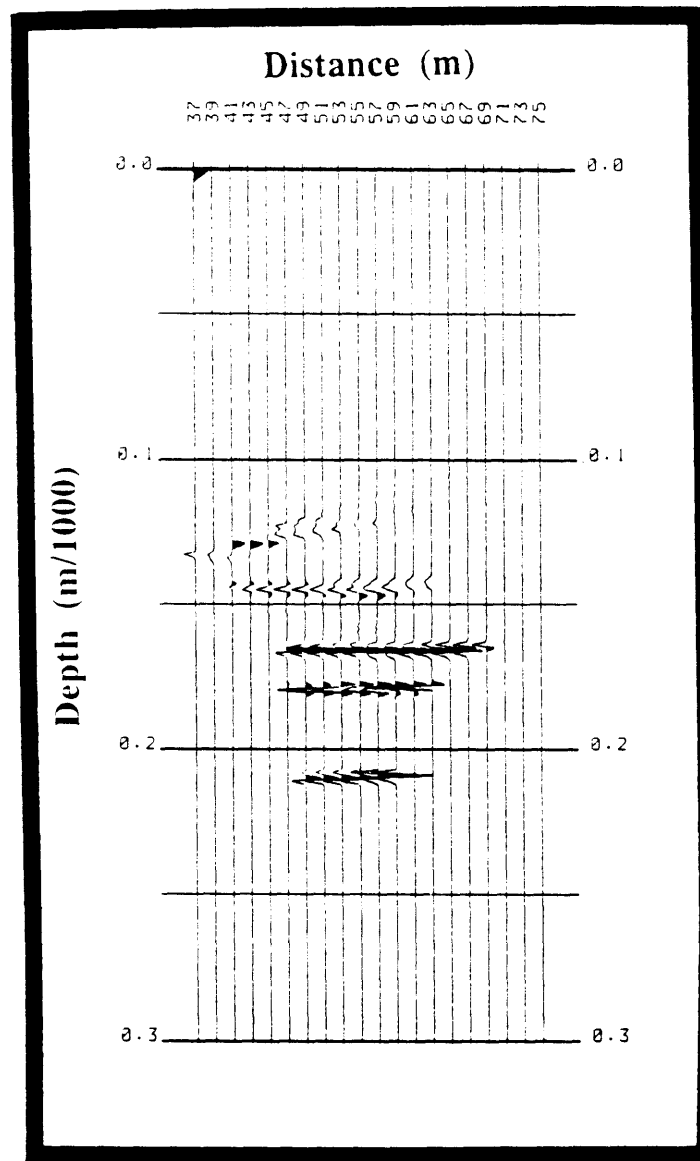


Figure 4.20: Upgoing map of XHLCDP transformation for shot 2 of the synthetic data.

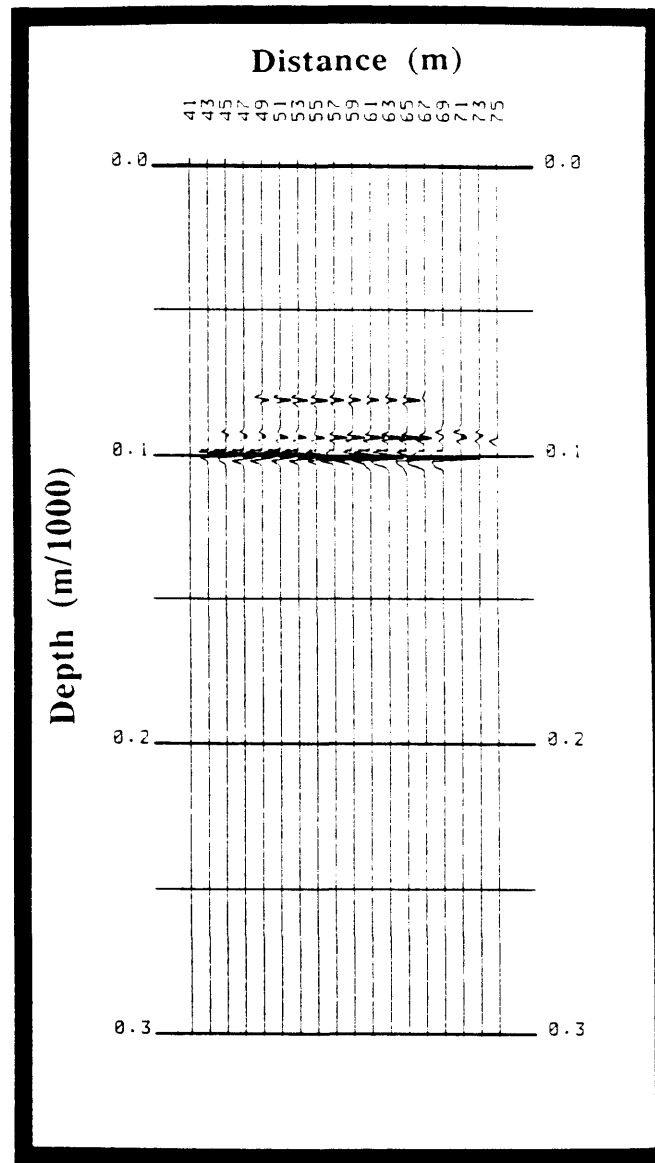


Figure 4.21: Downgoing map of XHLCDP transformation for shot 2 of the synthetic data.

Similar mapping is carried out for the field f - k separated records of receiver gather 2 (Figures 4.11 and 4.12). The upgoing map is shown in Figure 4.22 for depth interval 1390 m - 1410 m while the downgoing map is shown in Figure 4.23 for the depth interval 1370 m - 1390 m. The horizontal coordinate represents the distance from the receiver borehole (maximum of 13.5 m). When these two maps are put together, Figure 4.24 results for the entire interval, 1370 m - 1410 m. Several observations have to be discussed here.

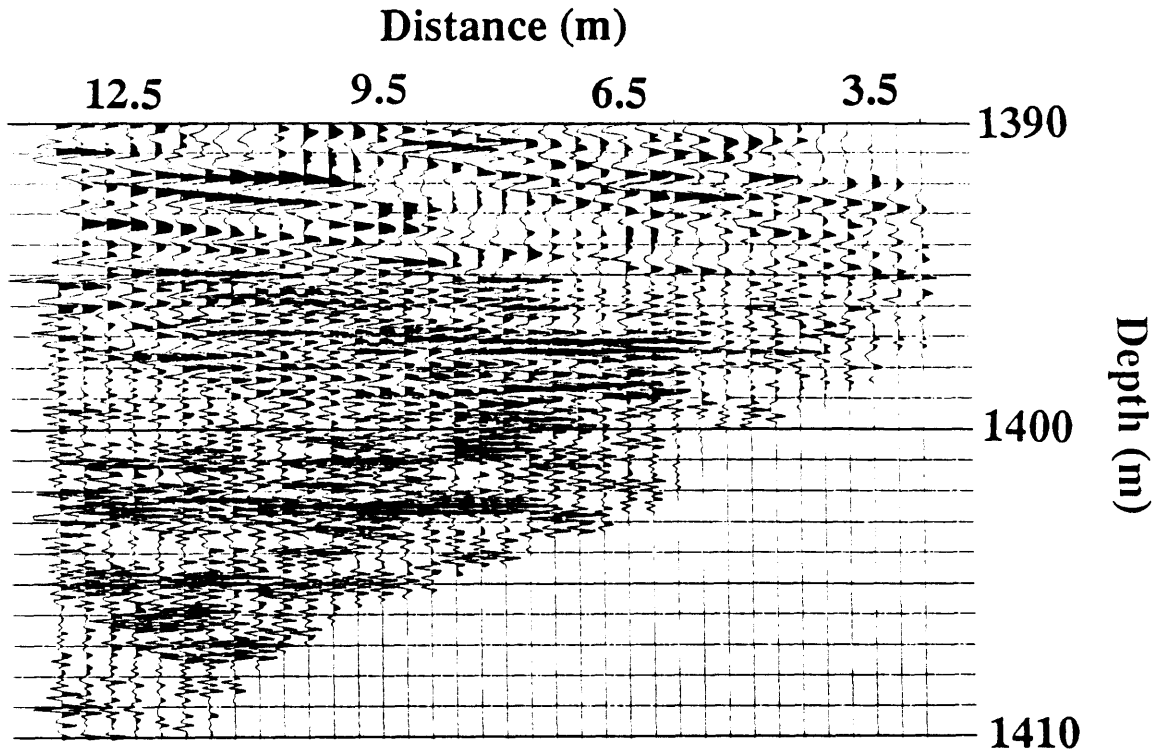


Figure 4.22: Upgoing map of XHLCDP transformation for receiver 2 of the field data.

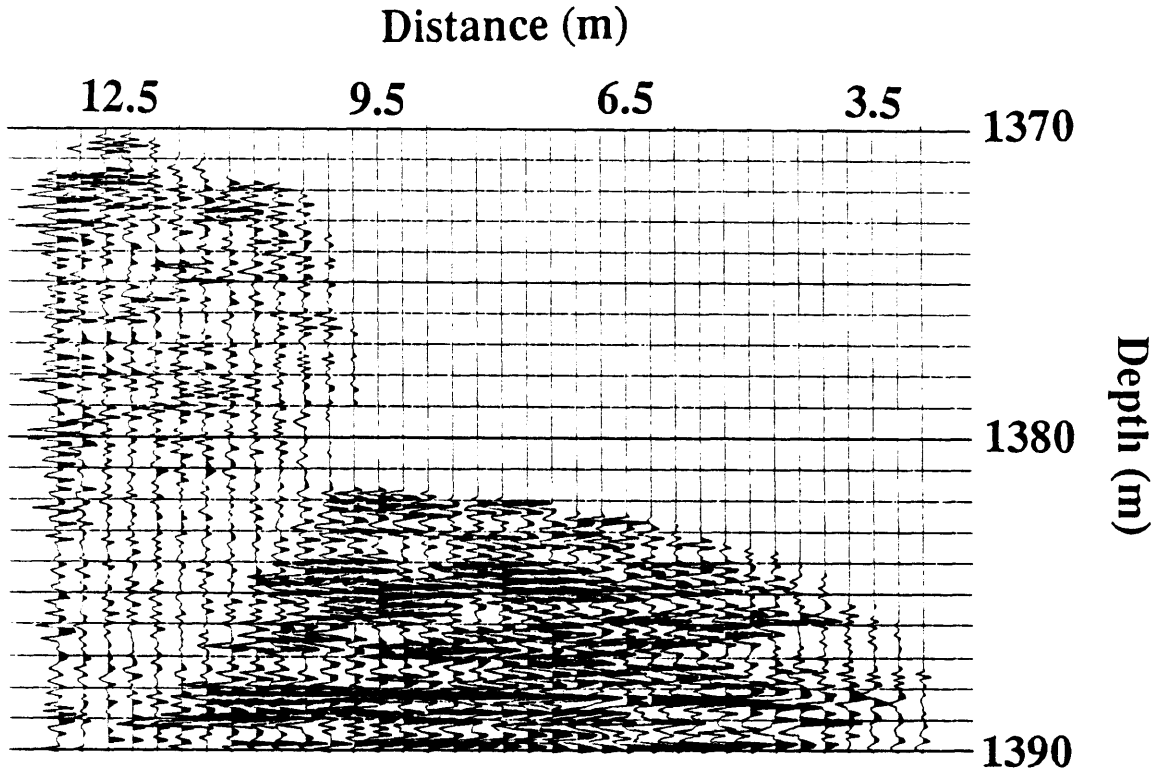


Figure 4.23: Downgoing map of XHLCDP transformation for receiver 2 of the field data.

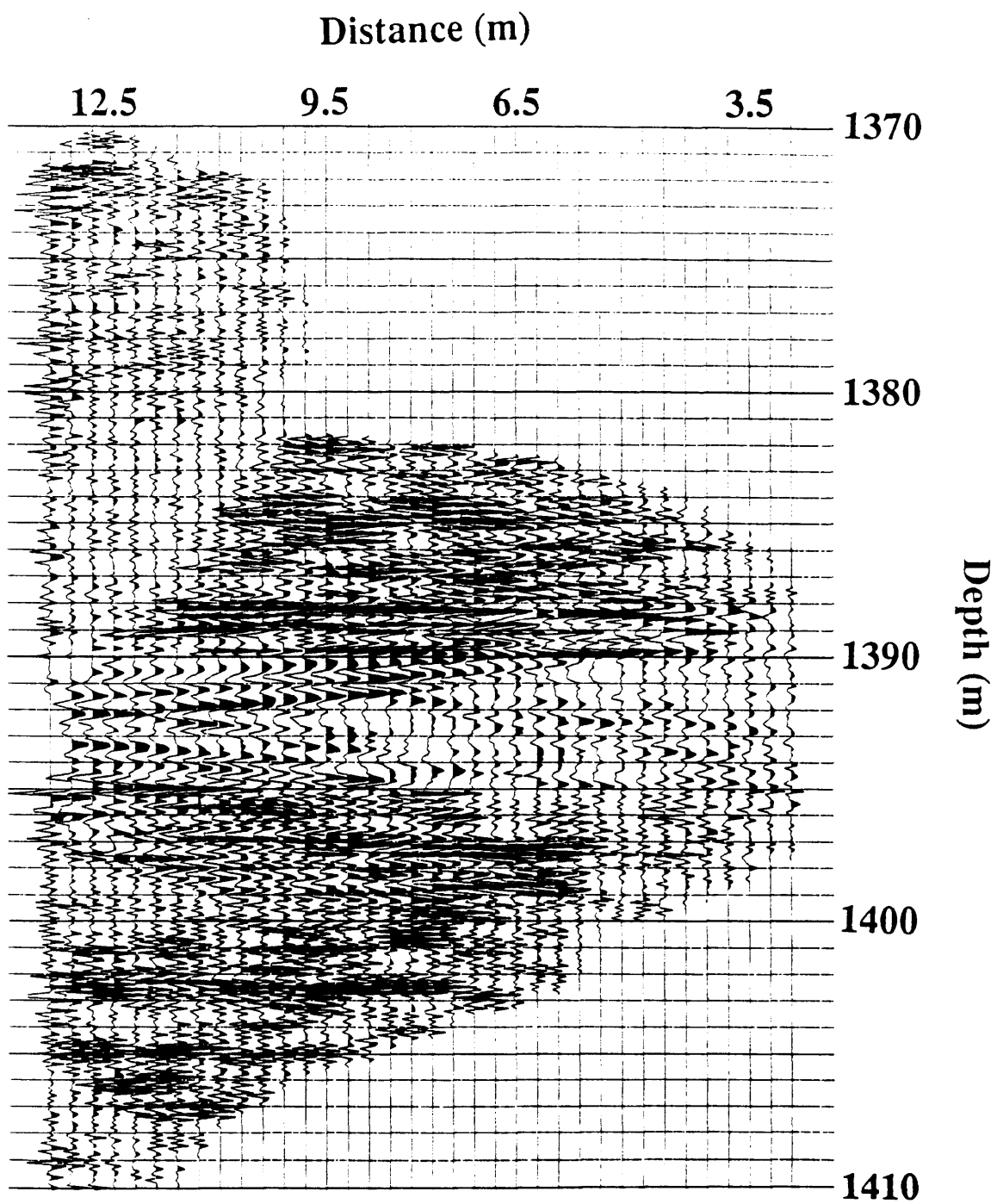


Figure 4.24: Total map of XHLCDP transformation for receiver 2 of the field data.

1. The cut-off apparent on the boundaries of the record is the result of the limited recording time of the field experiment. Figure 4.25 depicts the approximate form of the mapped record when the input data are as in Figures 4.11 and 4.12. It is very critical when acquiring crosswell data and reflections are of interest to record the maximum number of points possible. This would provide a better reflected image with higher fold.

2. Observe that in Figure 4.25 the subsurface area at and around the receiver location lack of significant reflected coverage. This depends on the interface locations where impedance contrasts exist. Transmitted arrivals would be the major constituent of this area. Now, looking back at the data in Figure 4.24 between the depth interval 1390 m and 1395 m, there is no interface in this zone to produce reflections in either upgoing or downgoing direction. In fact, this zone is an anhydrite unit in the Ratcliffe beds. The reason for the dipping, relatively low-frequency, events present in this zone is the transformation program used. While transforming the data, there is a step where the traces are bent in the new domain of offset distance and depth (before binning takes effect). The algorithm does not exactly bend the traces the way they are displayed in Figure 4.25. It is processing the data as if they are VSP data. So, it computes the correct reflection points for those locations beyond the midpoint and toward the receiver borehole. But it connects these bent traces to their source locations at the source borehole line. This is the problem since there can be no upgoing reflections generated at points above the receiver level and also there can be no downgoing reflections generated below the receiver level.

3. The flat horizons in the image are the primary reflected events. These events are somewhat puzzling. First, they are high-frequency signal concentrating in different parts of the image, particularly the upgoing part (1395 m to 1410 m). Second, they are masked by even higher-frequency signal in the entire section in general. Finally, the downgoing part of the image (1382 m to 1390 m) has a discontinuity in its reflected energy (toward the left of the section). This suggests in fact that there are source directivity effects in these data.

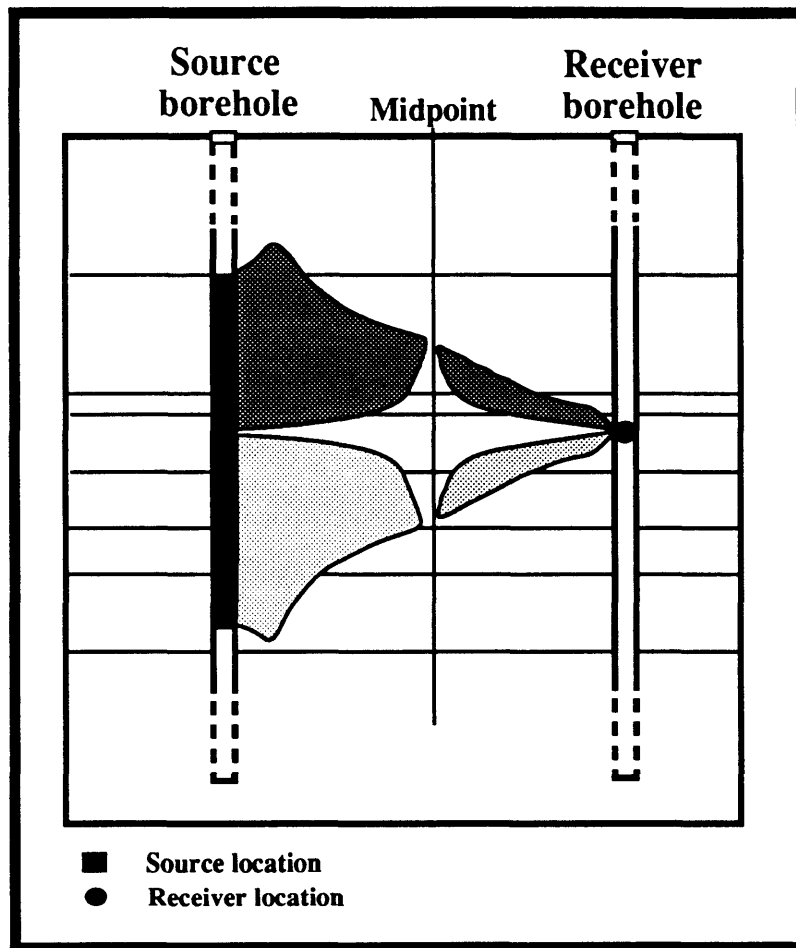


Figure 4.25: Subsurface coverage of receiver gather 2. Note the effect of limited recording time on the coverage.

The general content of reflectivity in the image is somewhat disappointing.

However, with some enhancement of primary signal and removal of noise signal, a much

more reasonable image can be produced. Figure 4.26 shows the same data in Figure 4.24 after the following poststack processes:

- Mute of the noisy zone around the receiver location that has no reflectivity coverage as seen in the approximate subsurface coverage (Figure 4.25).
- f - k dip filter to enhance primary reflections.
- High-cut bandpass filter to remove high-frequency noise components.
- Automatic gain control (AGC) to help continue the events.

Several reflectors are now easily seen with relatively higher signal-to-noise ratio than the data shown before the previous processing steps. All the shot records of synthetic and the receiver gathers of field data are processed similarly according to the respective flow discussed for each data set.

Finally, it should be noted that attempts were made to migrate both synthetic and field records using a VSP Kirchhoff migration program of the Western Geophysical software. The migration of synthetic data produced depth sections with similar interface locations as those produced by the mapping procedure shown earlier. However, a number of attempts to migrate the field records showed unacceptable smeared sections. These are probably due to the lack of coverage of every receiver gather on which the migration is performed. The mapping procedure was then concentrated on as the only reconstruction technique to obtain the depth sections.

4.9 Sum

At this point, the several maps of synthetic and field data are individually reconstructed. Since the area of subsurface coverage depends on the source/receiver array, it is of interest to sum all maps of each data set and form one composite reflection image of

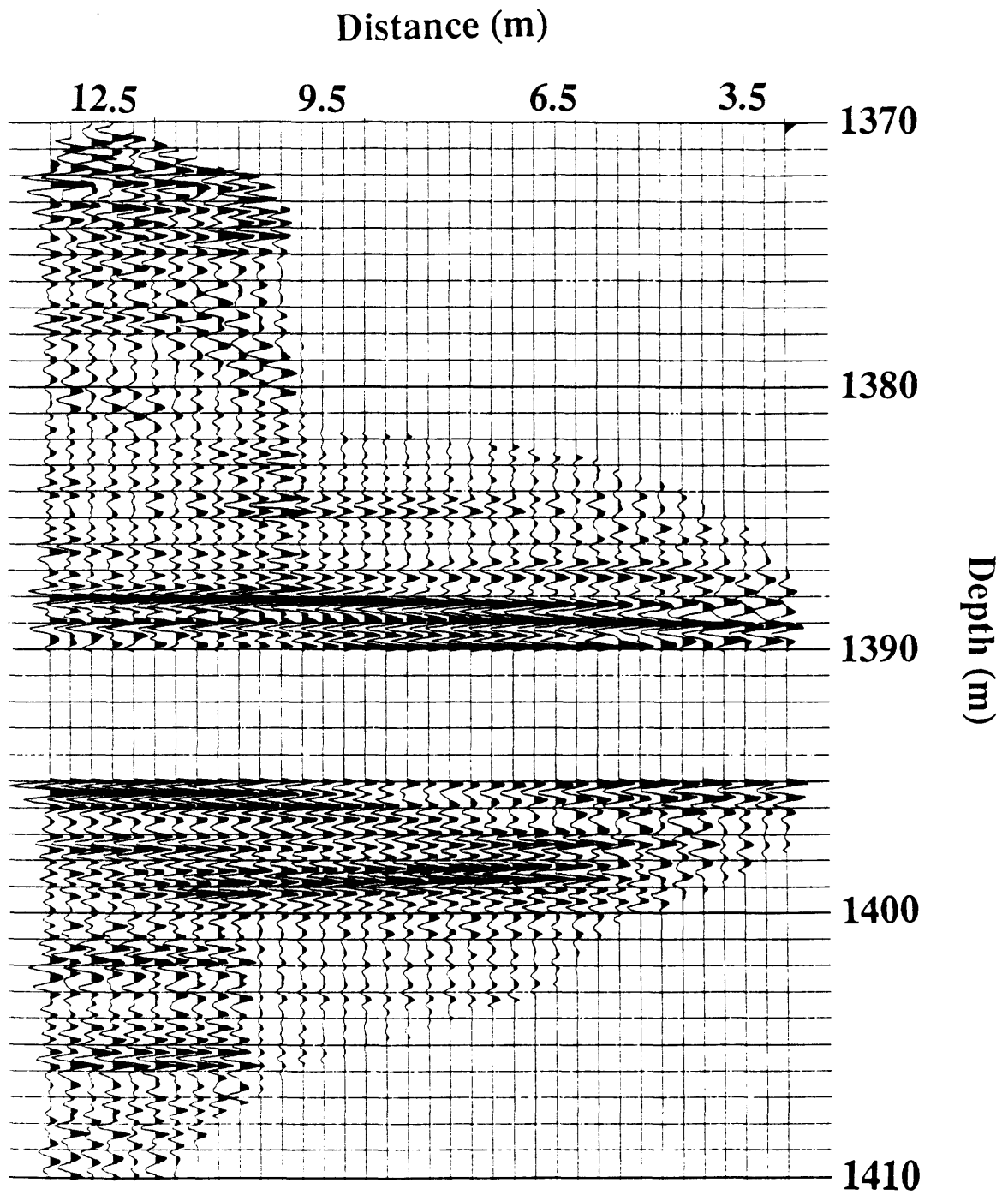


Figure 4.26: Total map of XHLCDP transformation for receiver 2 of the field data after further poststack processing.

the subsurface between the boreholes. This should also provide the maximum subsurface coverage for both upgoing and downgoing wavefields. The summing procedure is conducted accordingly to keep the amplitude level the same in the final map. The sum is normalized by the number of live samples added together.

The sum of the three total maps of the synthetic data is shown in Figure 4.27. The midpoint between the source and receiver boreholes in this data set is 52.5 m. The final image (Figure 4.27) reveals the maximum coverage on both sides of the midpoint, not seen on the individual maps of shot 2 alone (Figure 4.20 and 4.21). Some artifacts, however, appear on this final section as lateral amplitude changes resulting from summing events not exactly aligned. These artifacts can be seen at depths about 82 m, 95 m, and 146 m. The reflector at about 123 m (negative polarity) suffers a distorted edge which is contributed from a single map and could not be canceled out by the sum.

For the sum of the nine total receiver maps of the field data, the final image is shown in Figure 4.28 for depth interval 1370 m to 1420 m. One advantage of the sum of the maps here is the contribution of the other maps into the muted zone, 1390 m - 1395 m, of the single receiver map shown in Figure 4.26. In fact, this is another reason for muting the zone around the receiver location that does not exhibit any reflected energy. That is, if the muted data were summed to other maps that show primary reflections, the stack would have been erroneous. The other advantage is that there are three overlapping depth intervals covered as a result of the three receiver groups as mentioned earlier in the data description section 2.5. These intervals, when stacked together, give an interval of 1370 m to 1440 m. Figure 4.28 is only shown down to 1420 m. There is a mute zone starting at 1418 m that had no coverage. No more maps are available to overlap in this area.

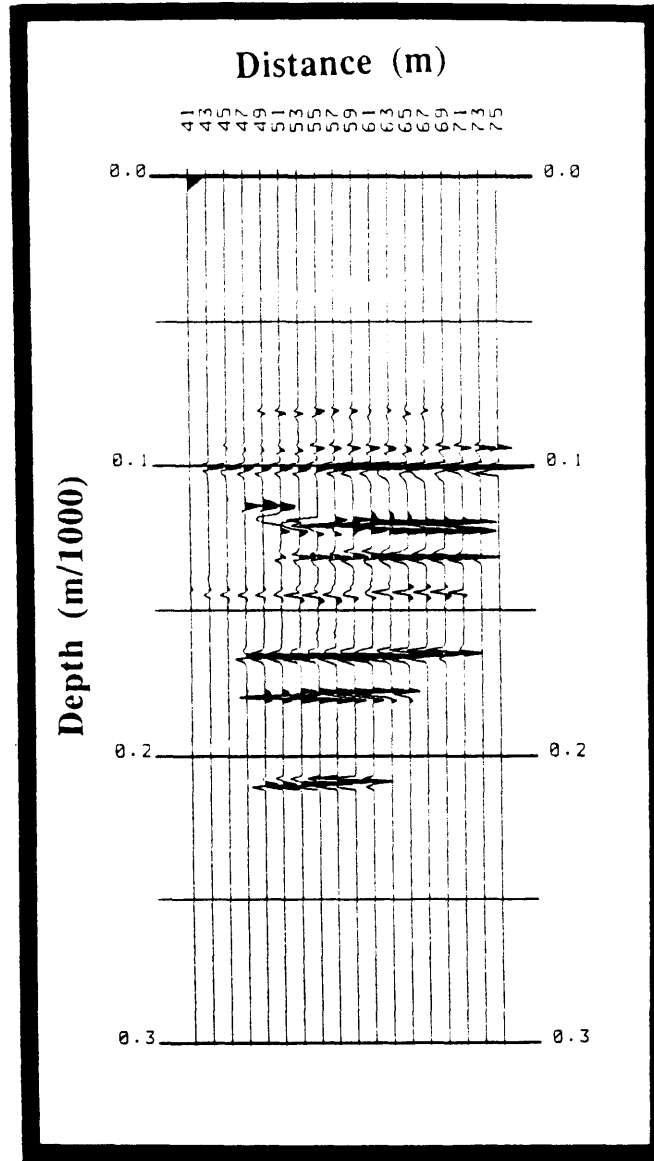


Figure 4.27: The sum of all maps of the synthetic data set.

The lateral illumination of the image extends along most of the subsurface, 3.0 m to 13.5 m from the receiver borehole with bin width of 0.3 m. An additional feature, and perhaps the most significant achievement of that image, is the vertical resolution. In Figure 4.28, events can be seen within an interval less than 1 m (about 0.5 m).

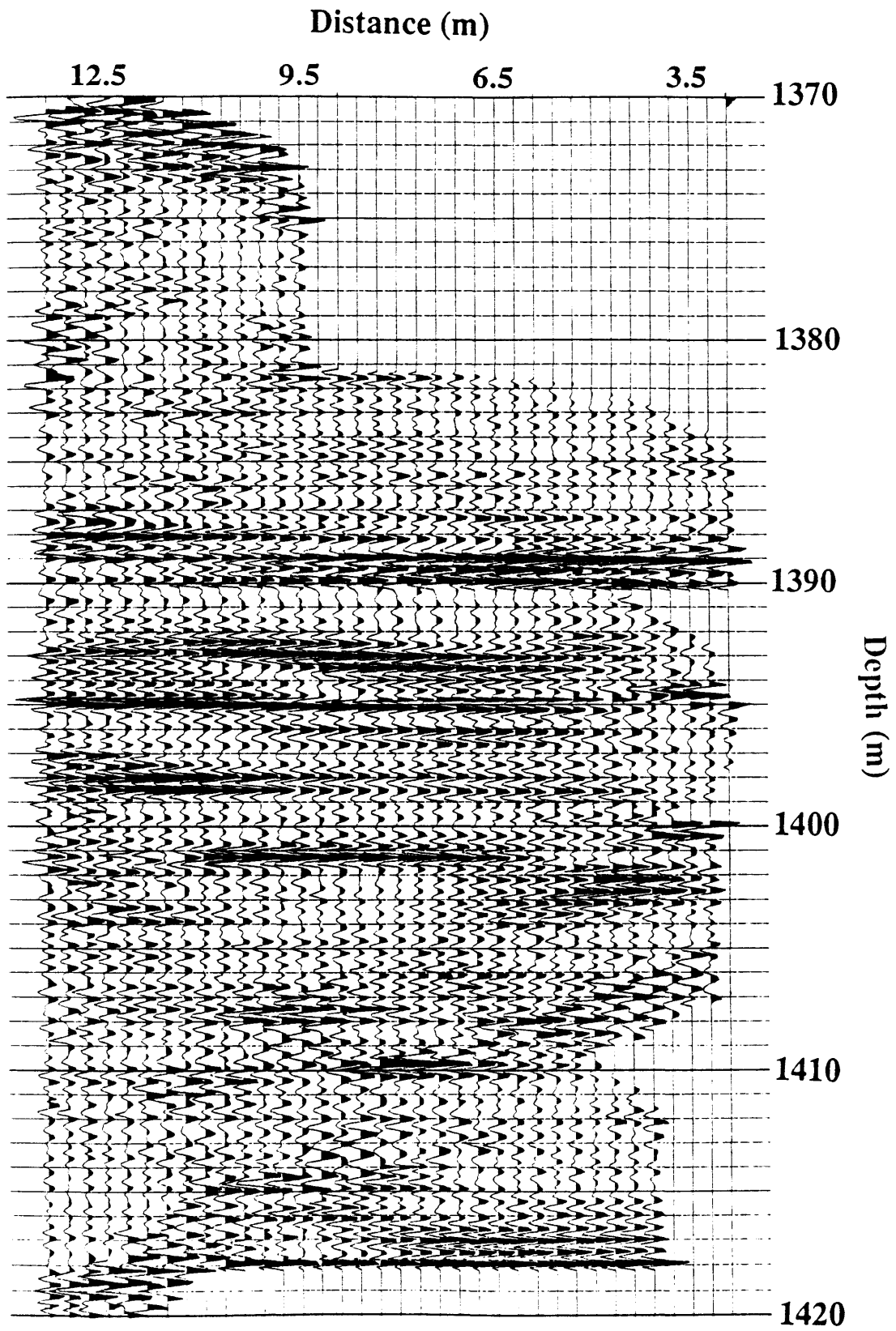


Figure 4.28: The sum of all maps of the field data set.

As seen also in the final section of the synthetic example (Figure 4.27), there is a considerable degradation in some of the field-data events after the sum. Note the weaker event in the final image (Figure 4.28) at about 1388 m compared to its corresponding strength before the sum (Figure 4.26). Other events exhibit similar effects of the destructive interference as seen in the final image at a depth of about 1401 m. The direct reason for such interference, as discussed earlier, is that similar events in the different maps are not located at exactly the same depth. Two possible reasons can be stated. The first is that the velocity-constructed model from the inversion results is not perfect for all the different maps. The second reason goes back to the unconfirmed source/receiver locations in the field experiment. Finally, the presence of the noisy dipping trend in the final section (Figure 4.28) at a depth of about 1405 m on the right side of image and a depth of 1420 m on the left side is a result of single-fold coverage.

4.10 Instantaneous amplitude

The high-cut bandpass filter used to produce the map of Figure 4.26 is designed to obtain a smooth representation of the reflected data. However, the wavelet sharpness maintained after the band-pass filter seems to destructively affect the sum of the final map (Figure 4.28).

Seeking a localized measure of the reflectivity strength along the depth interval of the final maps, instantaneous amplitude sections are computed using the method of complex attributes (Taner, 1978). In short, the seismic trace is represented as a complex function $\mathbf{u}(t)$,

$$\mathbf{u}(t) = \mathbf{x}(t) + i \mathbf{y}(t), \quad (4.17)$$

where $\mathbf{x}(t)$ is the seismic trace and $\mathbf{y}(t)$ is its quadrature. The quadrature is a 90-degree phase-shifted version of the recorded trace. It is obtained by taking the Hilbert transform of

$x(t)$ (Bracewell, 1965; Yilmaz, 1987). The instantaneous amplitude, $R(t)$, computed from

$$R(t) = [x^2(t) + y^2(t)]_2^{\frac{1}{2}}. \quad (4.18)$$

is proportionally related to the square root of the total energy of the seismic trace at an instant of time.

Figures 4.29 and 4.30 show the reflectivity strength of the individual map (Figure 4.26) and the final sum of maps (Figure 4.28) respectively. A general smoothed description of the reflectivity is now obtained maintaining the high vertical resolution content (about 1 m) of the images.

4.11 Conclusions

A crosswell processing flow is presented here to construct a subsurface image using the reflected wavefields. Most of the processing steps are conventionally used in VSP data processing. This suggests that processing crosswell data can be achieved with existing software.

Median filtering both synthetic and field data followed by $f-k$ dip filtering (field data only) contributed to the enhancement and the separation of direct, upgoing reflected, and downgoing reflected events. Deconvolution of crosswell data was attempted using the two types of deconvolution algorithms, deterministic and statistical. However, both types were found to degrade the reflections in the recorded data. For that reason, no deconvolution was used in the processing of this crosswell data set.

Based on a constant-velocity model, subsurface reflection of the crosswell geometry is investigated and shown to have an extended coverage that goes past the

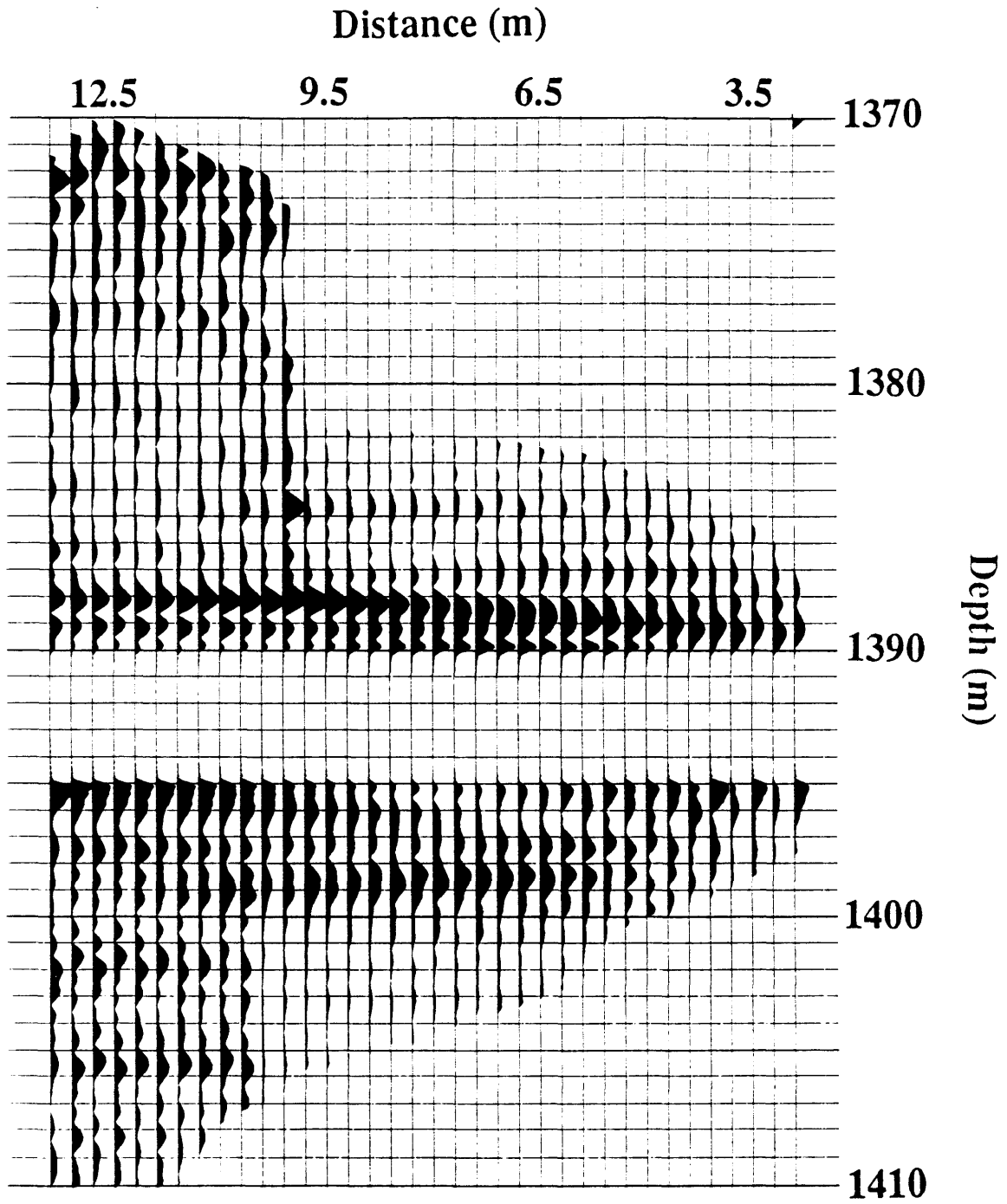


Figure 4.29: Instantaneous amplitude of the single receiver map (Figure 4.26).

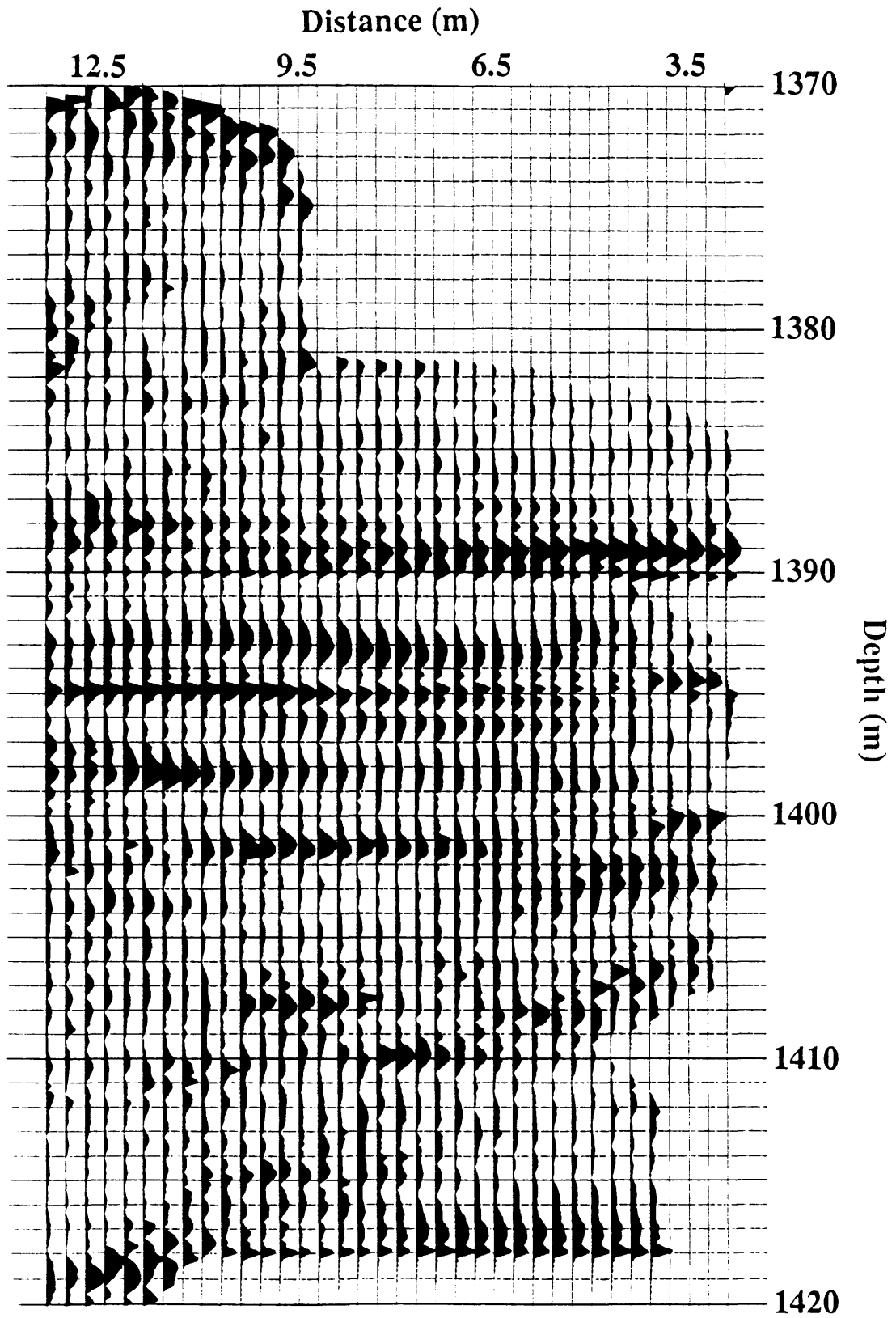


Figure 4.30: Instantaneous amplitude of the sum of all maps (Figure 4.28).

midpoint between the boreholes. Both upgoing and downgoing primary reflections are used in a crosswell transformation procedure, called here XHLCDP, that constructs a reflected image of the data in the domain of subsurface lateral distance and depth. Further poststack processing has produced maps of higher signal-to-noise ratio that are summed together to form one final reflection image of the subsurface area covered by the crosswell survey. The final image exhibits detailed description (resolution) both laterally, along the subsurface between the boreholes, and vertically, separation between events in depth. Finally, instantaneous amplitude sections are generated to depict the reflectivity strength of the subsurface.

Chapter 5 - Data interpretation

5.1 Introduction

The reflection processing of crosswell seismic data, discussed in the previous chapter, results in a reflected image of the subsurface area between the boreholes. To justify the validity of such an image and to identify the events it contains, an interpretation procedure is undertaken using the prior information available in both synthetic and real data cases.

For the synthetic data case, available information is merely the model (Figure 2.5) used to generate the shot records. On the other hand, only sonic log information is available for the real data case.

Synthetic seismograms (Peterson et al., 1955) made from the velocity logs are widely used to identify geological horizons and hence help interpreters to correlate seismic reflections with the geological structure (Al-Sadi, 1980; Anderson et al., 1989). The use of synthetic seismograms also extends to the integration of surface seismic and VSP data (e.g. Stewart and Disiena, 1989; Geis et al., 1990) leading to improvements in data interpretation.

In this Chapter, synthetic seismograms are used to demonstrate the high resolution crosswell data can offer. Finally, they are also used to identify the events in the resultant image from the reflection processing of field data and reach a satisfactory interpretation of the subsurface area covered by the survey.

5.2 Synthetic data

Although it is trivial to interpret data whose solution is known, the purpose here is to examine the location of the mapped events in the final synthetic image (Figure 4.27).

Comparing the synthetic model (Figure 2.5) to the produced image shows that events are accurately mapped into their subsurface depths according to their proper reflection coverage. The reflected event located at about 123 m exhibits a distorted signal at the left end as a result of the mute performed on the shot records and the lack of coverage due to these being only 3 shot records. In general, the mapping procedure is proven to provide useful depth information about the subsurface reflectors between boreholes.

5.3 Synthetic seismograms

Using the shear velocity log recorded in well FS-1, the source well, a group of band-limited synthetic seismograms is generated to demonstrate the types of resolution various frequency bands offer. A time plot with depth annotated (Figure 5.1) shows the steps involved in constructing the seismograms. From right to left, the shear sonic log is shown for the interval from 1300 m to 1500 m. Then, the interval velocity function (inverse of the slowness) of the log is computed for the same zone. The reflectivity series is then calculated assuming a constant unit density and normal incidence reflectivity (Peterson et al., 1955). Finally, zero-phase wavelets over various bands are convolved with the reflectivity function to yield the seismograms shown on the left of Figure 5.1. Each group contains 8 repeated seismograms with the 4-point band limits (displayed on top in hertz) used to construct the wavelet.

The first seismogram from the left can be considered as the response of surface seismic wavelets due to the conventional bandwidth it contains. Around the zone of interest 1380 m to 1420 m, this seismogram fails to describe the reflectivity series for the entire interval. As the bandwidth gets broader (to the right) except the fourth group of seismograms, the reflectivity description is largely improved with the most detailed representation seen in the extreme right seismogram. The purpose of constructing the fourth seismogram is to show that high resolution does not mean high-frequency band

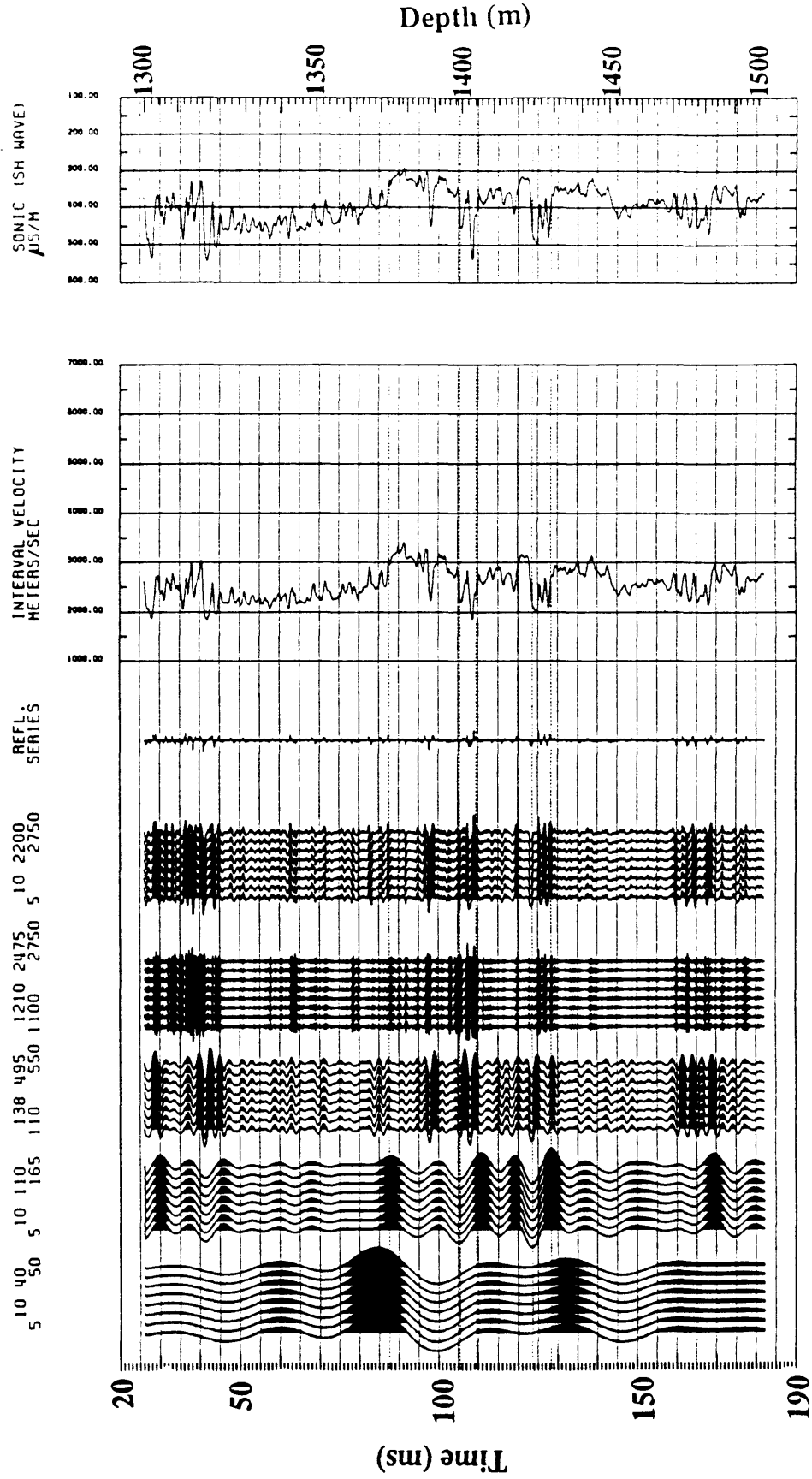


Figure 5.1: Synthetic seismograms generated from the shear sonic log from the source well (FS-1). The band limits used to generate the wavelet are annotated on the top of each group of synthetic seismograms.

limits with no low-frequency components. But it does mean broad bandwidth.

The previous discussion suggests that the description of the reflectivity series is a function of the bandwidth of the source wavelet. The use of sources producing broad-band seismic wavelets promises the unique resolution ability of the crosswell experiment (Iverson, 1988).

5.4 Field data

The final goal is to interpret the pictures of the field data (Figure 4.28 and 4.30) that have been made. Shown in Figures 5.2 and 5.3 are the final depth images (map and its envelope) along with the shear velocity log recorded in well FS-1 and a synthetic seismogram for the same depth interval. The band-limited wavelet used to generate the synthetic seismogram has a passband similar to that used to filter the crosswell image. The synthetic seismogram has been converted from time to depth using the sonic velocity function, shown on the left of both figures. On the other hand, and as discussed earlier, the crosswell maps are based on the velocity functions obtained from the traveltime inversion of Chapter 3. So, we can see that there could be a built-in difference in the velocity functions used to construct the synthetic seismogram and the reflected image. This difference can appear as a depth mismatch when comparing the two data types. The other theoretical principle that the synthetic seismogram is based on is the assumption of normal incidence reflectivity. That assumption may not be valid for the crosswell image since its transformation is performed based on nonnormal incidence using raytracing.

With the previous assumptions in mind, the correlation between the synthetic seismogram and the reflected images is carried out to identify possible reflected horizons. Fairly good correlation can be observed in both Figures, 5.2 and 5.3, which suggests once

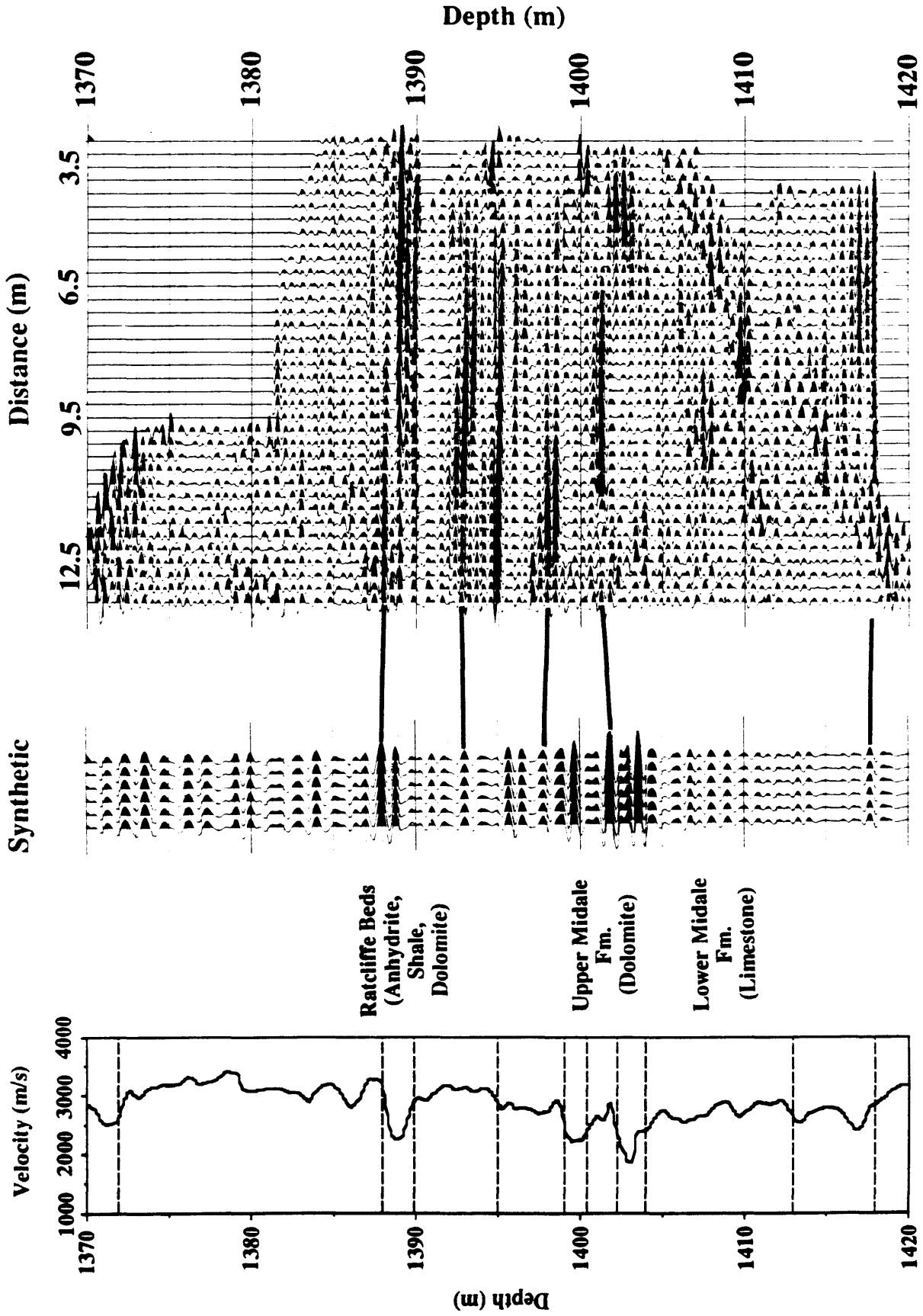


Figure 5.2: Correlation between the sum of all receiver-gather maps (right) and the synthetic seismogram in depth (middle) generated from the sonic log (left).

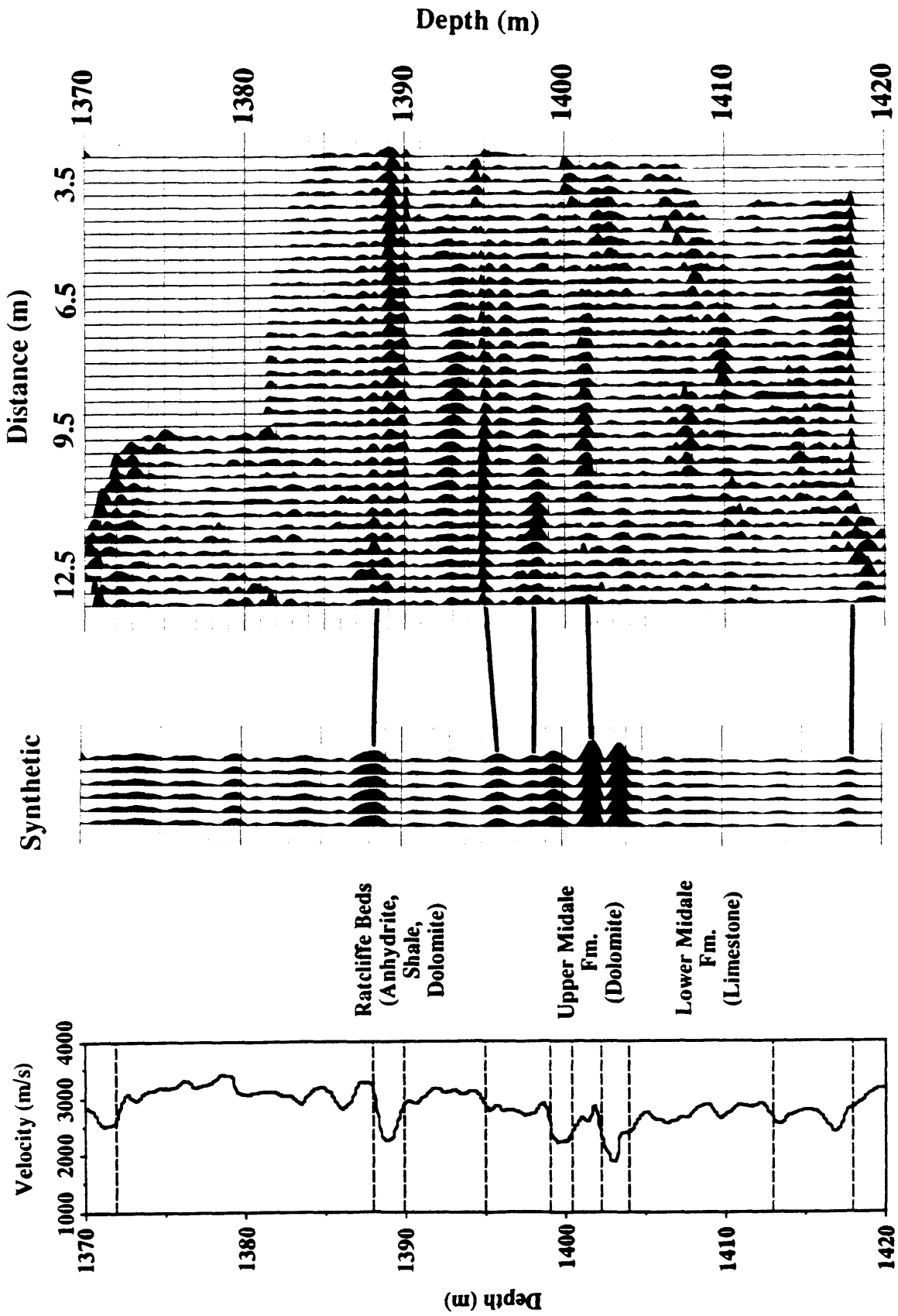


Figure 5.3: Correlation between the instantaneous amplitude of the sum (right) and the synthetic seismogram in depth (middle) generated from the sonic log (left).

again that the mapping procedure provides suitable results for estimating the location of the subsurface horizons. However, the synthetic seismogram shows a depth stretch with respect to some of the events in the crosswell image. This is probably due to the difference between the two velocity functions used in constructing the synthetic and the crosswell section. Several horizons are identified as displayed in Figures 5.2 and 5.3. Of these horizons are the tops of shale and other interbeds in the Ratcliffe Formation. The top and an interbed interface in the marly dolomite, upper Midale Formation, can also be correlated with their corresponding events in the crosswell images. Although similar band-pass filters are used in both the synthetic seismogram and the crosswell field data, inspecting the two final Figures 5.2 and 5.3 suggests that the crosswell images contain data of higher resolution than that of the synthetic seismogram obtained from the sonic log. This can be referred to the fact that the resolution of reflected crosswell data largely depends on the frequency bandwidth of the source used. On the other hand, the resolution of the sonic log depends on the spacing between the source and receiver which may not resolve zones that are thinner than 1 m.

5.5 Conclusions

Synthetic seismograms show that crosswell data can provide detailed information about the seismic impedance functions of the subsurface. The interpretation procedure presented here for the synthetic and field data sets has confirmed the validity and the suitability of the imaging technique used to construct reflected images of crosswell seismic data. The produced subsurface sections are of very high resolution even with respect to the synthetic seismogram generated from the sonic log. Using different velocity estimates causes difficulties in correlating the crosswell images with synthetic seismograms.

Chapter 6 - Conclusions

The current study has considered traveltime inversion, reflection processing, and interpretation of synthetic and field crosswell seismic data. These topics have contributed to the exploitation of the full waveform of crosswell data and the deduction of information about the geology in terms of velocity and reflectivity of the subsurface between the boreholes.

Investigating receiver-gathered crosswell data from the Midale field of southeastern Saskatchewan, band-pass filtering has shown coherent signal up to about 17 kHz. Mode-converted events (P to S and S to P) at the borehole walls exist and enable the study of S waves as well as P waves. The wave propagation of the crosswell geometry has depicted the presence of direct P- and S-wave arrivals as well as reflected upgoing and downgoing shear wave arrivals. Transmitted-converted (S to P) waves are also identified by implementing a median filtering process designed on the P-wave direct arrivals. The occurrence of such events (converted transmissions) is found to assist in constructing the layering of a 1-D model needed for the traveltime inversion. Other wave types included head waves generated as a result of a low-velocity zone in the upper Midale formation as well as peg-leg multiple activity of both P and S waves believed to have been generated in the high-velocity zone of the upper Midale formation.

Inverting crosswell P- and S-wave direct arrivals using a layer-stripping via raytracing technique has produced background or macroscopic velocity maps. The inversion method, which is model-based, starts solving for the interval in which both source and receiver are located. Then, from the receiver layer outward (upward and downward), the algorithm proceeds, solving for subsequent intervals using the previously calculated interval velocities. Testing the algorithm on synthetic data has offered better

understanding of the results and its associated errors. Synthetic data inversion has shown that performing the inversion on every point is of advantage, that is, selecting the optimum solution with the least timing error present in the data. Traveltime inversion of three independent field gathers has provided P- and S-wave results within a range of 200 m/s for the most part. Unconfirmed source/receiver locations are blamed for the discrepancy in the velocity estimates in a thin shale interval. Furthermore, the results of the field data traveltime inversion have undergone a series of tests to evaluate their reliability. First, the estimated P- and S-wave interval velocities are found to be consistent with the full-waveform log velocities. Both types of information, sonic and seismic, are in the same range except one disagreement in the thin shale interval. The difference between the sonic and seismic velocities of that shale interval has been referred to possible errors in the sonic log, unconfirmed locations, anisotropic effects in shale, or finally raypath complexity. A second evaluation of the inversion results is conducted by generating forward-raytraced direct traveltimes using the estimated (1-D) velocity solutions and comparing them to their respective observed traveltimes. That comparison has shown good agreement between the computed and the true traveltimes in both P and S cases. Based on that comparison, the residual average error magnitude in each interval is then computed and found to have a maximum of 1.45 percent in one interval in the P-wave solution. A final evaluation is carried out by considering the two velocity solutions (P and S) with their V_p/V_s estimate. The results of this evaluation are found to agree with reported measurements of V_p/V_s of the available subsurface lithology information.

Processing crosswell reflected upgoing and downgoing shear wave arrivals has produced reflected images that represent the subsurface between boreholes in the domain of lateral distance and depth. Processing such data does not need special software development. It can be performed using the conventional borehole software. Filtering processes such as median and $f-k$ have contributed in the enhancement and to the separation

of direct, upgoing reflected, and downgoing reflected events in both synthetic and field data. A number of attempts (deterministically and statistically) are made to deconvolve the data. However, deconvolution always degraded the reflections. Factors such as effects of lithology and radiation patterns due to the different propagation directions of both direct and reflected waves may give an indication of the unsuitability of assuming that the direct arrivals represent the seismic wavelet (in deterministic deconvolution). It can also be that the assumption of minimum-phase wavelet (required in the deconvolution process) is not valid in this data case and filter operators could not be properly constructed to compress the wavelets. So, ultimately no deconvolution has been used in this study. Time-variant gain and trace equalization are used after separating the reflected wavefields to account for amplitude losses and prepare the data for the mapping and summing processes.

Considering the crosswell subsurface coverage, a mathematical expression based on a constant-velocity model is developed for the location of reflection points in the crosswell geometry. It is found that the crosswell geometry has an extended coverage that goes past the midpoint between the boreholes. This feature gives crosswell reflection processing an advantage, that is, the ability to delineate subsurface horizons between boreholes. A transformation procedure, called here XHLCDP, similar to the conventional VSPCDP mapping process is then used to construct a reflection image from both upgoing and downgoing wavefields. The method is based on the shear-velocity function obtained from the traveltimes inversion. The resulting image presents the crosswell data in the domain of subsurface lateral distance and depth. Poststack processing provides higher signal-to-noise ratio maps that are summed together to yield a final reflected image of the subsurface area covered by the crosswell survey. The lateral illumination of the final image extends along most of the subsurface, 3.0 m to 13.5 m (borehole separation of 13.5 m). In addition, vertical separation between events (vertical resolution) can be seen within an interval less than 1 m (about 0.5 m). A smoothed description of the reflectivity strength is

obtained by producing an instantaneous amplitude section of the final map maintaining the high resolution content (about 1 m) of the images. The final images, particularly the mapped section, exhibit a considerable degradation in some of the events after the sum. These are primarily due to the imperfect velocity solution used in the mapping procedure for the different receiver maps. These receiver maps contain high-frequency events that are very difficult to align properly.

Interpreting the final sections is carried out using depth synthetic seismograms. Many subsurface horizons at and around the zone of interest are identified and shown to extend the interpretation of logs between boreholes. In this case study, crosswell data appear to provide higher resolution image of geologic strata than those predicted by the synthetic seismograms.

Chapter 7 - Future work

This thesis attempted to develop an integrated flow for the processing of crosswell seismic data. Reflection processing of crosswell data is not quite established. Therefore, it was of considerable interest to present the method considered here in a complete (start to end) manner without developing the optimum technique for every processing step. In this respect, some future work topics regarding specific processing steps are discussed.

Both the traveltimes inversion (Chapter 3) and the mapping (section 4.8) techniques are operated on individual shot/receiver records. They also require a geologic model as prior information on which the procedures are based. With the recording of several tens of crosswell records, these two procedures consume a great deal of time and effort on the processor side. More robust algorithms that operate on multi-record data, particularly those that do not require geologic or velocity information, are of major need to overcome these processing difficulties. Current research activities in the area of crosswell seismology of the CREWES project at The University of Calgary are directed to these topics. Another field of future investigation is the deconvolution question where medium effects and radiation patterns appear to have different effects on the waveforms of both direct and reflected wavefields.

The current processing study suggested that crosswell data can encounter lateral amplitude changes on events reflected from one interface. Raypath geometry showed the wide range of incidence angles the crosswell experiment may exhibit particularly for recording locations near the source level. It is proposed then that true-amplitude processing be considered in future crosswell studies. In this case, numerical modeling would have an important role investigating the subsurface coverage using a realistic geologic model of the area surveyed by the experiment.

References

- Abdalla, A. A. and Stewart, R. R., 1989, Reflection processing of synthetic crosshole data: paper 16, presented at the First Annual Meeting of the CREWES Project, Banff, Alberta, 225-244.
- Abdalla, A. A., Stewart, R. R., and Henley, D. C., 1990, Traveltime inversion and reflection processing of cross-hole seismic data: paper BG2.8, presented at the 60th Annual Meeting of SEG, San Francisco, 47-50.
- Al-Sadi, H. N., 1980, *Seismic Exploration: Technique and Processing*: Birkhauser Verlag Basel.
- Anderson, N. L., Brown, R. J., and Hinds, R. C., 1989, Low- and high-relief Leduc formation reefs: A seismic analysis: *Geophysics*, 54, 1410-1419.
- Baker, L. J. and Harris, J. M., 1984, Cross-borehole seismic imaging: paper BHG2.2, presented at the 54th Annual Meeting of SEG, Atlanta, 23-25.
- Banik, N. C., 1984, Velocity anisotropy of shales and depth estimation in the North Sea basin: *Geophysics*, 49, 1411-1419.
- Beydoun, W. B., Delvaux, J., Mendes, M., Noual, G., and Tarantola, A., 1989, Practical aspects of an elastic migration/inversion of crosshole data for reservoir characterization: A Paris basin example: *Geophysics*, 54, 1587-1595.
- Bois, P., La Porte, M., Lavergne, M., and Thomas, G., 1972, Well-to-well seismic measurements: *Geophysics*, 37, 471-480.
- Bracewell, R., 1965, *The Fourier transform and its applications*: McGraw-Hill Book Co.
- Bregman, N. D., Bailey, R. C., and Chapman, C. H., 1989a, Crosshole seismic tomography: *Geophysics*, 54, 200-215.
- Bregman, N. D., Hurley, P. A., and West, G. F., 1989b, Seismic tomography at a fire-flood site: *Geophysics*, 54, 1082-1090.

- Burden, R. L. and Faires, J. D., 1985, Numerical analysis: PWS publishers.
- Castagna, J. P., Batzle, M. L., and Eastwood, R. L., 1985, Relationships between compressional-wave and shear-wave velocities in clastic silicate rocks: *Geophysics*, 50, 571-581.
- Chen, S. T., Zimmerman, L. J., and Tugnait, J. K., 1990, Subsurface imaging using reversed vertical seismic profiling and crosshole tomographic methods: *Geophysics*, 55, 1478-1487.
- Dillon, P. B. and Thomson, R. C., 1984, Offset source VSP surveys and their image reconstruction: *Geophys. Prosp.*, 32, 790-811.
- Esmersoy, C., 1990, Inversion of P and SV waves from multicomponent offset vertical seismic profiles: *Geophysics*, 55, 39-50.
- Fehler, M. and Pearson, C., 1984, Cross-hole seismic surveys: Applications for studying subsurface fracture systems at a hot dry rock geothermal site: *Geophysics*, 49, 37-45.
- Geis, W. T., Stewart, R. R., Jones, M. J., and Katopodis, P. E., 1990, Processing, correlating, and interpreting converted shear waves from borehole data in southern Alberta: *Geophysics*, 55, 660-669.
- Hamming, R. W. and Feigenbaum, 1971, Introduction to applied numerical analysis: McGraw-Hill Book Co.
- Hardage, B. A., 1985, Vertical Seismic Profiling: Geophysical Press, 14A.
- Harris, J. M., Tan, H., Lines, L., Pearson, C., Treitel, S., Mavko, G., Moos, D., and Hoeksma, R. N., 1990, Cross-well tomographic imaging of geological structures in Gulf Coast sediments: paper BG2.5, presented at the 60th Annual Meeting of SEG, San Francisco, 37-40.

- Harrison, M. P., 1989, Three-component seismic data processing: Carrot Creek, Alberta: paper 2, presented at the First Annual Meeting of the CREWES Project, Banff, Alberta, 6-26.
- Hornby, B. E., 1989, Imaging of near-borehole structure using full-waveform sonic data: *Geophysics*, 54, 747-757.
- Hu, L., McMechan, G. A., and Harris, J. M., 1988a, Acoustic prestack migration of cross-hole data: *Geophysics*, 53, 1015-1023.
- Hu, L., McMechan, G. A., and Harris, J. M., 1988b, Elastic finite-difference modeling of cross-hole seismic data: *Bull. Seis. Soc. Am.*, 78, 1796-1806.
- Inderwiesen, P. L. and Lo, T., 1990, Cross-hole seismic tomographic imaging of reservoir inhomogeneities in the Midway Sunset field, California: paper BG2.1, presented at the 60th Annual Meeting of SEG, San Francisco, 22-25.
- Ivansson, S., 1985, A study of methods for tomographic velocity estimation in the presence of low-velocity zones: *Geophysics*, 50, 969-988.
- Iverson, W. P., 1988, Crosswell Logging for Acoustic Impedance: *Pet. Tech. J.*, 75-82.
- Justice, J. H., 1986a, Traveltime inversion for the flat-layer model: *Geophysics*, 51, 1904-1911.
- , 1986b, Interval velocity analysis from VSP surveys: *J. Can. Soc. Expl. Geophys.*, 22, 33-43.
- Justice, J. H., Vassiliou, A. A., Singh, S., Logel, J. D., Hansen, P. A., Hall, B. R., Hutt, P. R., and Solanki, J. J., 1989, Acoustic tomography for monitoring enhanced oil recovery: *The Leading Edge*, 8, no. 2, 12-19.
- Justice, J. H., Vassiliou, A. A., Mathisen, M. E., Bulau, J. R., Singh, S., and Cunningham, P. S., 1990, Cross-hole seismic tomography-reservoir interpretation case histories: paper BG2.6, presented at the 60th Annual Meeting of SEG, San Francisco, 41-42.

- Labonte, S, 1990, Modal separation, mapping, and inverting three-component VSP data: M. Sc. thesis, Department of Geology and Geophysics, University of Calgary.
- Lines, L. R., Bourgeois, A., and Covey, J. D., 1984, Traveltime inversion of offset vertical seismic profiles - A feasibility study: *Geophysics*, 49, 250-264.
- Lines, L. R. and LaFehr, E. D., 1989, Tomographic modeling of a cross-borehole data set: *Geophysics*, 54, 1249-1257.
- Lo, T., Inderwiesen, P. L., Howlett, D. L., Melton, D. R., Livingston, N. D., Paulsson, B. N. P., and Fairborn, J. W., 1990, McKittrick cross-well seismology project: Part II. tomographic processing and interpretation: paper BG2.3, presented at the 60th Annual Meeting of SEG, San Francisco, 30-33.
- Lovell, J. R. and Hornby, B. E., 1990, Borehole coupling at sonic frequencies: *Geophysics*, 55, 806-814.
- Luo, Y. and Schuster, G. T., 1990a, Wave-equation traveltime inversion: paper SI4.2, presented at the 60th Annual Meeting of SEG, San Francisco, 1207-1210.
- , 1990b, Wave-equation traveltime + waveform inversion: paper SI4.6, presented at the 60th Annual Meeting of SEG, San Francisco, 1223-1225.
- Macrides, C. G., 1987, Seismic tomography in oil sands for monitoring thermal recovery processes: Ph. D. thesis, Department of Physics, University of Alberta.
- Macrides, C. G., Kanasewich, E. R., and Bharatha, S., 1988, Multiborehole seismic imaging in steam injection heavy oil recovery projects: *Geophysics*, 53, 65-75.
- Marzetta, T. L., Orton, M., Krampe, A., Johnston, L. K., and Wuenschel, P. C., 1988, A hydrophone vertical seismic profiling experiment: *Geophysics*, 53, 1437-1444.
- Miller, S. L. and Stewart, R. R., 1990, The effect of lithology, porosity, and shaliness on elastic-wave velocities from full-waveform sonic logs: *Can. J. Expl. Geophys.*, 26, 94-103.

- Newman, P., 1973, Divergence effects in a layered earth: *Geophysics*, 38, 481-488.
- Ostrander, W. J., 1984, Plane-wave reflection coefficients for gas sands at nonnormal angles of incidence: *Geophysics*, 49, 1637-1648.
- Paulsson, B. N. P., Fairborn, J. W., Cogley, A. L., Howlett, D. L., Melton, D. R., and Livingston, N. D., 1990, McKittrick cross-well seismology project: Part I. data acquisition and tomographic imaging: paper BG2.2, presented at the 60th Annual Meeting of SEG, San Francisco, 26-29.
- Peterson, R. A., Fillippone, W. R., and Coker, F. B., 1955, The synthesis of seismograms from well log data: *Geophysics*, 3, 516-538.
- Peterson, J. E., Paulsson, B. N. P., and McEvelly, T. V., 1985, Applications of algebraic reconstruction techniques to crosshole seismic data: *Geophysics*, 50, 1566-1580.
- Pickett, G. R., 1963, Acoustic character logs and their applications in formation evaluation: *J. Petr. Tech.*, June, 659-667.
- Poel, N. J. van der and Cassell, B. R., 1989, Borehole seismic surveys for fault delineation in the Dutch North Sea: *Geophysics*, 54, 1091-1100.
- Pratt, R. G. and Worthington, M. H., 1988, The application of diffraction tomography to cross-hole seismic data: *Geophysics*, 53, 1284-1294.
- Pratt, R. G. and Gouly, N. R., 1989, High-resolution tomography using the wave equation: results with physical data: paper BG3.6, presented at the 59th Annual Meeting of SEG, Dallas, 70-74.
- Rafavich, F., Kendall, C. H. St. C., and Todd, T. P., 1984, The relationship between acoustic properties and the petrographic character of carbonate rocks: *Geophysics*, 49, 1622-1636.
- Robinson, E. A. and Treitel, S., 1980, *Geophysical signal analysis*: Prentice-Hall Inc.

- Robinson, E. A., 1983, Seismic velocity analysis and the convolutional model: International Human Resources Development.
- Salo, E. L. and Schuster, G. T., 1989, Traveltime inversion of both direct and reflected arrivals in vertical seismic profile data: *Geophysics*, 54, 49-56.
- Slotnick, M. M., 1959, Lessons in seismic computing: *Soc. Expl. Geophys.*
- Stewart, R. R., 1984, VSP interval velocities from traveltime inversion: *Geophys. Prosp.*, 32, 608-628.
- , 1985, Median filtering: Review and a new f/k analogue design: *J. Can. Soc. Expl. Geophys.*, 21, 54-63.
- 1988, VSPCDP map for P waves: Personal communication.
- 1989, Integrated seismic analysis: Kidney area, northern Alberta, Canada: *Geophysics*, 54, 1240-1248.
- Stewart, R. R. and Disiena, J. P., 1989, The values of VSP in interpretation: The Leading Edge - *Geophysics*, 8, 16-23.
- Taner, M. T., 1978, Complex seismic trace analysis: *Geophysics*, 44, 1041-1063.
- Tatham, R. H. and Stoffa, P. L., 1976, V_p/V_s - A potential hydrocarbon indicator: *Geophysics*, 41, 837-849.
- Winterstein, D. F. and Paulsson, B. N. P., 1990, Velocity anisotropy in shale determined from crosshole seismic and vertical seismic profile data: *Geophysics*, 55, 470-479.
- Wyatt, K. D. and Wyatt, S. B., 1984, Determining subsurface structure using the vertical seismic profiling: In Toksoz, M. N., and Stewart, R. R., Eds, *Vertical seismic profiling: Advanced concepts*, Geophysical Press.
- Yilmaz, O., 1987, Seismic data processing: *Soc. Expl. Geophys.*

Zhu, X., and McMechan, G. A., 1988, Acoustic modeling and migration of stacked cross-hole data: *Geophysics*, 53, 492-500.